
Synthesis and Characterisation of Functional Organic-Inorganic Hybrid 'Soft' Materials

A Thesis Submitted for the Degree of

Master of Science

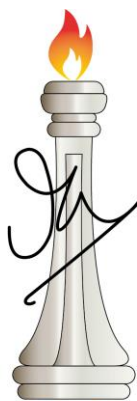
as a part of the

Integrated Ph.D. Programme

(Chemical Science)

by

Tarak Nath Das



J N C A S R

New Chemistry Unit (NCU)

Jawaharlal Nehru Centre for Advanced Scientific Research

(A Deemed University)

Bangalore – 560064

(March 2022)

Dedicated to
Chemistry Department,
Ramakrishna Mission
Vivekananda Centenary
College

DECLARATION

I hereby declare that the matter embodied in the thesis entitled “*Synthesis and Characterisation of Functional Organic-Inorganic Hybrid ‘Soft’ Materials*” is the result of investigations carried out by me at the New Chemistry Unit, Jawaharlal Nehru Centre for Advanced Scientific Research, India under the supervision of Prof. Tapas Kumar Maji and that it has not been submitted elsewhere for the award of any degree or diploma.

In keeping with the general practice in reporting the scientific observations, due acknowledgement has been made whenever the work described is based on the findings of other investigators. Any omission that might have occurred due to oversight or error in judgement is regretted.

Tarak Nath Das.

(Tarak Nath Das)

Date: 31.03.2022

CERTIFICATE

I hereby certify that the work described in this thesis entitled “*Synthesis and Characterisation of Functional Organic-Inorganic Hybrid ‘Soft’ Materials*” has been carried out Tarak Nath Das under my supervision at the New Chemistry Unit, Jawaharlal Nehru Centre for Advanced Scientific Research, India and that it has not been submitted elsewhere for the award of any degree or diploma.



Tapas Kumar Maji, Ph.D.
Professor
Chemistry & Physics of Materials Unit
Jawaharlal Nehru Centre for
Advanced Scientific Research
Jakkur, Bengaluru-560 064, India.

(Prof. Tapas Kumar Maji)

(Research Supervisor)

Date: 31.03.2022

Acknowledgments

I would like to express my sincere and heartfelt gratitude to my research supervisor Prof. Tapas Kumar Maji, for his constant support, guidance, and encouragement. He has not only motivated me with his invaluable suggestions but has also encouraged me to come up with my own ideas. His enthusiasm towards science has greatly inspired the young researcher in me. As I take a step further into the world of research, I am indebted to him for giving me an opportunity to work under his guidance and for mentoring me with infinite patience. Prof. C. N. R. Rao has always been a true source of inspiration, with his extraordinary enthusiasm and energy. I consider myself extremely privileged to have got the opportunity of listening to his delightful motivational words.

I express my sincere gratitude to the past and present chairmen of NCU: Prof. CNR Rao and Prof. Subi Jacob George, and CPMU: Prof. Balasubramanian, Prof. Chandrabhas Narayana, and Prof. A Sundaresan for allowing me to avail myself the research facilities of the Centre.

I am thankful to the Int. Ph.D. course instructors of JNCASR for the great coursework that has enriched my basic knowledge, which is valuable for going ahead in research. I would like to thank Prof. M. Eswaramoorthy, Dr. Premkumar Senguttuvan, Dr. Sarit Agasti, Prof. Sridhar Rajaram, Prof. Ranjani Viswanatha, Prof. Balasubramanian Sundaram, Prof. T. K. Maji, Prof. Kanishka Biswas, Prof. A. Sundaresan, Prof. Jayanta Haldar, Dr. Bivas Saha, Prof. Sebastian C. Peter, Prof. Subi J. George of JNCASR and Prof. Aloknath Chakraborty of IISc for their enlightening courseworks.

I am also greatly thankful to the technical staff members of JNCASR, namely, Mr. Anil, Mr. Vasu, Mr. Shivakumar, Mr. Mahesh, Mr. Srinivas, Mrs. Usha, Ms. Meenakshi, and Mr. Rahul, for their prompt help with instruments and measurements. I thank JNCASR Library, Complab, Hostel, Health Centre (Dhanvantari), Academics, and Administrative staff for providing and maintaining all the wonderful facilities which have made our campus lives smooth and easy.

I am extremely grateful to my labmates of the Molecular Materials Lab for maintaining a nice and healthy atmosphere in the lab. I owe my heartfelt gratitude to all the past and present members Dr. Ashish da, Dr. Soumitra da, Dr. Sandip da, Dr. Kamal da, Dr. Subhajit da, Dr. Parul di, Sanchita di, Faruk da, Anupam da, Rohan da, Adrija di, Arghya, Sneha, Souvik da for their help, cooperation and scientific discussions.

I want to convey my gratitude to Mrs. Supreeti Maji, Sonai, and Neel for their warm and vibrant company.

I extend my gratitude to my teachers from my alma mater institutions, Raghunathganj High School, Ramakrishna Mission Vivekananda Centenary College, and Ramakrishna Mission Calcutta Students' Home for helping me grow interest in this field. I am always thankful to my undergrad professor, Dr. Sougata Sarkar, who encouraged and helped me to pursue my research carrier.

I want to thank my batchmates Animesh, Amit, Anustup, Aditya, Ashish, Uttam, Dipanjana, Surabhi, Vinay for all the fruitful discussions and enjoyable times that we have spent together during the coursework.

It is difficult to put to words how grateful I am to my parents and family. They have always motivated me, nurtured me, and filled me with positive thoughts. It is their love and care that keeps me going no matter what the situation.

Preface

This thesis is organized into four chapters that describes the synthesis, characterisation, and multifarious applications of self-assembled metal-organic cubes and low molecular weight gelator (LMWG). The stabilisation of these self-assembly is restricted in soft gel state. These gels are evaluated in different disciplines starting from fundamental phase transition to versatile energy, environment-related applications.

Chapter 1 gives a brief overview of supramolecular gel and coordination polymer gels materials with driving force, classifications, structural importance and potential applications in various fields.

Chapter 2 discussed the synthesis, characterisation, and utilisation of a bidentate LMWG based on naphthalene diimide (NDI) core connected with two terpyridine units (Tpy-NDI) through amide linkage. This gelators connects each other with metal-ligand coordination bonds and result in a coordination polymer gel (CPG). A redox active, earth abundant Fe^{II} metal center is utilized for the construction of this CPG which shows fibrous nanostructure under electron microscope. The metal to ligand charge transfer (MLCT) spectra falls under visible light region and the DFT calculation shows a feasible excited state electron transfer from the metal-terpyridine units to NDI core. This Fe-Tpy-NDI CPG is employed for photoreduction of CO₂ in aqueous medium with triethylamine (TEA) and 1-benzyl-1,4-dihydronicotinamide (BNAH) as sacrificial electron donor. This CPG acts as an efficient heterogeneous catalyst for the production of CH₄ with a maximum rate of 2.75 mmol g⁻¹ h⁻¹ and 85% selectivity. Real time monitoring of this photoreduction process and detection of the possible through *in-situ* DRIFT spectroscopic study also in accordance with this photoreduction process.

Chapter 3 describes the design, synthesis, and characterisation of charge assisted H-bonding based hydrogel. The gelation study is performed with Ga-MOC and [Ni(en)₃]²⁺ complex, where strong hydrogen bond interaction between -NH₂ of ethylenediamine and -COO⁻ of imidazole-dicarboxylate made the self-assembled structure. This strong non-covalent interaction results in the spontaneous transformation from gel to crystal. The stoichiometric variation of the binder and the MOC is studied with rheology, which shows a gradual increment in the stiffness of the gel with an increasing amount of [Ni(en)₃]²⁺. A variation in the time of crystallisation is also found with different stoichiometric gel.

Chapter 4 reports the design, synthesis, characterisation, and gelation of a Ga^{III} based metal-organic cube (MOC). These MOCs get self-assembled in gel with the help of binder through charge assisted hydrogen bonding (CAHB). An ethylenediamine complex with redox-active metal center (Cu^{II}) is adopted as the binder for connecting Ga-MOCs in a particular array. This CAHB driven hydrogel shows a fibrillar morphology under the electron microscope and atomic force microscope (AFM). Upon standing, this kinetically metastable gel shows a spontaneous transformation into a thermodynamically stable crystal, and the transition is investigated with AFM. This heterogeneous gel is used as an electrocatalyst, and it exhibits intrinsic CO₂ reduction activity with high stability. A high faradaic efficiency of 92% is achieved for the production of CO. This electroreduction process is examined with possible intermediates detection through the *in-situ* DRIFT spectroscopic technique.

Table of Contents

DECLARATION	v
CERTIFICATE.....	vii
Acknowledgements	ix
Preface.....	xi
Chapter 1: Introduction	1
1.1 Gel materials: A brief overview.....	3
1.2 Driving forces for gelation	5
1.2.1 Hydrogen bonding	5
1.2.2 Hydrophobic and hydrophilic interaction	6
1.2.3 Electrostatic interaction	7
1.2.4 Host-guest interaction	7
1.3 Classification of Gel	9
1.3.1 Classification on the basis of solvent/medium	9
1.3.1.1 Hydrogel	9
1.3.1.2 Organogel	10
1.3.2 Classification on the basis of components	10
1.3.2.1 Polymeric gel	10
1.3.2.2 Metallogel	11
1.3.2.3 Nanocomposite gel	11
1.4 Applications of gel materials	12
1.4.1 Self-healing properties of gel materials	12
1.4.2 Chemosensing properties of gel materials	15
1.4.3 Gel materials as the drug delivery agents	16
1.4.4 Optoelectronic applications of gel-based materials	18
1.4.5 Gel materials as catalyst for organic reactions	21
1.4.6 Photochemical and electrochemical CO ₂ reduction with gel materials ..	24
1.5 Outlook	26
1.6 References	27

Chapter 2: Iron(II) based coordination polymer gel towards visible-light driven multi-electron photocatalytic CO₂ reduction 33

Abstract 35

2.1 Introduction 37

2.2 Experimental section 39

2.2.1 General 39

2.2.2 Electrochemical characterisations 39

2.2.3 Artificial visible light-driven CO₂ reduction 40

2.2.4 *In situ* diffuse reflectance FT-IR measurements 41

2.3 Synthesis 42

2.4 Results and discussion 47

2.4.1 Preparation of the organogel 47

2.4.2 Characterisation of the LMWG and organogel 47

2.4.3 Characterisation of the LMWG and Coordination polymer gel..... 52

2.4.4 Visible light-driven photocatalytic CO₂ reduction 58

2.4.5 Insights into CO₂ reduction mechanism 62

2.5 Summary 63

2.6 References 63

Chapter 3: Self-assembly of Ga-MOC and [Ni(en)₃]²⁺ by charge assisted H-bonding interaction: Understanding of Gel to Crystal transformation 67

Abstract 69

3.1 Introduction 71

3.2 Experimental section	73
3.2.1 General	73
3.2.2 Single-crystal X-ray diffraction	73
3.2.3 Powder X-ray Diffraction Measurements	73
3.2.4 Thermal Stability Measurements	73
3.2.5 Morphological analysis	73
3.2.6 Rheological analysis	73
3.2.7 ATR-IR Measurements	74
3.3 Synthesis	74
3.3.1 Synthesis of Ga(III)-Metal Organic Cube	74
3.3.2 Synthesis of tris(ethylenediamine)nickel(II) nitrate (Ni-EDA complex).....	75
3.4 Results and discussion	76
3.4.1 Gel to crystal transition,.....	80
3.4.2 Single Crystal X-ray Diffraction Analysis (SCXRD)	86
3.5 Summary	91
3.6 References	92

Chapter 4: Co-assembly of Ga-MOC and [Cu(en)₂(NO₃)₂] towards soft materials: Gel to Crystal transformation and electrocatalytic CO₂ reduction	95
--	-----------

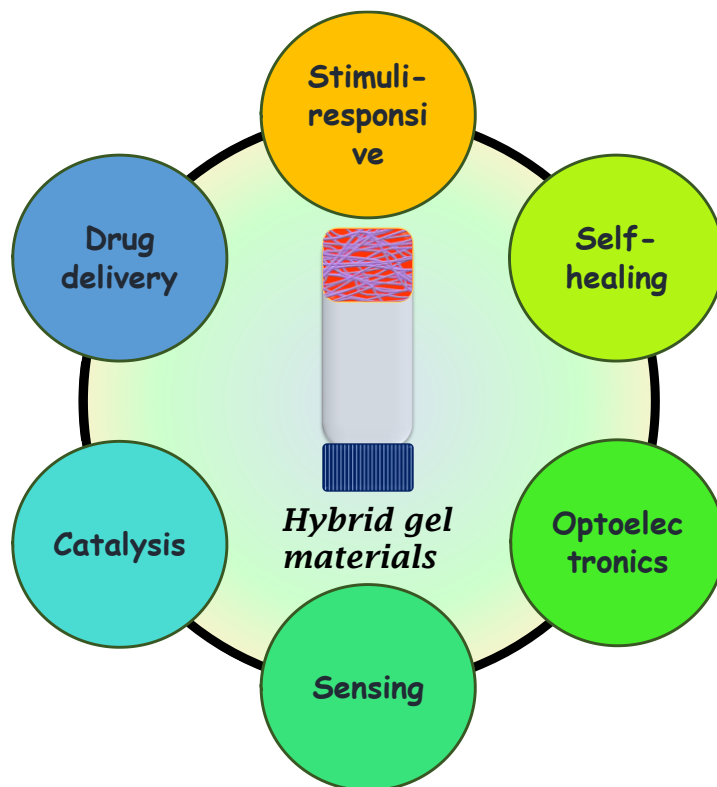
<i>Abstract</i>	97
-----------------------	----

4.1 Introduction	99
4.2 Experimental section	101
4.2.1 General	101
4.2.2 Single-crystal X-ray diffraction	101
4.2.3 NMR Measurements	101
4.2.4 Powder X-ray Diffraction Measurements	101

4.2.5 Thermal Stability Measurements	101
4.2.6 Morphological analysis	101
4.2.7 Rheological analysis	102
4.2.8 Zeta Potential Measurements	102
4.2.9 ATR-IR Measurements	102
4.2.10 Preparation of working electrode	102
4.2.11 Electrochemical setup	102
4.2.12 Chronoamperometric experiment	104
4.2.13 ¹ H-Nuclear Magnetic resonance analysis	104
4.2.14 Gas-Chromatography analysis	104
4.2.15 Turn Over Frequency calculation	105
4.2.16 <i>In situ</i> diffuse reflectance FT-IR measurements	105
4.3 Synthesis	106
4.3.1 Synthesis of Ga(III)-Metal Organic Cube	106
4.3.2 Synthesis of bis(ethylenediamine)copper(II) nitrate	107
4.3.3 Preparation of Ga-Cu hydrogel	107
4.4 Results and discussion	108
4.4.1 Single Crystal X-ray Diffraction Analysis (SCXRD)	113
4.5 Electrochemical CO ₂ reduction	118
4.6 Summary	126
4.7 References	126
Summary and Future Outlook	133
Biography	135

Chapter 1

Introduction



1.1 Gel materials: A brief overview

Gel is such a kind of substance having the properties of both solid and liquid; it has been recognized as a soft material with extensive application in daily life, starting from toothpaste, cosmetics, soft bioengineering, food industry, optoelectronics, and agriculture.¹⁻³ In general, gel is a colloidal cross-linked network withholding an enormous number of solvent molecules in its 3D matrix by immobilizing the flow of solvents.⁴ This solid-like viscoelastic nature of the gel can be easily realized by a simple inversion test method where it remains stable under the gravitational force when the gel pot is kept upside down. Rheological test can also be performed to derive a conclusion about the gelation. A higher value of elastic storage modulus (G') than that of loss modulus (G'') indicates the viscoelastic property of the gel.⁵ From the last few decades, there has been an upsurge in the design and development of gel materials for interdisciplinary applications.⁶ A bottom-up approach is generally employed to construct the self-assembled structure of the gelators into a solid-like phase, and the interstitial vacant spaces are occupied by the fluid (Fig. 1). This self-assembly is formed by the influence of different types of non-covalent interactions such as hydrogen-bonding, π - π stacking, electrostatic interactions, and host-guest interactions.⁷ These supramolecular gels also show good reversibility towards different stimuli like pH, thermal, and mechanical force due to the dynamic properties of the weak non-covalent interactions.⁸ For the gelator molecules with π -electron enriched moieties (pyrene, anthracene, naphthalene, porphyrin, tetrathiafulvalene, etc.), the gelation is primarily driven by the π - π interaction.³ However, two oppositely charged species interconnect electrostatically and result in gel formation.⁹ Molecules containing functional groups such as amide,¹⁰ amine,¹¹ hydroxyl, amino acid,¹² sugar-derivatives¹³ are also well known to form gel with the help of hydrogen-bond donation acceptance capacity. There is another class of gel directed by the covalent interaction, known as chemical gel. Polyamide, polyester, poly(vinyl alcohol), etc., can form strong chemical bonds between the polymeric units and lead to gelation.^{14,15} Whereas, these polymeric gels are not suitable due to their low processibility and irreversible nature. In this context, low molecular weight gelator (LMWG) and metal-organic cubes can be suitable candidates for processable gel materials. Gelators that form self-assembly in organic solvents and water are commonly known as organogels and hydrogels, respectively. These gelators show beautiful architecture in their self-assembled state. Micro and nano-structuring of the gel consist of fibers, 2D nano-sheets, spheres, nano-ribbons, and nano-scrolled morphologies. These nanostructures further interconnect each other to form a 3D network that finally encapsulates

the liquid phase and allows a viscoelastic nature. Under different stimuli applications, these supramolecular structures undergo destabilization and lead to a phase transition from gel to sol, which is again reversed back to its original gel phase with some internal rearrangements.^{16,17} There is another possibility, not to return into the gel state rather, it undergoes a close ordered packing to form a crystalline state.¹⁸ These gel to crystal transitions are often found to be spontaneous in nature without the application of external stimuli.¹⁹ The gel state is considered as a kinetically trapped metastable state that can undergo a phase transition to a thermodynamically more stable crystalline state. Several reports suggest that the strong non-covalent interactions act as the key factor to start the crystallisation process.^{20–22} Most of the LMWG are found to be amphiphilic in nature. The solvophobic part tries to assemble them with each other, whereas the solvophilic part is exposed to the solvents, leading to gel formation. A perfect balance between these two opposite phenomena helps the molecules to gelate. This solvophobic counterpart of the LMWG also plays a vital role in the phase transition from gel to crystal.

Therefore, designing the new gelator molecule and studying their supramolecular assembly with the phase transition phenomenon will be an exciting approach to understand the processable soft materials. These gel materials, which consist of metal ions, have been used for different applications such as optoelectronics, chemosensing, bio-imaging, drug delivery, self-healing, electrocatalysis, and photocatalysis.^{23–25} These supramolecular gels are interesting to study in a precise way due to their easy synthetic tunability, sol-gel reversibility, and high solution processibility. Many metallo-organogels containing the redox-active center show an excellent application in the field of catalysis, starting from organic reactions, electrocatalysis, and photocatalysis. This overall flexible nature of the metallogel with superior capability can pave way for the development of cost-effective materials in a diverse application field.

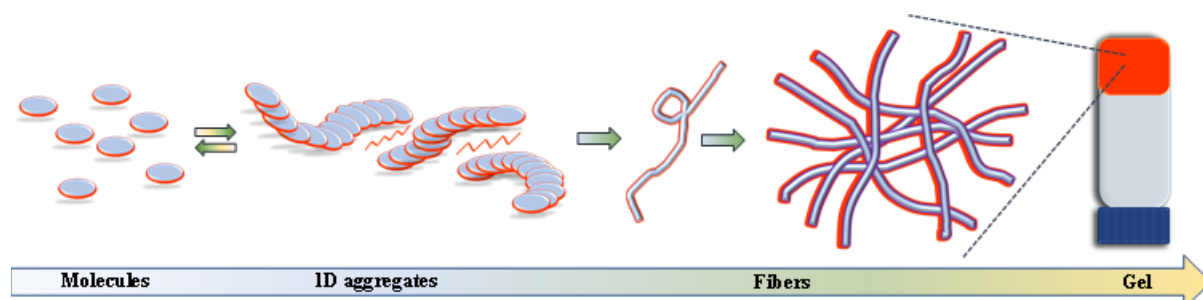


Figure 1. Bottom-up approach of self-assembly process of the LMWG to supramolecular gel.

1.2 Driving forces for gelation:

1.2.1 Hydrogen bonding: The hydrogen bond is a type of non-covalent interaction that is much weaker than a typical ionic and covalent bond and stronger than the van-der-Waals interaction. A hydrogen atom located in between two atoms with a high electron affinity can form hydrogen bonding. This type of non-covalent interaction plays a significant role in the formation of supramolecular architectures.^{26–28} Hydrogen bond is not only crucial for the structural property correlations but also well known for various molecular recognition process bio-macromolecular systems.²⁹ This short and directional interconnection between the donor and acceptor is also extensively employed in the crystalline extended metal-organic architectures, metal-organic cage, and supramolecular gel. Hydrogen bonds are also well-known for showing an interesting dynamic property, where breaking and reforming the bond is stimulated by external forces. This phenomenon is employed to construct self-healing soft materials.³⁰ It is a ubiquitous supramolecular interaction employed in the supramolecular gels. There are several examples of gelators with multiple hydrogen bond donation-acceptance sites. The most commonly used functional groups which are employed for the gelation are as follows, amide, hydroxyl, amine, carboxylate, peptides, sugar-derivative, etc. In this context, urea and thiourea groups are promising candidates to form an extended structure with the help of constructing strong hydrogen bonds. Not only the neutral functional groups participate in the hydrogen bonding rather two oppositely charged species can also form a strong hydrogen bond, which is commonly known as charged assisted hydrogen bonding (CAHB). In a review article, Andrew D. Hamilton *et al.* described the importance of the hydrogen bond in the formation of the primary and secondary structure of a self-assembled organo-hydro-gelator (Fig. 2a).³¹ Where they showed a urea-based organo-hydro-gelator forming primary self-assembled linear chain organisation, and those fibrils expand into a secondary structure with the help of weak hydrogen bond and van-der-Waals interaction, thus inducing the gelation.

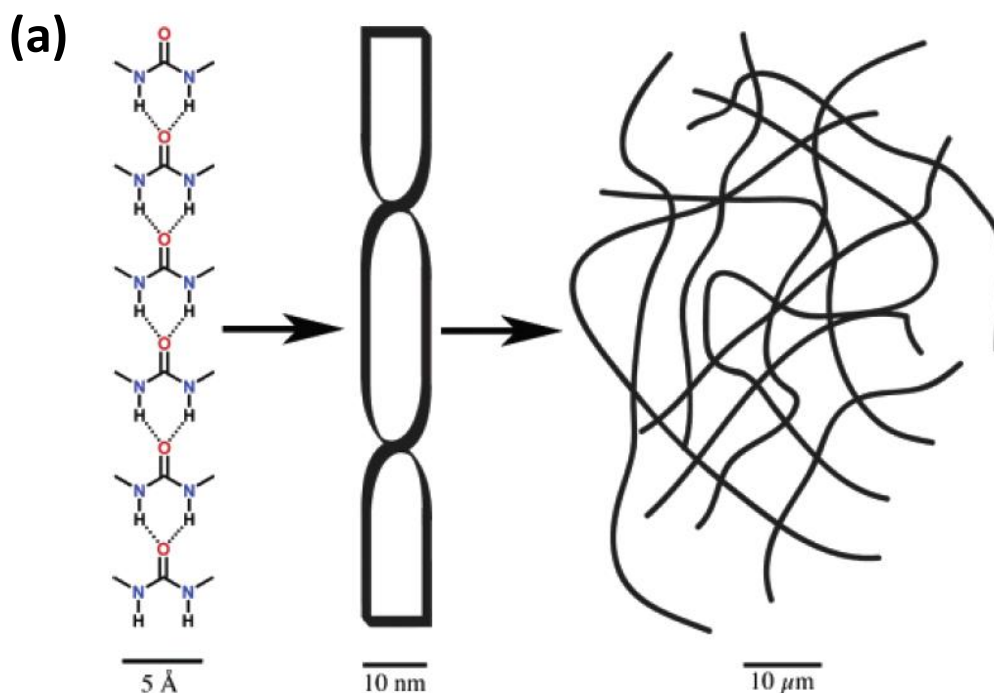


Figure 2. (a) Primary, secondary, and tertiary structure of the self-assembled supramolecular gel. Figure reproduced from ref. 31 with permission.

1.2.2 Hydrophobic and hydrophilic interaction: The gelators that form the hydrogel are often amphiphilic in nature. These have two types of functional groups hydrophilic and hydrophobic. The hydrophilic part tries to take the molecules into the solution state, whereas the hydrophobic moieties hold them in a self-aggregated fashion.³² The perfect balance between these two forces leads to gel, an in-between state solution, and precipitate. Hydrophobic interaction plays a crucial role in forming large biological assemblies in water to form a hydrogel. As they are amphiphilic molecules, they form micelles in lower concentration and higher concentration, self-assembled into a cross-linked structure. The gelation concentration is not only dependent on the hydrophilic and hydrophobic forces but also controlled by components present in the water solution (e.g., salt, pH, surfactant). The hydrogelators with amphiphilic groups also have a high degree of toughness in the association and, therefore, are able to show self-healing properties. Zang and co-workers showed a physical double network hydrogel, where they have used a triblock copolymer. The hydrophobic groups at the two ends and the hydrophilic core poly(methacrylic acid) consist of -NH_2 groups for hydrogen bonding help to form the supramolecular cross-linked network. The hydrophobic unit of the gelators also helps to hold some drugs molecules, and a release of these can be achieved in a controlled way. Tsitsilianis and co-workers showed hydrogels' formation from polystyrene-*b*-poly(sodium acrylate)-*b*-polystyrene (PSt-*b*-PNaA-*b*-PSt),

which is a triblock copolymer. Micellar structures were formed below 0.2% concentration, while weak gels were obtained above 0.4% concentration.

1.2.3 Electrostatic interaction: Electrostatic interaction is widespread in constructing supramolecular architectures.^{33–35} Hydrogelators having charges are readily soluble in water. When two oppositely charged units come into the same solution, those can form a supramolecular self-assembled structure with the help of electrostatic interaction. A polymeric chain with ionic counterparts at the end is known to form hydrogels. The ionic monomers can form the complex cluster that ends up with the cross-linked arrangements while the other groups remain in the solution. However, electrostatic forces are not very common for the formation of organogel due to the lower solubility of the ionic groups in the common organic solvents. Aida and co-workers showed the formation of organogel with some dendritic molecular binders having guanidium ions at the end. The organogel is formed with the help of hydrogen bonding along with the electrostatic interaction with the anionic clay, which leads to cross lining hydrogel. Boulmedais and co-workers exhibited the formation of hydrogel driven by electrostatic forces.³⁶ A quaternary ammonium polymer (PAH) interacts electrostatically with a Fmoc-FF peptide consisting of anionic phosphate groups. The gel was formed just after adding the two components at a particular molar ratio (PAH monomer/Fmoc-FF) peptide of 8. They also showed that the formation of viscous liquid with a molar ratio indicates non-sufficient weak interaction between the cationic ammonium groups and the anionic phosphate groups. The hydrogel shows a shear-thinning behaviour, where, the application of shear stress, the cross-linked structure broke and it again reform after removal of the stress. Hennink *et al.* showed the formation of hydrogel with two oppositely charged dextran microsphere and methacrylic acid.³⁷ Gelation takes place after mixing the two oppositely charged microsphere with same equivalent by keeping the pH 7.

1.2.4 Host-guest interaction: Another crucial interaction is found to be common in soft supramolecular materials, i.e., host-guest interaction.^{38,39} This is nothing but a combination of hydrogen bonding and electrostatic interaction. This specific interaction has unique characteristics like particular geometry, strong binding affinity, etc. Moreover, it is also found that these associations are sensitive to different external stimuli like pH and heating and the presence of different metal ions, which makes them more attractive in the biomedical application as the drug delivery agent. Cyclodextrin is a promising candidate due to its inner hydrophobic and outer hydrophilic nature and its easy commercial availability. It can also accommodate the hydrophobic molecules in the aqueous solution, which will end up with the

aggregated cross-linking state. Several other examples can be found among them; crown ether and cucurbituril are very common for the formation of a hydrogel. In a recent article, Baker *et al.* showed a hydrogel formation with the help of host-guest interaction between cyclodextrin and adamantane.⁴⁰ The cyclodextrin host was connected with an alginate polymeric chain, and the adamantane was covalently connected to the polyethylene glycol chain. With the increasing number of multivalent cross-linker guests, gelation was found to be started and resulted in a robust gel. With the maximum number of cross-linked structures, it was obtained that the gel is resistant to mechanical forces and shows self-healing properties. Ajayaghosh and co-workers demonstrated the formation of hydrogel with the same cyclodextrin and a coordination polymeric unit.⁴¹ A coordination polymer formed by the azomonocarboxylic acid and Mg^{2+} acts as the host, and the cyclodextrin, which accommodates the benzene ring of the azo group, acts as the guest. Here they showed a precise stepwise release of cyclodextrin molecule from the hydrogel driven by the temperature stimuli. Kim *et al.* used cucurbit[6]uril-conjugated with hyaluronic acid and diamino-hexane conjugated hyaluronic acid for the in-situ formation of hydrogel inside the cell (Fig. 3a-c). This was applied in cellular engineering, and cell imaging was done by the modified fluorescein isothiocyanate cucurbit[6]uril.⁴²

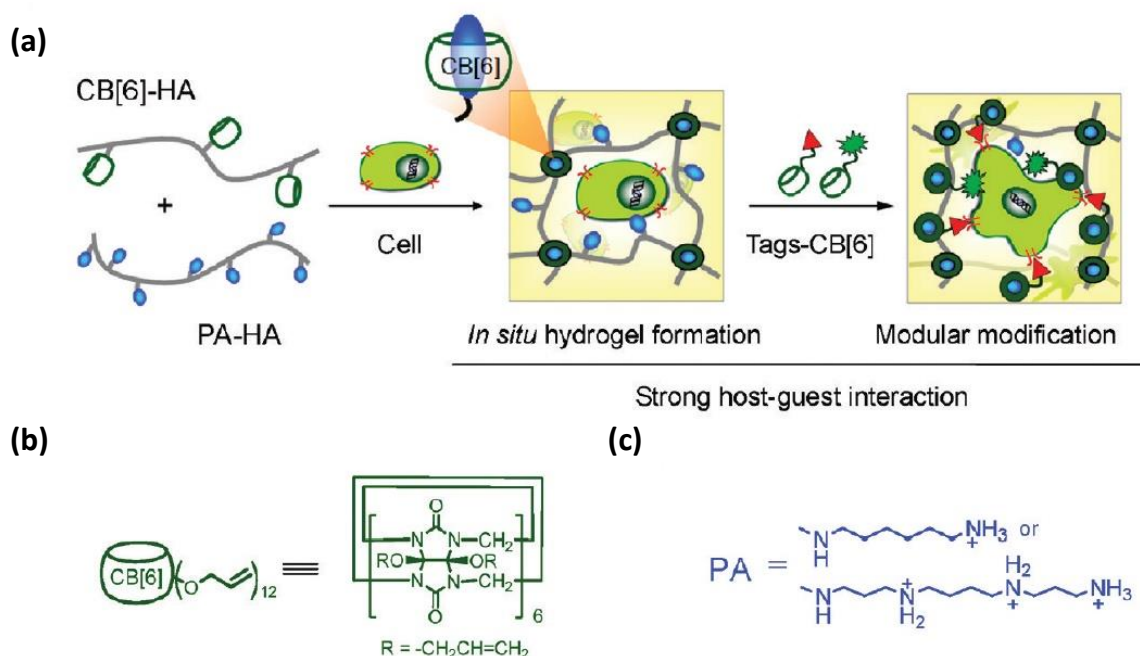
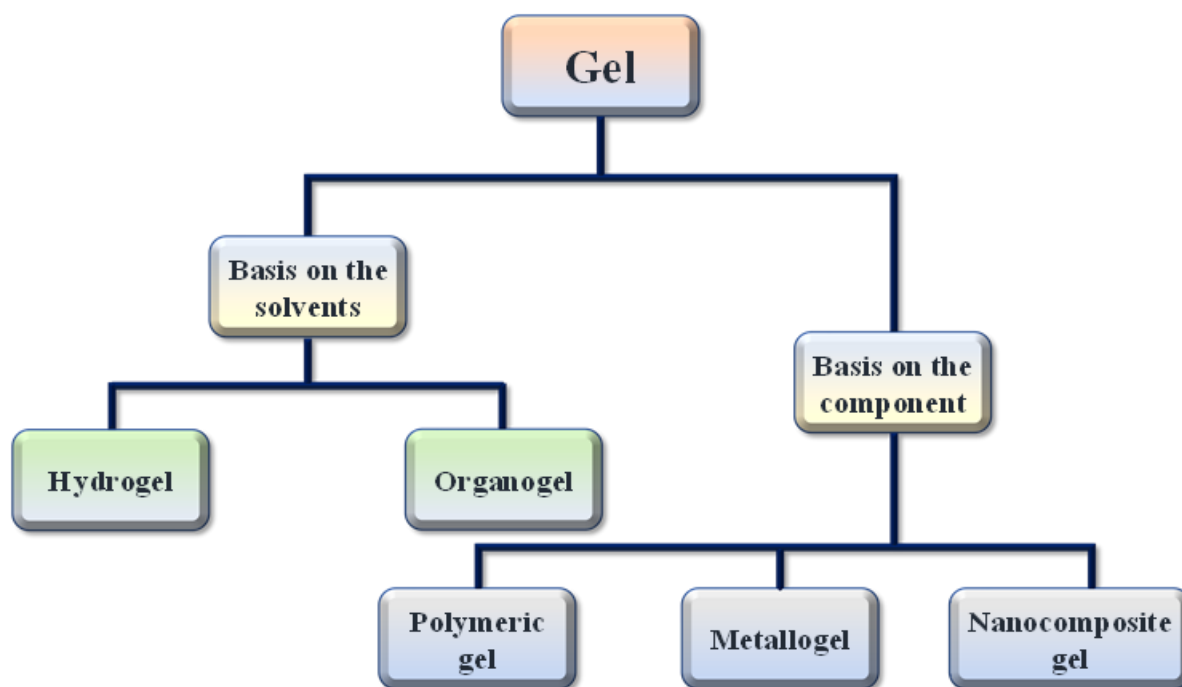


Figure 3. (a) Schematic representation of the in-situ formation of the biocompatible hydrogel by the host-guest interaction. (b) chemical structure of cucurbit[6]uril. (c) Polyamines of diamino-hexane and spermine. CB-HA=cucurbit[6]uril-conjugated hyaluronic. Figure reproduced from ref. 42 with permission.

1.3 Classification of Gel:



Scheme 1: General classification of gel materials.

1.3.1 Classification on the basis of solvent/medium:

Depending on the nature of the solvent, the gel materials can be divided into two categories. Most of the gelation is performed with a water medium or in a mixture of organic solvents. These two categories are named as hydrogels and organogels.

1.3.1.1 Hydrogel: As discussed earlier, a hydrogel is an extended network constructed by the self-assembly of the gelators, which are able to hold a large volume of water.⁴³ This 3D cross-linked network is made up of only gelator and sometimes gelator along with the linker molecules with the help of different covalent and non-covalent interactions.⁴⁴ A high-water content (>90%) in the hydrogel matrix makes it more flexible and tuneable in nature. Due to the high-water contents, it can be utilized as a stimuli-responsive soft-smart material in comparison with natural tissues. These 3D cross-link networks formed by different types of non-covalent interactions such as hydrogen-bond, hydrophobic, hydrophilic, and host-guest interactions can also provide self-healing properties.^{45,46} A change in the volume with the phase transformation from gel to sol by the stimulation can serve as sensors and actuators. Due to ease of handling of the substance, sometimes the gel state is transformed into its solid phase, popularly known as xerogel. In the xerogel 3D matrix, the porous micro or nanostructure remains intact as in the gel, but the solvent molecules are replaced by the air.⁴⁷

There are several techniques to perform this transformation and replace the solvent in supercritical conditions like critical point drying (CPD) and freeze-drying method. This results in a porous, low dense, 3D cross-linked network. However, high-temperature vacuum condition is also used as a drying technique to afford xerogel. This high temperature creates viscous sintering in the gel matrix, which leads to a more densely packed 3D network and produces a more robust solid. Therefore, depending on the drying conditions, we can modulate the density and porosity of the gel matrix.

1.3.1.2 Organogel: In general, organogel is a viscoelastic material with a large volume of organic solvents immobilized into the 3D interconnected network made up of self-assembled LMWG.^{48,49} A pure organic solvent or a solvent combination is chosen depending on the gelator solubility and the critical concentration of the gelation. Organogels show diverse supramolecular nano-architecture under microscopic techniques, such as FESEM, TEM, and AFM. This diversity makes them a promising candidate for various application fields like the food industry, medicine, tissue engineering, control drug release, and catalysis.⁵⁰⁻⁵² In recent years, chromophoric unit-based organogel has been gaining immense interest in optoelectronics, sensors, energy transfer, and light-harvesting applications.

1.3.2 Classification on the basis of components:

1.3.2.1 Polymeric gel: This class of organogel comprises of polymers of small monomeric units. The lamellar structure of these polymeric units can hold a copious amount of solvents molecules, which results in gelation. These entangled chains of different molecular weights of polymers are distributed homogeneously in the solvent medium. Some polymers are (polysiloxanes, polycarbonates, polyethers), well known for suitable gel preparation.⁵⁰ Other than that, the π -electron rich aromatic units are also used for the gelation based on their individual identities, such as functional dyes, photoresponsive chromophore, heterocyclic chromophore units, and fused polyaromatics.^{53,54} Some small molecules like pyrrole, aniline, thiophene are also very popular to form the polymeric chain, which leads to the formation of a polymeric gel. Natural and synthesised proteins, carbohydrates, and other peptide derivatives also have the π -electron rich core and functional amide bonds, also capable of forming self- aggregated supramolecular assembly that can immobilize the solvent molecules inside it. The interesting photophysical properties of the organogelators make them more appealing for catalysis, light-harvesting applications, and optoelectronic applications. Therefore, several organogelators have been reported with different chromophore parts, such

as pyrene, anthracene, porphyrin, phthalocyanine, coronene, phenanthroline, stilbene, thiophene, tetrathiafulvalene, phenylene, phenylenevinylene, phenylene-acetylene, etc.^{55–59}

1.3.2.2 Metallogel: The indirect and direct involvement of the metal ion coordination with the gelator ligands can form a kind of gel, broadly known as metallogel.²⁴ We can subdivide this class of gels into two categories, i) discrete metal complexes or polyhedra self-assembled through different non-covalent interactions by the help of linker molecules, and ii) metal ions coordinated LMWG results in a coordination polymer, which can hold a large amount of solvent within it, known as coordination polymer gel (CPG). In the first subclass of metallogel, metal ions are not directly involved in the self-organization process. The polyhedra or the cages are made up of metal ions held by multidentate macromolecular ligands. It consists of some metal-organic cages connected with each other through some binder molecules by supramolecular interactions or by coordinating some vacant metal sites. Recently, this CPG has been emerging as a popular metallogel due to the involvement of electron-rich chromophoric units and redox-active metal centers.⁶⁰ Here, the metal ions actively participate in forming gel networks. The incorporation of the metal ions also expands the research area towards different supramolecular architectures and rheological behaviour. Designing the LMWG needs a central core and metal coordinating units covalently connected to each other. The sol-gel reversible nature and various morphological nanostructures facilitate their utilization of CPGs to fabricate a large display and sensing device. The stimuli-responsive behaviour of CPGs makes them a superior drug delivery agent. The advantage of the metal ions in these organic-inorganic hybrid materials made them a promising candidate in the field of redox, optical, electronics, magnetism application.^{61–63} Depending on the different metal ions in these soft materials, the application properties can be tuned towards optoelectronics, pharmaceuticals, and catalysis.⁷ Therefore, a rational design of novel metallogel with new LMWG or metal-organic polyhedra is of utmost interest.

1.3.2.3 Nanocomposite gel: The implantation of nanoparticles, clay materials, or other nanostructures in the cross-linked network of the gel matrix leads to nanocomposite gel. These nano components are generally connected to the gel through different kinds of non-covalent and covalent interactions. These heterogeneous nano-constituents can be carbon-based 2D materials, clay particles, or metal nanoparticles. Recently, these hybrid nanostructured soft materials are gaining more interest due to their wide range of applications. Based on the components embedded in the gel structure, it can be used in a vast field of applications with enhanced physical, chemical, electrical, magnetism, biological

activity.^{64–67} Metallogels and hydrogels can act as the template for stabilizing the metal nanoparticles, which results in well-dispersed nanoparticle decorated metallogel nanocomposites. The introduction of the nanoparticles inside the supramolecular gel widens their application field, particularly towards catalysis. In addition to the nanoparticles, different kinds of clay particles are also introduced inside the gel matrix. The resulting gel shows excellent self-healing properties. Over the past decades, various photosensitizer and photocatalytic centers are also introduced into these soft materials to get enhanced photocatalytic performance with the porous cross-linked network structures.

1.4 Applications of gel materials:

The self-assembly of the low molecular weight gelators to supramolecular gel network gained considerable attention from materials to medical chemistry. These multifunctional soft materials have wide applications in optoelectronics, self-healing materials, drug delivery agents, molecular sensors, organic catalysis, photocatalytic, and electrocatalytic chemical processes. The below section will discuss about these all with suitable examples.

1.4.1 Self-healing properties of gel materials: The natural healing ability over any damage by the application of an external force is a very common phenomenon in living organisms. Therefore, the development of these kinds of artificial self-healing substrates is much promising in biomedical applications and device fabrications.^{68,69} Over the last few decades, gel materials have attracted considerable attention as a proper candidate because of different non-covalent supramolecular interactions in the gel. Harada and co-workers showed a redox-active self-healing gel constructed with the host-guest interaction.⁷⁰ The polymer taken as a guest for hydrogelation was performed in buffer with pH 9. Next, they have speculated on the self-healing nature of the self-standing hydrogel (Fig. 4a). Rheological experiments were performed both before and after the healing, which indicated no relaxation for the hydrogel during the reconstruction. When they kept two cubes of that hydrogel in an attached position for 24 hours, it came as a single block. The detached host and guest counterpart were free at the edge of the cutting area, which again interacted with each other to reconstruct the hydrogel.

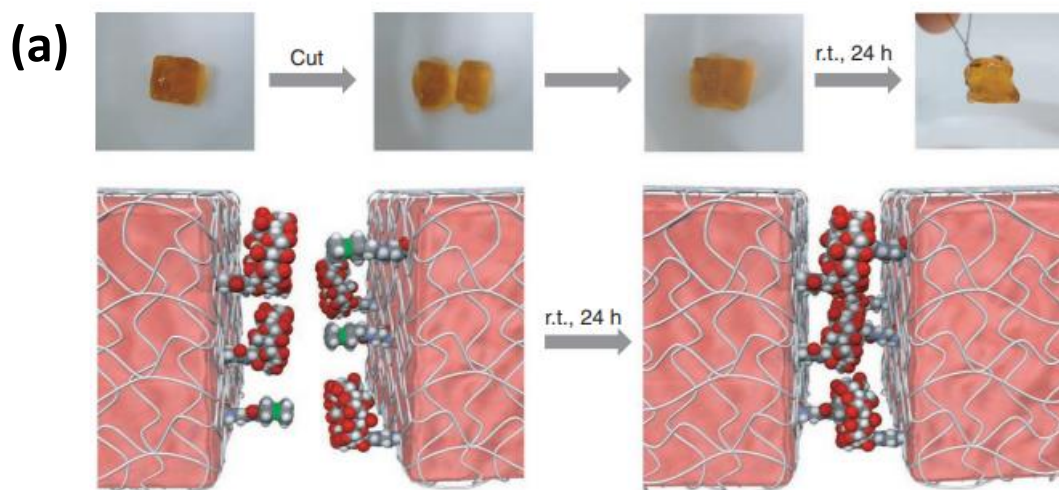


Figure 4. (a) The self-healing nature of the hydrogel after standing for 24 hours. The schematic of the host-guest interaction between cyclodextrin and ferrocene at the cut edge. Figure reproduced from ref. 70 with permission.

Aida *et al.* show a self-healable hydrogel made up of macromolecular dendrimer as the binder, sodium polyacrylate, and clay nanosheets.⁷¹ The binder has two dendron units decorated with guanidium ions. These dendron units were named as molecular glue, which can interact with each other with the help of salt-bridge interaction. They achieved a quick recovery of the initial storage modulus (G') value, which is much more difficult for other copolyptide gels. Interestingly, they found that when they attached two cutting parts, it healed, but two fresh surfaces were not attached to each other. Also, the two cut surfaces could join when they connect quickly, just after fresh cutting. The 3D cross-linked structures were made up of binding of the pendent guanidium groups with the sheets of clay. This architecture helps the hydrogel recover fast and does not need the rearrangements of the organic component. Gunnlaugsson *et al.* showed a highly luminescent self-healable metallogel (Fig. 5a-h). The gelation was performed with pyridine-2,6-dicarboxylic acid derivative (H_2L) and lanthanides ($Ln = Eu^{III}$ and Tb^{III}).⁷² Both gels show individual luminescent properties, and an equal mixture of these two lanthanides gave rise to a yellow-orange coloured gel. Both of the gel was cut into two parts and, when it was kept in contact, showed a self-healing property without any external stimuli.

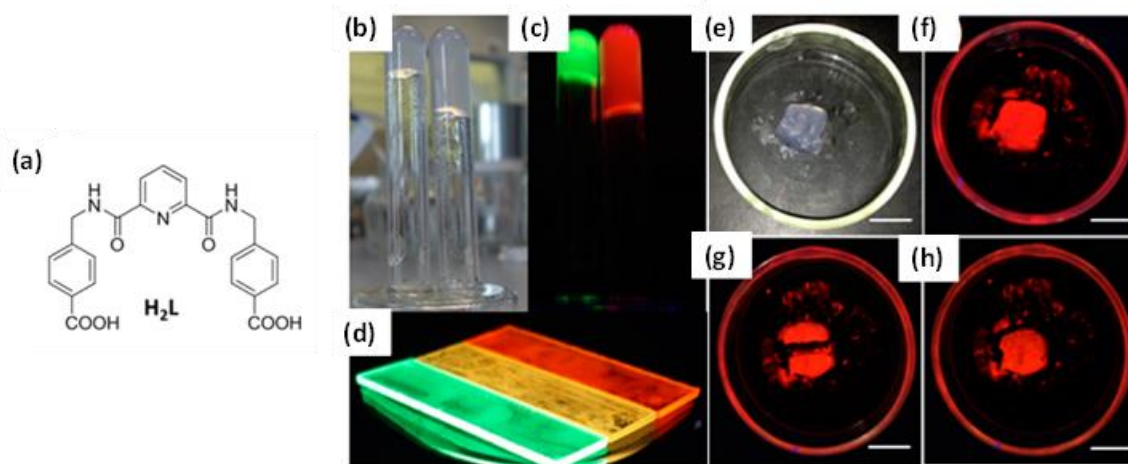


Figure 5. (a) The structure of the LMWG. (b) gelation with Eu^{3+} and Tb^{3+} under daylight conditions. (c) Gels under UV light. (d) Luminescence properties of Eu^{3+} , $\text{Eu}^{3+}/\text{Tb}^{3+}$, and Tb^{3+} gels. (e-h) Self-healing properties of the gel under daylight and UV light conditions. Figure reproduced from ref. 72 with permission.

A. Banerjee and his team have reported a series of metallo-hydrogel made up of tyrosine-based amphiphiles.⁷³ The gelation was found to be very selective towards Ni^{2+} . They also observed a significant change in the mechanical property and stiffness of the gels when the carbon chain length was varied from 10 to 14. Gelation was performed in phosphate buffer solution with a pH of 7-8. The amphiphile had a lower chain length took much more time for the gelation upon resting after sonication of two precursor solutions. This nickel-based metallo-hydrogel showed an excellent self-healing property. When the gel was cut into several pieces and kept in contact with a moderate press, it was observed that the cut area was healed fully, and the whole gel structure could be lifted with the help of a needle. Here also, the chain length affected the self-healing properties. The healing process was delayed with a lower chain length, but for the longer carbon chain length, the healing was completed within 5 min. Presumably, the hydrophobic interaction also plays a significant role in gelation and self-healing. Therefore, it happens with the longer carbon chain much faster within the water medium. Therefore, these gel materials can mimic nature, and this interesting phenomenon can act as a potential agent in different fields of application.

1.4.2 Chemosensing properties of gel materials: The chemosensing application of the gel is one of the most exciting applications in the field of these soft materials. The presence of different functional groups and the different photophysical properties within the gel systems make them a suitable candidate in this particular application field.^{74–76} Such change in some properties of the gel with the addition of the different external agents, which are sensitive to

the naked eye, can provide specific information for that particular contaminants. The soft nature of the gel structure for an easy change into a different phase like sol or sometimes change in the luminescent properties makes them an excellent candidate for the detection of different toxic gases, heavy metal ions, and other hazardous chemicals. Berke *et al.* reported a metallo gel with the property of sensing different nitroaromatic compounds.⁷⁷ Conventional heating and cooling method, when applied to the DMF solution of 1,4,5,8-triptycenetetracarboxylic acid with $\text{Al}(\text{NO}_3)_3 \cdot 9\text{H}_2\text{O}$, leads to gelation after one hour. Next, the metallo gel was investigated to sense the different nitroaromatic compounds, and it shows an excellent sensing property towards picric acid. The gel was emissive, and the photoinduced electron transfer (PET) process made the system much more efficient with fluorescence quenching for this application. The increasing number of nitro groups within a phenyl ring made them more electron-deficient, and the low line lowest unoccupied molecular orbital (LUMO) level made the PET process much easier. Therefore, the picric acid having three nitro functional groups has the lowest LUMO level, and the gel shows the effective detection with the highest quenching percentage. Shinkai *et al.* reported a Co-based metallo gel prepared from a LMWG (1,2,4,5-tetra(2H-tetrazole-5-yl)-benzene) and CoBr_2 .⁷⁸ This metallo gel acted as a chemosensor for chloride-containing molecules, like HCl , SOCl_2 , COCl_2 , and $(\text{COCl})_2$. They had also prepared a portable chemosensor kit by filling a capillary with the gel and closing the ends of the capillary with membrane filters. The capillary was exposed to phosgene gas, and after that, the capillary colour changed from red to blue. In a very recent article, Maitra and the co-worker showed the sensitization of H_2O_2 at the micromolar level with a paper disc coated with the sensitizer hydrogel.⁷⁹ They have used the photoinduced energy transfer process with the help of biphenyl carboxylic acid and terbium ions (Tb^{3+}) in this sensitization process (Fig. 6a-c). A hydrogel made up of biphenyl carboxylic ester, terbium nitrate, and sodium cholate was coated on a paper disc, showing a luminescent property under UV light when exposed to H_2O_2 . The proposed mechanism indicates first the oxidation in the presence of H_2O_2 followed by deboration and fragmentation, which leads to the formation of the biphenyl monocarboxylic acid. This carboxylic acid can coordinate the terbium ions and a feasible energy transfer process can take place according to the Latva's empirical rule. Lack of this interaction helps the ester to remain silent towards sensitization. This chemical reaction is also quantitatively sensitive toward H_2O_2 , which shows an emission intensity increment with the increase in the concentration of H_2O_2 .

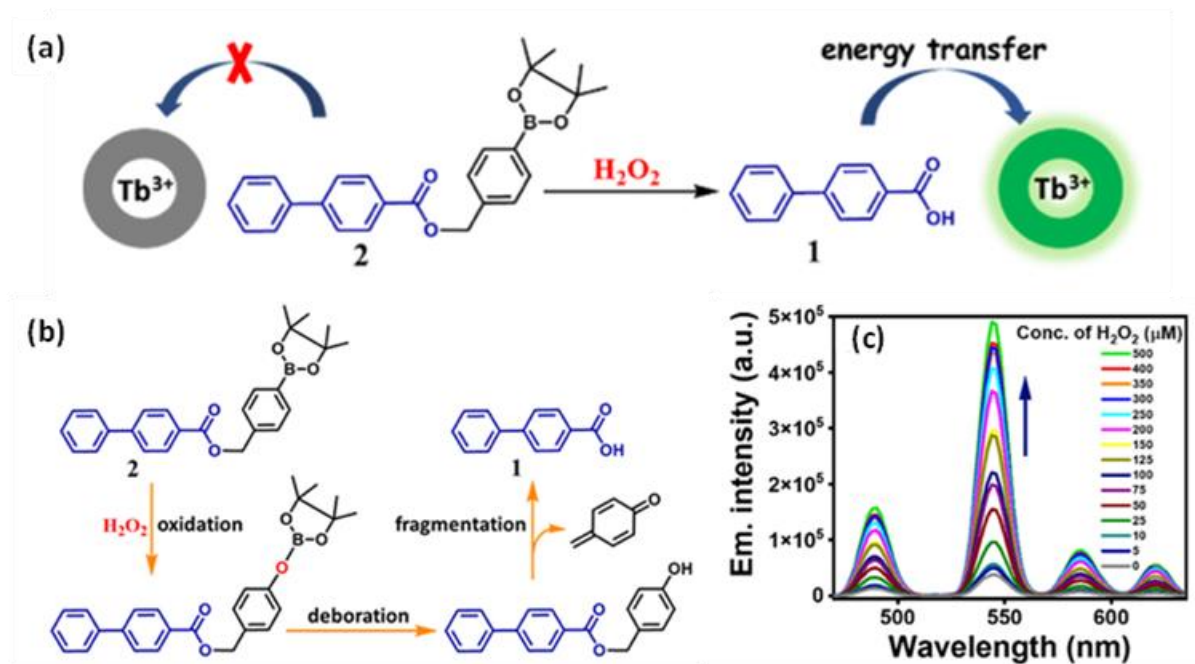


Figure 6. (a) Schematic of the H_2O_2 sensing with the terbium-based gel. (b) The reactions involved in the sensing process. (c) Increase in emission intensity with the concentration of H_2O_2 . Figure reproduced from ref. 79 with permission.

1.4.3 Gel materials as the drug delivery agents: Delivery of a drug to a particular location with the help of a metal-organic or pure organic soft materials has been at the forefront of research in the biomedical field for the last few decades.^{80–82} It is challenging to develop a new material that can act as a drug-delivery agent in a well-controlled manner. Recently the metal-organic cage-based gel and polypeptide-based gels are emerging as potential agents for acting as the host for the drug molecules and are also capable of a controlled release. The metal-organic polyhedras are appealing in this field due to their analogous character with the enzymes or other large biomolecular systems for encapsulating guests in a confined way. These cages also have the advantage of size selectivity. Stimuli-responsive gels, such as different coordination polymeric gels, are also reported as the drug-delivery agent with the controlled release of drug triggered by some physical and chemical perturbation (like pH, ionic strength, temperature, mechanical force, etc.). Here one has to consider also the toxicity of the vehicle of the drug, and because of that, most of the metal-containing materials and polymeric materials get failed though they have the encapsulating capability and controlled release nature. Banerjee *et al.* showed a tetrapeptide-based hydrogel for a controlled release of the doxorubicin drug, which is considered a potential anti-cancer drug and also acted against gastric carcinoma (Fig. 7a-c).⁸³ The hydrogels were able to entrap 13.79×10^{-3} (M) drug solution at the lowest gelation concentration. Next, they have studied the controlled

release of the drug at the physiological pH. In this regard, they covered the drug-loaded hydrogel into the PBS buffer with a pH of 7.46. The diffusion rate was calculated by fitting the data with a nonsteady state diffusion model equation. The hydrogels showed the highest 90% of drug release at 45 hours. Similarly, they have also performed the drug release kinetic at the acidic pH of 6.5, and it shows the highest release of 80% after 35 hours.

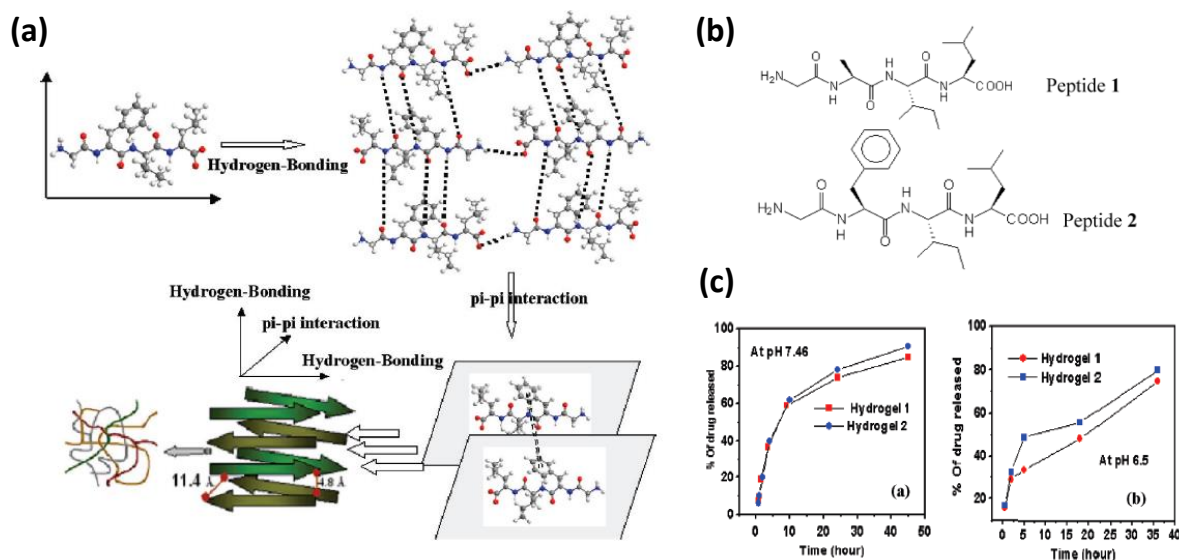


Figure 7. (a) Schematic highlighting the molecular packing in gel state. (b) Chemical structures of the gelators. (c) Drug release profile of the hydrogels. Figure reproduced from ref. 83 with permission.

The same group has also studied the effect of the chiral center present in the hydrogelator in the drug release kinetics.⁸⁴ A tripeptide-based nontoxic hydrogelator they have synthesized with all possible arrangements of the chiral center. Three of the four enantiomeric pairs show gelation properties with different mechanical strengths. A detailed rheological study of all the gels and sols indicates that as the D-phenylalanine residue moves from the N to C terminus, the gel stiffness decreases with the decreasing interaction of H-bonding and π - π stacking. This study tells that the mechanical strength of the gel can be tuned by placing the chiral residue in a particular position of the gelator. The gel's stiffness also affects the drug release performance of different gels. The same amount of Doxorubicin was loaded into each gel, and the release of the drug was monitored. The release curve shows a similar nature for all the enantiomers, but it is found to be different for the diastereomers. They obtained a maximum of 76% of drug release after 79 hours. Therefore, the position of the D-residue in the gelator determines the mechanical strength and controls the gel's drug release properties. Most of the time, the drug is loaded on a vehicle such as a polymer gel matrix before the delivery. But sometimes, it is found to be cytotoxic and carrier material degradation. Dastidar *et al.* showed that the drug itself could be transformed into the gel by a

non-trivial modification to a pro-drug.⁸⁵ These pro-drugs can show self-release properties. They have employed the 1D hydrogen bonding network approach for the formation of the gel. Naproxen, a well-known drug, was used along with its two β -peptide derivatives and allowed them to react with different primary and secondary amine to obtain the salt. Among all of these salts, five were able to show the gelation properties. A particular salt derivative of the parent drug was chosen to check the activity towards skin inflammation, and it displays a similar activity as the parent drug. Next, the self-delivery property of the chosen drug was evaluated on the skin inflammation of the mice. A daily dose of 1 mg/day of the gel-treated mouse shows a good skin recovery within 10 days, whereas the mouse without the gel treatment was found to be dead after 2 days.

1.4.4 Optoelectronic applications of gel-based materials: Optoelectronics materials are generally deal with electronic systems by means of different utilizations such as tunable light emission, sensing, transmitting, etc. Hence, metal-organic soft materials can be a promising agent in this type of application. The emission properties of gel materials can be generated from two sites i) metal center^{63,86–88} and ii) chromophore⁸⁹ part of the ligand molecules. The emission properties of the gel can be tuned as the emission of the metal center is depends on the coordination environments. The emission can also be modulated by synthetic modification of the chromophoric unit of the gel matrix. Apart from this, the different charge transfer (CT) bands, aggregation-induced emission, guest-induced emissions, and inclusion of the photoresponsive molecules are also reported for these kinds of soft materials. Maji and co-workers showed the formation of organogel in a methanol/dichloromethane mixture with a 1,4-bis- (anthracenylethynyl)benzene (BAB) derivative as the LMWG (Fig. 8a-c).⁹⁰ The gel showed a thermoreversible and thixotropic behaviour with gel to sol phase change. Successful crystallisation from the molecular state to aggregated state showed that the BAB molecules were arranged in a *J*-aggregated fashion. The indication of π - π stacking was also found in the PXRD pattern with a peak at 24.2°. Methanolic solution of the BAB showed the vibronic band at 460 nm, and the peak position of the absorption was found to be redshifted in the xerogel state. This bathochromic shift also suggested the *J*-type aggregation of the BAB molecules in the gel state. This π -conjugated LMWG also showed luminescence properties where the peak maxima of the PL spectra were found at 479 and 505 nm for the methanolic solution of BAB. They have also incorporated an acceptor molecule inside the gel via non-covalent interaction to study the Forster Resonance Energy Transfer (FRET) phenomena. 4,4'-(perfluorocyclopent-1-ene-1,2-diyl)bis(5-methylthiophene-2-carbaldehyde)

(DTE derivative) was found to be a suitable candidate to understand this photochromic-FRET (pc-FRET) process (Fig. 8a). Interestingly, the energy acceptor molecule has two molecular forms (close and open) with two different absorption properties. These forms are interchangeable by the UV and Vis light irradiation. The absorption band of the close form had a proper overlap with the emission band of the BAB LMWG, which is an essential criterion for observing the pc-FRET process (Fig. 8b). The faster kinetics showed an ON-OFF energy transfer process. Therefore, the excited state energy transfer can only be feasible when the acceptor molecules are present in the close form. The decreasing intensity of the PL spectra of the DTE derivative incorporated BAB indicates the successful transfer of excited-state energy to the acceptor (Fig. 8c). The BAB was also able to regain its emission when it was irradiated with visible lights, and the DTE derivative transformed into its open form.

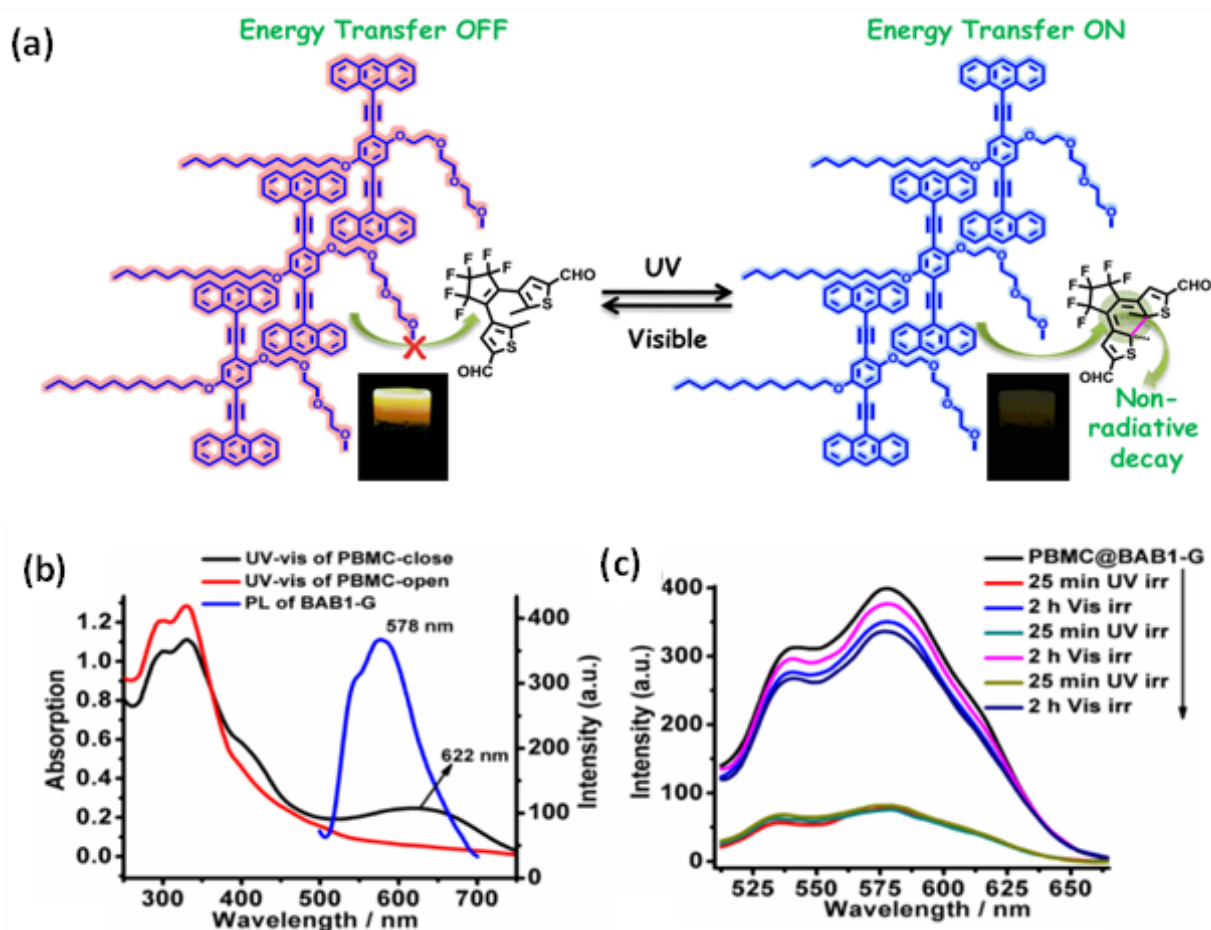


Figure 8. (a) Schematic of the pc-FRET process in gel materials. (b) UV-Vis spectra of the DTE-derivative and the emission spectra of the LMWG show the partial overlap of the spectra for the pc-FRET process. (c) The ON-OFF Energy transfer study in gel material by fluorescence spectroscopy. Figure reproduced from ref. 90 with permission.

CPG-based tuneable emission properties were further explored by the same group. They have designed a tripodal LMWG with one chromophore core unit and three metal binding sites for the coordination-driven gelation performance. 4,4',4'-[1,3,5-phenyl-tri(methoxy)]-tris-benzene core and 2,2':6',2''-terpyridyl termini were covalently connected for realising the gelation properties with different lanthanide ions.⁹¹ The LMWG was capable to form hydrogel with a nanosphere morphology. In contrast, a nanotubular morphology was found when it was assembled with lanthanide ions (Tb^{3+} and Eu^{3+}) in a solvent mixture of chloroform/THF. They have made a series of CPG with different emission maximums. The CPG made up of only Tb^{3+} showed a green emission, whereas the CPG made up of Eu^{3+} only showed red emission. A 1:2 combination of $\text{Tb}^{3+}:\text{Eu}^{3+}$ was capable of showing white light emission (Fig. 9a). They have also tried other combinations of the $\text{Tb}^{3+}:\text{Eu}^{3+}$ and CPGs are also found to emit cyan and pink light.

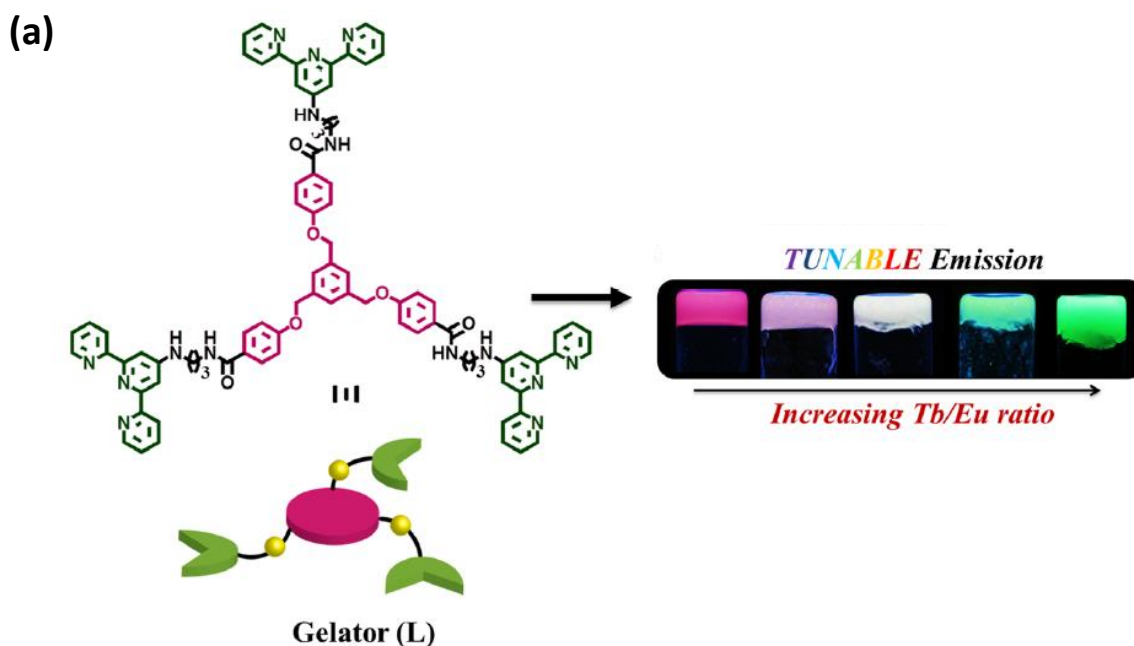


Figure 9. (a) Chemical structure of the LMWG. The coordination with the Eu^{3+} and Tb^{3+} in different stoichiometric ratios for tunable emission, including white light. Figure reproduced from ref. 91 with permission.

1.4.5 Gel materials as a catalyst for organic reactions: Metal catalysed organic reactions are well studied in material developments, and different metals were implemented to design the catalyst with some organic linker. Therefore, different metal-organic coordination complexes attracted enormous attention towards catalysis in different organic reactions.^{92,93} In this context, metal-organic coordination hybrid soft materials received immense interest in catalysis. Not only the nanostructure of the gel matrix can act as a catalyst, but also it gives

support to different metal-nanoparticle by helping in catalysis indirect way. Sarkar and co-workers showed the design and synthesis of a copper-based metallo-hydrogel with two organic ligands, which act as a catalyst in phenoxazinone synthesis (Fig. 10a-b).⁹⁴ They had found instantaneous gelation when the copper (II) solution was added to sodium succinate and hexamethylenetetramine solution. The xerogel showed a fibrous nanostructure and was responsive to different stimuli. The xerogel they have used for the catalytic oxidation of o-amino phenol to phenoxazinone, which is a crucial chromophore for the synthesis of actinomycin-D. Aerial oxidation in methanol was monitored by the UV-Vis spectrometric study. A characteristic peak of phenoxazinone at 430 nm was increasing with time, and conversion was also supported by mass analysis. A control study without the xerogel under the same condition shows no change in UV-Vis spectra, confirming the catalysis process by the redox-active copper metal-based xerogel.

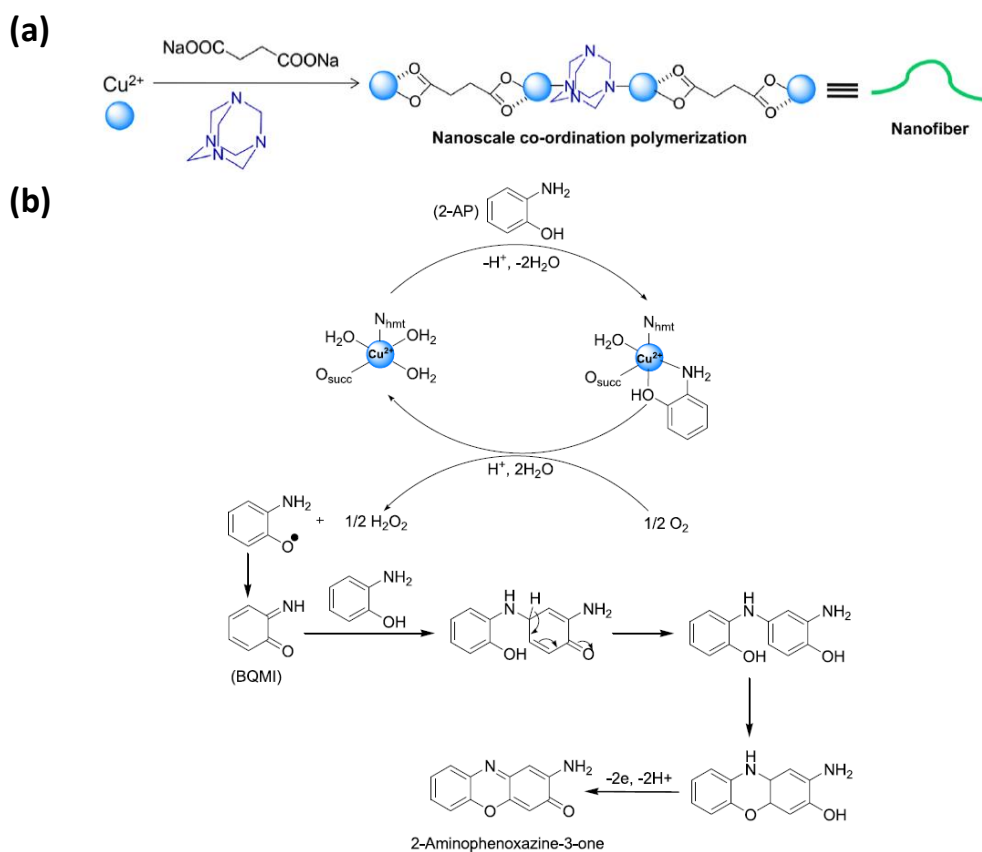


Figure 10: (a) Schematic of the formation of tricomponent gel nanofibers. (b) Catalytic cycle for the amino-phenoxazinone synthesis. Figure reproduced from ref. 94 with permission.

Yu *et al.* reported another copper-based metallogel and used it as a catalyst in click reaction (Fig. 11a-b).⁹⁵ A coordination polymeric gel was prepared by Cu^{2+} metal ions and a LMWG consisting terpyridine unit. The xerogel showed acts as the catalyst for the click

chemistry with the highest yield of 81.8% in water medium. This shows an environment-friendly and cheap nature of the catalysis process in water medium with a high reaction yield. They have performed a series of reactions with different substituted azide and alkyne. The catalyst shows a great performance for all in terms of yield. A recyclability test was also performed, and the xerogel showed stability up to the 4th cycle.

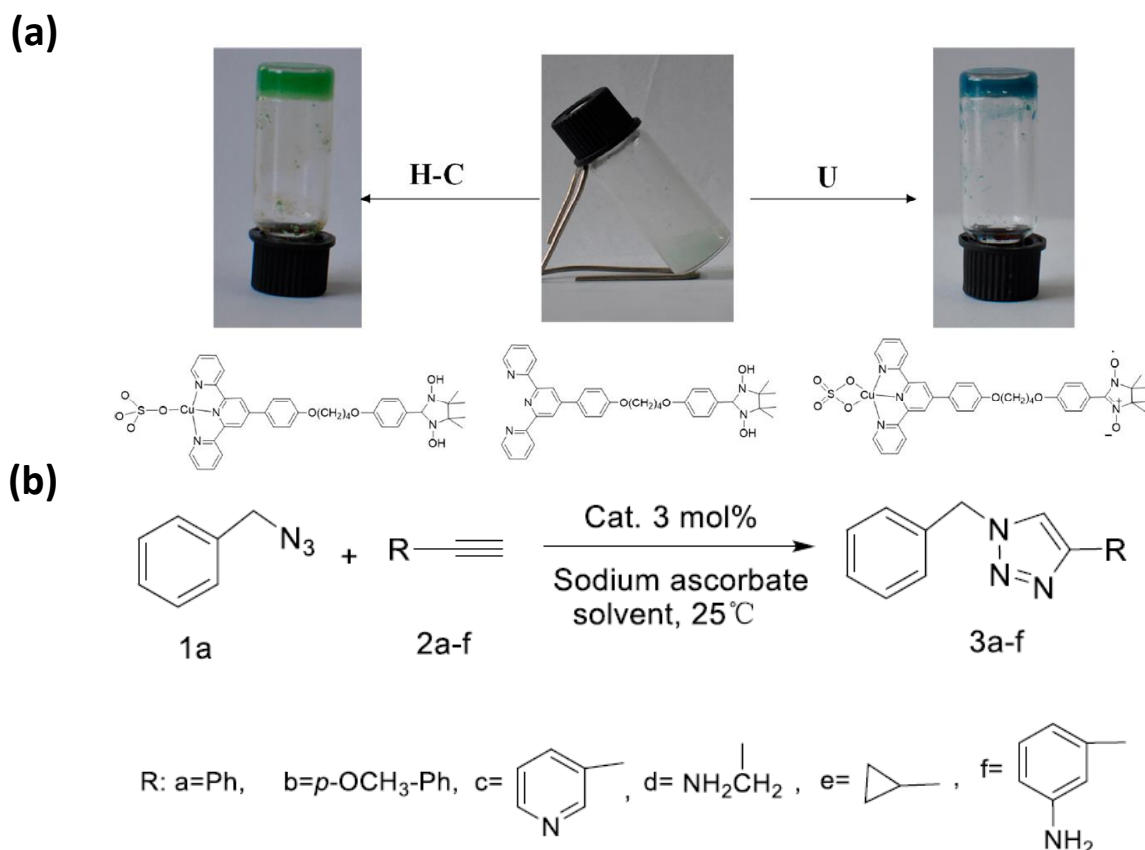


Figure 11. (a) Gelation process of the LMWG and Cu²⁺ with heating-cooling (H_C) method and by application of ultrasonic (U) power. (b) Xerogel acts as a catalyst for click reaction with a different substituted alkyne. Figure reproduced from ref. 95 with permission.

C-Yong Su and co-worker reported a metallogel with a pyridine-based tripodal ligand by incorporating Pd(COD)(NO₃)₂ in a CH₃OH-CHCl₃ mixed solvent system.⁹⁶ Involvement of hydrogen bonding, π - π interactions, coordination bonding in the gel showed different morphology with different Pd/Ligand ratio. The nanostructure changed from fibers to the sphere with increasing the ligand concentration. The catalytic potential was also found to be different for different concentration ratios. They have found that the 1:1 stoichiometric ratio of Pd and ligand with fibrous nanostructure shows the best catalytic activity towards the Suzuki-Miyaura reaction, and it also shows good recyclability up to the 5th cycle. Banerjee and co-workers reported a trihybrid gel system for enhanced catalytic performance.⁹⁷ A

covalently attached pyrene and tryptophan were used as the gelator, and graphene oxide (GO) was mixed during gelation, giving a high surface area and mechanical strength to the gel. Gold nanoparticles were also incorporated into the fibrous gel matrix to experience the catalytic reduction reaction of 4-amino phenol. Subsequent addition of GO and Au NPs improved the hydrogel's mechanical strength and enhanced the catalytic performance.

1.4.6 Photochemical and electrochemical CO₂ reduction with gel materials: A detailed study has been carried out in the last decades on the development of the confined environment for photoreactions. In this regard, different heterogeneous photocatalysts with 3D network structures are well explored for solar energy conversion. Supramolecular gel materials, which are typically self-assembly of the gelators through non-covalent interactions, can be a suitable candidate for photoconversion. Further, the metallo gels containing redox-active metal centers with a good conductive nature can be a potential candidate. The 3D entangled porous network structure also helps in the diffusion process of the CO₂, which readily comes into contact with the catalytic center. However, the efficiency and selectivity of the chemical process depend on the reaction medium, reaction type, solvent system, properties of the reactants, and properties of the gel matrix. Therefore, a judicious choice of the gelator, solvent system, and optimum reaction conditions are also important to realise the CO₂ reduction process with the soft material system. In spite of these advantages, there are only a few reports on CO₂ reduction with these soft processible materials. Maji and co-workers reported a tetrapodal LMWG with terpyridine units as the metal ions linker. The covalent connected tetrathiafulvalene with four terpyridine units based LMWG was combined with Zn²⁺ ions to get the coordination polymer gel (CPG) (Fig. 12a-c).⁵⁹ The charge transfer phenomena from the TTF unit to the Tpy units was investigated experimentally and computationally. This feasible electron transfer process was used in visible light-driven CO₂ reduction reactions. They obtained CO as a major product with the selectivity of 99% in an acetonitrile/water mixture medium with triethylamine as a sacrificial electron donor. Next, they have also deposited Pt nanoparticles on the gel matrix. Further, this soft material showed an enhanced catalytic activity toward methane production with 97% selectivity in a similar reaction environment.

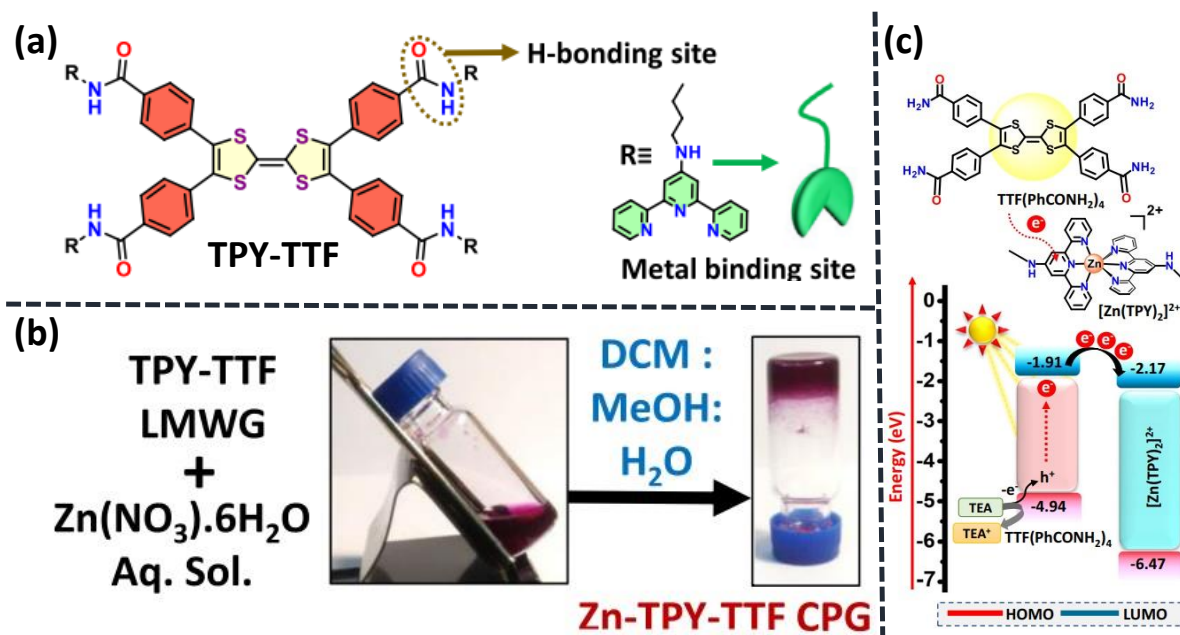


Figure 12. (a) Chemical structure of the LMWG. (b) Gelation study of the LMWG with Zn^{2+} in a mixture solvent. (c) electron transfer feasibility during the photocatalytic process. Figure reproduced from ref. 59 with permission.

Metal-organic polyhedras (MOPs) are also a promising candidate for the catalysis process due to the unsaturated coordination environments on the metal centers. Furukawa *et al.* recently reported designing and synthesizing a Rhodium-based metal-organic polyhedra (Rh-MOP) where the basic paddlewheel unit contains two coordination unsaturated Rh metal centers.⁹⁸ They have used two imidazole-containing linker molecules for connecting the Rh-MOPs, which end up with soft gel materials (Fig. 13a). One of the Rh centers helps bind with the imidazole linker's nitrogen, and the other remains unsaturated to show the catalytic activity. The photocatalytic CO_2 reduction reaction was studied in acetonitrile medium and triethanolamine (TEOA) as the proton and electron-donating agent. This highly stable catalyst showed the formation of formic acid as a sole product with a high productivity rate of $76 \text{ mmol} \cdot \text{g}^{-1} \cdot \text{h}^{-1}$. The electrochemical cyclic voltammetry study and density functional theory showed the redox-active character of the Rh cluster and the electron transfer feasibility during the CO_2 reduction process.

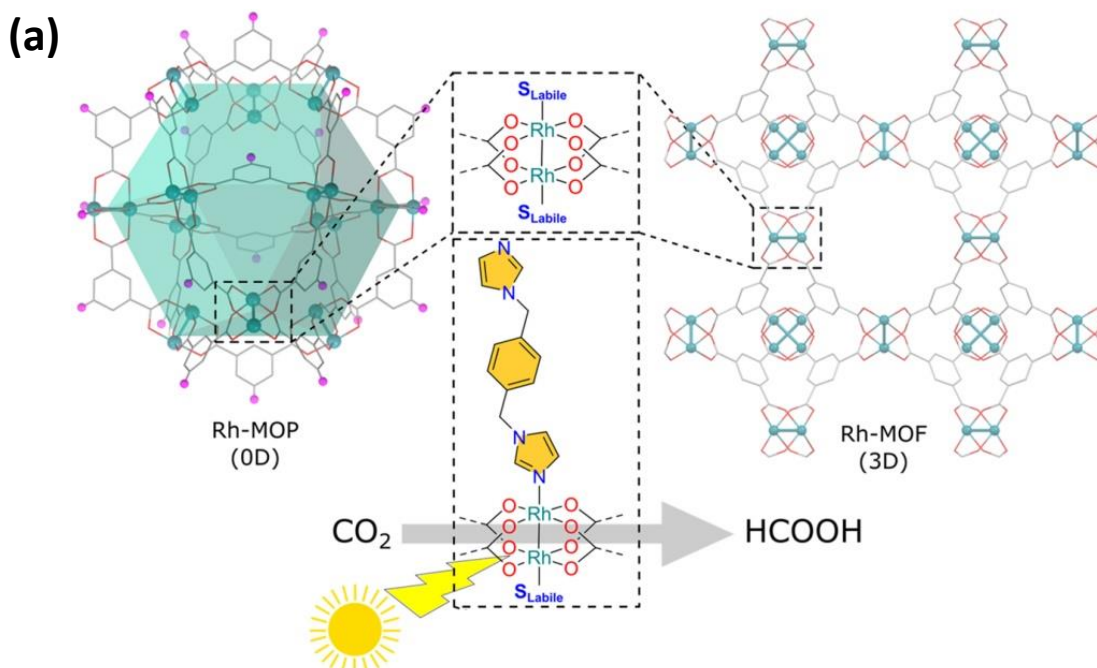


Figure 13. (a) Schematic of the MOP and the paddlewheel structure of the dirhodium unit for photocatalytic CO₂ reduction. Figure reproduced from ref. 98 with permission.

The suitable porous network for gas diffusion also makes the gel materials a promising candidate as an electrocatalyst for the CO₂ reduction process. Officer and co-workers showed the design and synthesis of graphene embedded iron-porphyrin gel materials.⁹⁹ They have performed the CO₂ reduction reaction in water medium. The primary difficulty in the electrochemical process is the competition between proton reduction and CO₂ reduction reactions. The 3D porous conductive nanostructure showed high faradaic efficiency of 96.2% for CO at a low overpotential of 280 mV. The robust nature of the hydrogel was also evaluated by a long-term efficiency experiment of CO production for up to 20 hours at the same potential.

1.5 Outlook:

The flexibility and the easy processibility of soft materials have attracted huge attention for applications in diverse fields over the past few decades. Self-assembly of LMWGs results in supramolecular gels that have been exploited for different application fields, including tissue engineering, optoelectronics, and bio-medicine. CPGs and other metallo gels are highly promising soft-hybrid materials because of the presence of metal ions, which endows them with unique redox, optical, electronic, and catalytic properties. To date, different synthetic strategies are implemented to design the LMWG and investigate the influence of metal coordination on the morphology and photophysical properties of the gels. The fundamental

study of this metastable kinetically trapped state to thermodynamically more stable arranged structure also has a great interest in the field of soft matter. Metal-organic cages are a class of materials that can also be used to construct these polymeric structures. However, this field of research is yet well explored. Assembling these metal-organic cages to a well-defined supramolecular arrangement by linking them with the binder is an important approach to investigate a phase transition process.

Visible light-driven and electrocatalytic CO₂ reduction is an emerging area of research in material sciences. This field is well explored with different semiconducting materials such as inorganic-oxide, metal-organic framework, organic polymers, and carbon-nitride-based materials. However, the application of gel materials in this field is not investigated yet. In this regard, we have designed different metallogels for CO₂ reduction applications. This thesis partially deals with photo and electrocatalytic CO₂ reduction reactions with CPG and MOCs based soft materials. These stimuli-responsive gel materials were also investigated for a spontaneous phase change. These multicomponent hybrid-soft materials also offer many potential opportunities; many of them are currently being explored.

1.6 References:

- 1 A. R. Hirst, B. Escuder, J. F. Miravet and D. K. Smith, *Angew. Chemie Int. Ed.*, 2008, **47**, 8002–8018.
- 2 B. O. Okesola and D. K. Smith, *Chem. Soc. Rev.*, 2016, **45**, 4226–4251.
- 3 S. S. Babu, V. K. Praveen and A. Ajayaghosh, *Chem. Rev.*, 2014, **114**, 1973–2129.
- 4 P. Sutar and T. K. Maji, *Dalt. Trans.*, 2020, **49**, 7658–7672.
- 5 M. M. Piepenbrock, G. O. Lloyd, N. Clarke and J. W. Steed, *Chem. Rev.*, 2010, **110**, 1960–2004.
- 6 N. M. Sangeetha and U. Maitra, *Chem. Soc. Rev.*, 2005, **34**, 821.
- 7 J. H. Jung, J. H. Lee, J. R. Silverman and G. John, *Chem. Soc. Rev.*, 2013, **42**, 924–936.
- 8 S. Panja and D. J. Adams, *Chem. Soc. Rev.*, 2021, **50**, 5165–5200.
- 9 H. Fan, J. Wang, Z. Tao, J. Huang, P. Rao, T. Kurokawa and J. P. Gong, *Nat. Commun.*, 2019, **10**, 5127.

- 10 L. Meazza, J. A. Foster, K. Fucke, P. Metrangolo, G. Resnati and J. W. Steed, *Nat. Chem.*, 2013, **5**, 42–47.
- 11 S. Yagai, H. Aonuma, Y. Kikkawa, S. Kubota, T. Karatsu, A. Kitamura, S. Mahesh and A. Ajayaghosh, *Chem. - A Eur. J.*, 2010, **16**, 8652–8661.
- 12 J. Li, R. Xing, S. Bai and X. Yan, *Soft Matter*, 2019, **15**, 1704–1715.
- 13 S. Datta and S. Bhattacharya, *Chem. Soc. Rev.*, 2015, **44**, 5596–5637.
- 14 S. C. P. Norris, J. Soto, A. M. Kasko and S. Li, *ACS Appl. Mater. Interfaces*, 2021, **13**, 5929–5944.
- 15 A. K. Denisin and B. L. Pruitt, *ACS Appl. Mater. Interfaces*, 2016, **8**, 21893–21902.
- 16 R. Staňo, P. Košován, A. Tagliabue and C. Holm, *Macromolecules*, 2021, **54**, 4769–4781.
- 17 S. J. Wezenberg, C. M. Croisetu, M. C. A. Stuart and B. L. Feringa, *Chem. Sci.*, 2016, **7**, 4341–4346.
- 18 I. Ramos Sasselli, P. J. Halling, R. V. Ulijn and T. Tuttle, *ACS Nano*, 2016, **10**, 2661–2668.
- 19 S. Satapathy, P. Prabakaran and E. Prasad, *Chem. - A Eur. J.*, 2018, **24**, 6217–6230.
- 20 X. Liu, J. Fei, A. Wang, W. Cui, P. Zhu and J. Li, *Angew. Chemie*, 2017, **129**, 2704–2707.
- 21 T. Guterman, M. Levin, S. Kolusheva, D. Levy, N. Noor, Y. Roichman and E. Gazit, *Angew. Chemie - Int. Ed.*, 2019, **58**, 15869–15875.
- 22 T. Yuan, Y. Xu, J. Fei, H. Xue, X. Li, C. Wang, G. Fytas and J. Li, *Angew. Chemie - Int. Ed.*, 2019, **58**, 11072–11077.
- 23 P. R. A. Chivers and D. K. Smith, *Nat. Rev. Mater.*, 2019, **4**, 463–478.
- 24 A. Y. Y. Tam and V. W. W. Yam, *Chem. Soc. Rev.*, 2013, **42**, 1540–1567.
- 25 P. Sutar and T. K. Maji, *Chem. Commun.*, 2016, **52**, 8055–8074.
- 26 E. Raphael, M. J. Derry, M. Hippler and S. P. Armes, *Chem. Sci.*, 2021, **12**, 12082–12091.

- 27 Y. You, J. Yang, Q. Zheng, N. Wu, Z. Lv and Z. Jiang, *Sci. Rep.*, 2020, **10**, 11727.
- 28 Q. Zhou, L. Dong, J. Wu, Y. Shi, X. Feng, X. Lu, J. Zhu and L. Mu, *ACS Appl. Polym. Mater.*, 2021, **3**, 5932–5941.
- 29 K. S. Oh, S. K. Han, Y. W. Choi, J. H. Lee, J. Y. Lee and S. H. Yuk, *Biomaterials*, 2004, **25**, 2393–2398.
- 30 E. Su, M. Yurtsever and O. Okay, *Macromolecules*, 2019, **52**, 3257–3267.
- 31 L. A. Estroff and A. D. Hamilton, *Chem. Rev.*, 2004, **104**, 1201–1217.
- 32 A. Y. Y. Tam, K. M. C. Wong, G. Wang and V. W. W. Yam, *Chem. Commun.*, 2007, 2028–2030.
- 33 F. J. Cedano-Serrano, U. Sidoli, A. Synytska, Y. Tran, D. Hourdet and C. Creton, *Macromolecules*, 2019, **52**, 3852–3862.
- 34 B. L. Abraham, E. S. Toriki, N. J. Tucker and B. L. Nilsson, *J. Mater. Chem. B*, 2020, **8**, 6366–6377.
- 35 Q. Wang, J. L. Mynar, M. Yoshida, E. Lee, M. Lee, K. Okuro, K. Kinbara and T. Aida, *Nature*, 2010, **463**, 339–343.
- 36 M. Criado-Gonzalez, D. Wagner, J. Rodon Fores, C. Blanck, M. Schmutz, A. Chaumont, M. Rabineau, J. B. Schlenoff, G. Fleith, J. Combet, P. Schaaf, L. Jierry and F. Boulmedais, *Chem. Mater.*, 2020, **32**, 1946–1956.
- 37 S. R. Van Tomme, M. J. Van Steenberghe, S. C. De Smedt, C. F. Van Nostrum and W. E. Hennink, *Biomaterials*, 2005, **26**, 2129–2135.
- 38 T. Xiao, L. Xu, L. Zhou, X. Q. Sun, C. Lin and L. Wang, *J. Mater. Chem. B*, 2019, **7**, 1526–1540.
- 39 S. M. Mantooh, B. G. Munoz-Robles and M. J. Webber, *Macromol. Biosci.*, 2019, **19**, 1–12.
- 40 H. W. Ooi, J. M. M. Kocken, F. L. C. Morgan, A. Malheiro, B. Zoetebier, M. Karperien, P. A. Wieringa, P. J. Dijkstra, L. Moroni and M. B. Baker, *Biomacromolecules*, 2020, **21**, 2208–2217.
- 41 R. D. Mukhopadhyay, G. Das and A. Ajayaghosh, *Nat. Commun.*, 2018, **9**, 1–9.

- 42 K. M. Park, J. A. Yang, H. Jung, J. Yeom, J. S. Park, K. H. Park, A. S. Hoffman, S. K. Hahn and K. Kim, *ACS Nano*, 2012, **6**, 2960–2968.
- 43 F. Zhao, J. Bae, X. Zhou, Y. Guo and G. Yu, *Adv. Mater.*, 2018, **30**, 1–16.
- 44 X. Sun, F. Yao and J. Li, *J. Mater. Chem. A*, 2020, **8**, 18605–18623.
- 45 A. Richter, G. Paschew, S. Klatt, J. Lienig, K. F. Arndt and H. J. P. Adler, *Sensors*, 2008, **8**, 561–581.
- 46 X. Yu, L. Chen, M. Zhang and T. Yi, *Chem. Soc. Rev.*, 2014, **43**, 5346–5371.
- 47 A. C. Pierre and G. M. Pajonk, *Chem. Rev.*, 2002, **102**, 4243–4265.
- 48 P. Terech and R. G. Weiss, *Chem. Rev.*, 1997, **97**, 3133–3159.
- 49 G. Zhu and J. S. Dordick, *Chem. Mater.*, 2006, **18**, 5988–5995.
- 50 M. Suzuki and K. Hanabusa, *Chem. Soc. Rev.*, 2010, **39**, 455–463.
- 51 A. Vintiloiu and J. C. Leroux, *J. Control. Release*, 2008, **125**, 179–192.
- 52 Y. Ni, X. Li, J. Hu, S. Huang and H. Yu, *Chem. Mater.*, 2019, **31**, 3388–3394.
- 53 S. Das, P. Chakraborty, A. Shit, S. Mondal and A. K. Nandi, *J. Mater. Chem. A*, 2016, **4**, 4194–4210.
- 54 S. Debnath, S. Kaushal, S. Mandal and U. Ojha, *Polym. Chem.*, 2020, **11**, 1471–1480.
- 55 P. Verma, F. A. Rahimi, D. Samanta, A. Kundu, J. Dasgupta and T. K. Maji, *Angew. Chemie - Int. Ed.*, , DOI:10.1002/anie.202116094.
- 56 P. Verma, A. Singh, F. A. Rahimi and T. K. Maji, *J. Mater. Chem. A*, 2021, **9**, 13608–13614.
- 57 S. M. M. Reddy, P. Dorishetty, G. Augustine, A. P. Deshpande, N. Ayyadurai and G. Shanmugam, *Langmuir*, 2017, **33**, 13504–13514.
- 58 A. Jain, K. Venkata Rao, C. Kulkarni, A. Geore and S. J. George, *Chem. Commun.*, 2012, **48**, 1467–1469.
- 59 P. Verma, A. Singh, F. A. Rahimi, P. Sarkar, S. Nath, S. K. Pati and T. K. Maji, *Nat. Commun.*, 2021, **12**, 1–14.
- 60 H. R. Khavasi and E. Jelokhani, *J. Mater. Chem. A*, 2019, **7**, 6638–6643.

- 61 H. B. Aiyappa, S. Saha, P. Wadge, R. Banerjee and S. Kurungot, *Chem. Sci.*, 2015, **6**, 603–607.
- 62 T. Feldner, M. Häring, S. Saha, J. Esquena, R. Banerjee and D. D. Díaz, *Chem. Mater.*, 2016, **28**, 3210–3217.
- 63 P. Chen, Q. Li, S. Grindy and N. Holten-Andersen, *J. Am. Chem. Soc.*, 2015, **137**, 11590–11593.
- 64 A. S. Weingarten, R. V. Kazantsev, L. C. Palmer, M. McClendon, A. R. Koltonow, A. P. S. Samuel, D. J. Kiebal, M. R. Wasielewski and S. I. Stupp, *Nat. Chem.*, 2014, **6**, 964–970.
- 65 G. De Paoli, Z. Džolic, F. Rizzo, L. De Cola, F. Vögtle, W. M. Müller, G. Richardt and M. Žinic, *Adv. Funct. Mater.*, 2007, **17**, 821–828.
- 66 A. Vashist, A. Kaushik, A. Ghosal, J. Bala, R. Nikkhah-Moshaie, W. A. Wani, P. Manickam and M. Nair, *Gels*, 2018, **4**, 1–15.
- 67 T. Shay, O. D. Velev and M. D. Dickey, *Soft Matter*, 2018, **14**, 3296–3303.
- 68 Z. Wei, J. H. Yang, J. Zhou, F. Xu, M. Zrínyi, P. H. Dussault, Y. Osada and Y. M. Chen, *Chem. Soc. Rev.*, 2014, **43**, 8114–8131.
- 69 T. Wang, X. Yu, Y. Li, J. Ren and X. Zhen, *ACS Appl. Mater. Interfaces*, 2017, **9**, 13666–13675.
- 70 M. Nakahata, Y. Takashima, H. Yamaguchi and A. Harada, *Nat. Commun.*, 2011, **2**, 511.
- 71 Q. Wang, J. L. Mynar, M. Yoshida, E. Lee, M. Lee, K. Okuro, K. Kinbara and T. Aida, *Nature*, 2010, **463**, 339–343.
- 72 M. Martínez-Calvo, O. Kotova, M. E. Möbius, A. P. Bell, T. McCabe, J. J. Boland and T. Gunnlaugsson, *J. Am. Chem. Soc.*, 2015, **137**, 1983–1992.
- 73 S. Basak, J. Nanda and A. Banerjee, *Chem. Commun.*, 2014, **50**, 2356–2359.
- 74 C. D. Jones and J. W. Steed, *Chem. Soc. Rev.*, 2016, **45**, 6546–6596.
- 75 S. J. Lee, S. S. Lee, M. S. Lah, J. M. Hong and J. H. Jung, *Chem. Commun.*, 2006, 4539–4541.

- 76 S. Sarkar, S. Dutta, S. Chakrabarti, P. Bairi and T. Pal, *ACS Appl. Mater. Interfaces*, 2014, **6**, 6308–6316.
- 77 S. Barman, J. A. Garg, O. Blacque, K. Venkatesan and H. Berke, *Chem. Commun.*, 2012, **48**, 11127–11129.
- 78 H. Lee, S. H. Jung, W. S. Han, J. H. Moon, S. Kang, J. Y. Lee, J. H. Jung and S. Shinkai, *Chem. - A Eur. J.*, 2011, **17**, 2823–2827.
- 79 A. Dutta and U. Maitra, *ACS Sensors*, 2022, **7**, 513–522.
- 80 J. Majumder, J. Deb, M. R. Das, S. S. Jana and P. Dastidar, *Chem. Commun.*, 2014, **50**, 1671–1674.
- 81 D. Zhao, S. Tan, D. Yuan, W. Lu, Y. H. Rezenom, H. Jiang, L. Q. Wang and H. C. Zhou, *Adv. Mater.*, 2011, **23**, 90–93.
- 82 A. Mallick, B. Garai, D. D. Díaz and R. Banerjee, *Angew. Chemie - Int. Ed.*, 2013, **52**, 13755–13759.
- 83 J. Naskar, G. Palui and A. Banerjee, *J. Phys. Chem. B*, 2009, **113**, 11787–11792.
- 84 K. Basu, A. Baral, S. Basak, A. Dehsorkhi, J. Nanda, D. Bhunia, S. Ghosh, V. Castelletto, I. W. Hamley and A. Banerjee, *Chem. Commun.*, 2016, **52**, 5045–5048.
- 85 P. Chakraborty and P. Dastidar, *Chem. Commun.*, 2019, **55**, 7683–7686.
- 86 G. O. Lloyd and J. W. Steed, *Nat. Chem.*, 2009, **1**, 437–442.
- 87 O. Kotova, R. Daly, C. M. G. Dos Santos, M. Boese, P. E. Kruger, J. J. Boland and T. Gunnlaugsson, *Angew. Chemie - Int. Ed.*, 2012, **51**, 7208–7212.
- 88 V. M. Suresh, A. De and T. K. Maji, *Chem. Commun.*, 2015, **51**, 14678–14681.
- 89 W. L. Leong, A. Y. Y. Tam, S. K. Batabyal, L. W. Koh, S. Kasapis, V. W. W. Yam and J. J. Vittal, *Chem. Commun.*, 2008, 3628–3630.
- 90 D. Samanta, A. Singh, P. Verma, S. Bhattacharyya, S. Roy and T. K. Maji, *J. Org. Chem.*, 2019, **84**, 10946–10952.
- 91 P. Sutar and T. K. Maji, *Inorg. Chem.*, 2017, **56**, 9417–9425.
- 92 M. Häring, R. Pérez-Ruiz, A. J. Von Wangelin and D. D. Díaz, *Chem. Commun.*,

- 2015, **51**, 16848–16851.
- 93 N. J. Oldenhuis, K. P. Qin, S. Wang, H. Z. Ye, E. A. Alt, A. P. Willard, T. Van Voorhis, S. L. Craig and J. A. Johnson, *Angew. Chemie - Int. Ed.*, 2020, **59**, 2784–2792.
- 94 S. Sarkar, P. K. Maji, Y. Negishi, S. Dutta, T. N. Das, R. Pan and S. Sarkar, *ACS Appl. Nano Mater.*, 2021, **4**, 1455–1466.
- 95 T. Zhao, S. Chen, K. Kang, J. Ren and X. Yu, *Langmuir*, 2022, **38**, 1398–1405.
- 96 Y. R. Liu, L. He, J. Zhang, X. Wang and C. Y. Su, *Chem. Mater.*, 2009, **21**, 557–563.
- 97 J. Nanda, A. Biswas, B. Adhikari and A. Banerjee, *Angew. Chemie - Int. Ed.*, 2013, **52**, 5041–5045.
- 98 A. C. Ghosh, A. Legrand, R. Rajapaksha, G. A. Craig, C. Sassoie, G. Balázs, D. Farrusseng, S. Furukawa, J. Canivet and F. M. Wisser, *J. Am. Chem. Soc.*, 2022, **144**, 3626–3636.
- 99 J. Choi, J. Kim, P. Wagner, S. Gambhir, R. Jalili, S. Byun, S. Sayyar, Y. M. Lee, D. R. MacFarlane, G. G. Wallace and D. L. Officer, *Energy Environ. Sci.*, 2019, **12**, 747–755.

Chapter 2

***Iron(II) based coordination polymer gel
towards visible-light driven multi-electron
photocatalytic CO₂ reduction***

Abstract

The design of a low molecular weight gelator (LMWG) and the study of their self-assembly towards a supramolecular soft material is emerging as a photocatalytic medium for solar fuel production. Besides this, solar energy to much-needed renewable sources such as CO₂ reduction to valuable products can be achieved by designing an efficient catalytic medium. This chapter discusses the design and synthesis of a covalently connected naphthalene diimide core with two terpyridine units (Tpy-NDI) based LMWG and corresponding self-assembled gel matrix utilisation for photocatalytic reaction. Self-assembly of these LMWG in dimethyl sulfoxide (DMSO) showed nanofibrous morphology with a *J*-type aggregation. The coordination polymer gel (CPG) was prepared by the Fe²⁺ metal ions coordination with the Tpy-NDI LMWG in a water-DMSO solvent mixture. Coordination of the Fe²⁺ metal ions with Tpy units showed a broad metal to ligand charge transfer band in the visible region, and the Fe-Tpy-NDI CPG matrix has consisted of a fibrous nanostructure. Upon visible light irradiation, Fe-Tpy-NDI CPG exhibited the CO₂ reduction reaction to CH₄ in water with triethylamine (TEA) and 1,4-dihydronicotinamide (BNAH) as the sacrificial electron donors. The highest productivity rate of CH₄ was found to be 2.75 mmol g⁻¹ h⁻¹ with 85% selectivity. Further, the *in-situ* DRIFT spectroscopy suggests possible reaction intermediates during CO₂ reduction to CH₄.

2.1 Introduction:

A hike in CO₂ emissions with the development of a carbon-based society is making a significant impact on climate change.^{1,2} However, now it is also impossible to avoid fossil fuel utilisation for daily energy requirements due to the lower availability and higher cost of different renewable energy. Therefore, the two elementary ways to reduce the amount of CO₂ are capturing and conversion to different value-added products.³ In the last few years, CO₂ reduction reaction (CO₂RR) has been gaining significant interest in the field of material research and development. However, the major difficulty one has to face in this reduction process is the very high stability and inert nature of CO₂, owing to the strong dissociation energy of the C=O bond (750 kJ mol⁻¹) with a complicated reduction pathway.⁴ In this 21st century, solar energy is also growing as an attractive renewable energy source, and its highly diffuse nature can fulfill all future energy demands. The sunlight that reaches the earth's surface consists of 50% of visible light and 45% of the infrared components with an insignificant amount of UV part. Considering all the possible strategies for the catalytic reduction process, the photocatalytic approach is found to be the most efficient in terms of energy efficiency and much viable due to the ambient reaction conditions.⁵ Artificial photosynthesis is one of the emerging approaches for converting CO₂ to different chemical feedstock with a promising green pathway.⁶ Natural photosynthesis involves a sequence of enzymes for light-harvesting, charge separation, and migration process in a very precise mechanism. Mimicking this phenomenon with the help of catalytic material not only can reduce the CO₂ load but also lower down the fossil fuel dependency.

There are several C1 based fuels one can get upon CO₂RR, such as CO, HCOOH, CH₃OH, and CH₄, where CH₃OH and CH₄ can be used directly in the fuel cell, increasing their demand.⁷ However, the thermodynamic and kinetic parameters are different in each case as the product formation involves a different number of electron transfer with an intricate mechanism. The thermodynamic feasibility for the production of CH₄ is much easier than that of CO, as indicated by the standard reduction potential value ($E^0_{\text{CH}_4} = -0.24 \text{ V vs. NHE}$ and $E^0_{\text{CO}} = -0.53 \text{ V vs. NHE at pH 7}$).⁸ Nevertheless, the formation of CH₄ is much more difficult than that of CO because of the eight-electron transfer process in the case of CH₄, which makes the kinetics substantially more sluggish in nature and makes it incredibly challenging. Only a handful of metal alloys, metal chalcogenides, and metal oxides are available, which can act as semiconductors for photocatalytic CO₂ reduction. Still, those generally suffer from lower productivity and selectivity issues. Hence, designing a photocatalyst with a light-

harvesting unit and catalytic center is much needed to overcome the obstacle of selectivity and productivity.⁹

To this end, low molecular weight gelator (LMWG) based inorganic-organic hybrid soft nanomaterial with all compulsory components can act as a potential agent for this photo-redox event.¹⁰ Gelator molecules can form a coordination-driven self-assembled structure with the help of suitable metal ions. This porous solid network is well known for various application fields like biomedical, optoelectronics, and food industries.¹¹ Coordination polymer gel (CPG) comprises different non-covalent interactions such as π - π stacking, electrostatic interaction, hydrogen bonding, and hydrophobic interaction, which helps to form the colloidal fibrous network and can hold a copious amount of solvent.¹² Such kind of hierarchical porous fibrous structure helps in the gas diffusion process and allows the metal centers to act as an active site. The integrated structure consists of a light collecting unit with semiconducting nature that can generate photoexcited charges.¹³ The feasible migration of these charges to the catalytic point leads to a potential candidate for CO₂RR. Here, naphthalene diimide can serve the purpose with a long π conjugated arrangement, and it is also well known for constructing a self-assembled structure through face-to-face aggregation.¹⁴ Naphthalene diimide has absorption at the junction of the UV, and Visible component and a terpyridine unit with a redox-active metal center. This redox-active terpyridine metal complex has a large absorption in the visible range due to the MLCT phenomena, which helps to separate the electron and hole, indicating semiconducting behaviour.

This chapter demonstrates a new class of processible soft material, Coordination Polymer Gel (CPG), made up of LMWG by covalently connected naphthalene diimide (NDI) and terpyridine units with the help of metal ion coordination. Here, iron (II) is chosen as the node for the polymeric chain because of its redox-active behavior, low cost, and high earth abundance.^{8,15} The nanoscopic flexible fibrous structure of the CPG matrix acts as an integrated component for photosensitisation. Photocatalytic CO₂ reduction performance was examined in water medium with sacrificial agents triethylamine (TEA) and 1-Benzyl-1,4-dihydronicotinamide (BNAH).¹⁶ CH₄ was found to be the primary product with a selectivity of >85% with a maximum rate of 2.75 mmol g⁻¹ h⁻¹. Here, NDI acts as the catalytic center and the [Fe(Tpy)₂]²⁺ as the light-harvesting unit according to the molecular orbital positions. Furthermore, the eight-electron transfer pathway for the conversion of CO₂ to CH₄ is established by *in-situ* DRIFT spectroscopic study.

2.2 Experimental section:

2.2.1 General: 1,4,5,8-Naphthalenetetracarboxylic dianhydride, 4-Aminobenzoic acid, 4-Chloro-2,2':6,2'-terpyridine, 1,2-Diaminopropane, were purchased from Sigma-Aldrich chemical Co. Ltd. All solvents and triethylamine (NEt₃) were obtained from Spectrochem Pvt. Ltd. (Mumbai, India).

¹H-NMR spectra were carried out on a Bruker AVANCE-400 spectrometer (at 400 MHz), and the chemical shifts recorded as ppm with all spectral calibration against TMS. UV-Vis spectra were recorded on a Perkin-Elmer lambda 900 spectrometer. MALDI has performed on a Bruker daltonics Autoflex Speed MALDI TOF System (GT0263G201) spectrometer. The ATR-IR experiment measurements were carried out using an FT-IR spectrophotometer (BRUKER, VORTEX 70B) in the region 4000–400 cm⁻¹. Powder X-ray diffraction (PXRD) patterns were collected in gel state coated on a glass plate and taken by a Rigaku Smartlab SE instrument using Cu K α radiation. Atomic force microscopy (AFM) measurements were carried out with Asylum MFD-3D Origin to analyse the morphologies of the sample surface. Samples were prepared by making a dispersion of the xerogels in THF and coated on a silicon wafer by the drop-casting method. The Field Emission Scanning Electron Microscopic (FE-SEM) images were recorded on a Zeiss Gemini SEM 500. Samples were prepared by the drop-casting method on a small piece of Si wafer and loaded in the machine without gold sputtering. Transmission Electron Microscopy (TEM) studies were done on JEOL JEM -3010 with an accelerating voltage of 300 kV. For this analysis, the xerogels were dispersed in THF and drop-casted on a carbon copper grid. The rheological study was done in Anton Paar Rheometer MCR 92 using plane plate geometry on a Peltier glass plate. The diameter of the plate was 60mm, and the measuring unit had a diameter of 25mm. The gel samples were placed on the plate and stress sweep experiment at a constant frequency at 25 °C, and frequency sweep measurements at constant stress in the linear viscoelastic range were carried out to get the storage or elastic modulus (G') and loss or viscous modulus (G'') values of the gel materials.

2.2.2 Electrochemical characterisations:

Mott-Schottky measurement: The energy band structure of Fe-Tpy-NDI-CPG was evaluated by the Mott Schottky (MS) analysis (at 1000, 2000, 3000, 4000 Hz, from -2.0 V to +2.0 V) using a glassy carbon electrode (area=0.07065 cm²) as a working electrode (WE) in N₂-purged aqueous solution of 0.2 M Na₂SO₄ at pH=7, Pt spring was used as a counter

electrode (CE) and Ag/AgCl as the reference electrode (RE). The ink for this measurement was prepared by making a dispersion of the corresponding sample (2 mg) in a mixture solvent of isopropyl alcohol (800 μL), mili Q water (180 μL), and Nafion (20 μL). After sonication of half an hour, 10 μL of the ink was coated on the working electrode and allowed for drying in ambient conditions for 3 hours. The obtained graph was fitted with equation 1.¹⁷

$$1/C^2 = (2/ \varepsilon \varepsilon_0 A^2 e N_D) (V-V_{fb} - k_B T/e) \dots\dots\dots \text{Eq.1}$$

Where, C and A are the interfacial capacitance and area, respectively. ε is the dielectric constant of the semiconductor, and ε₀ is the permittivity of free space. k_B Boltzmann constant, T the absolute temperature, and e is the electronic charge. N_D the number of donors, V the applied voltage. Hence the plot of 1/C² vs. V will give a straight line, and the intercept should yield the conduction band edge (V_{fb}).

Photocurrent measurement: A similar electrochemical setup (with three electrodes) was employed for the photocurrent measurement, but here an ITO plate connected with a copper wire was used as the working electrode. The photocurrent study was performed for Tpy-NDI-OG and Fe-Tpy-NDI-CPG upon consecutive light "ON-OFF" cycles for 30 s over 5 cycles at +0.5 V.

Impedance measurement: A three-electrode cell configuration with a glassy carbon electrode as the working electrode (WE), platinum as a counter electrode (CE), and Ag/AgCl as a reference electrode (RE) was used for Electrochemical impedance spectroscopy (EIS) performance and 0.2 M Na₂SO₄ was used as the electrolyte for this measurement. The ink was prepared by making a dispersion of the xerogel in a mixture solvent of isopropyl alcohol (800 μL), mili Q water (180 μL), and Nafion (20 μL). Sonicated for 30 mins and 10 μL of the ink was coated on the working electrode and allowed it for drying in ambient conditions for 3 hours. The Nyquist plot was recorded from 0.1 Hz to 100 kHz with light irradiation and without light.

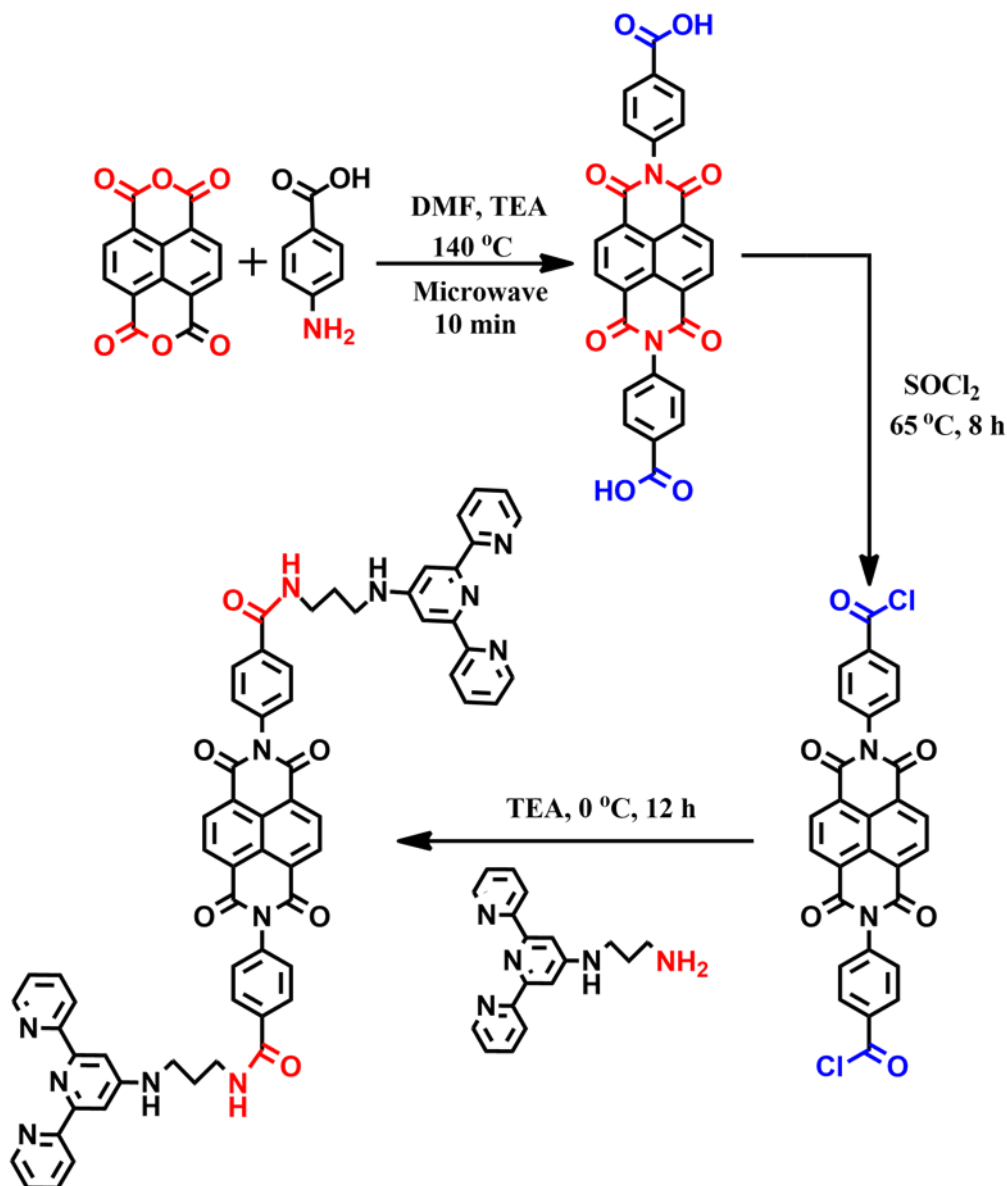
2.2.3 Artificial visible light-driven CO₂ reduction: Photocatalytic CO₂ reduction was carried out under visible light from a solar light simulator. 300 W Xenon Lamp (Newport) after using a visible bandpass filter (400-750 nm), also fitted with a 12 cm path length of water filter for removal of IR irradiation. Photocatalysis was performed by taking 1 mg of catalyst and dispersed in the solvent (4 mL water), and taken in an airtight capped seal glass cell along with a magnetic stirrer. BNAH (2 mg) and triethylamine (1mL) were also taken into the catalytic chamber as the sacrificial electron donor, and to get a uniform dispersion,

the sample was sonicated for 30 mins. Before going to the catalysis process, the dispersed sample was bubbled by 99.99% pure CO₂ for half an hour to ensure the full replacement of the dissolved gas and to get a saturation by the CO₂ only. Next, the vessel was sealed properly by Teflon tape and kept under irradiation for the photocatalytic redox process. The generated gas which is collected on the upper portion of the chamber, was analyzed with an interval of 2 hours. Hamilton syringe was used for the collection of the gaseous product and injected into the Gas Chromatography-Mass Spectrometry (GCMS) QP2020. Gaseous products were examined qualitatively and quantitatively by using the mass detector. The calibration was done by a standard gas mixture of H₂, CO, and CH₄ of different concentrations in ppm-level. For the isotopic labeling experiment, ¹³CO₂ gas was purged for 5 minutes in a controlled manner to the photocatalytic reaction mixture.

2.2.4 *In situ* diffuse reflectance FT-IR measurements: The *in situ* FT-IR measurements were carried out by FT-IR spectrophotometer (BRUKER, Pat. US, 034, 944) within a photoreactor. The 5 mg of catalyst was evenly spread over a glass disc of 1 cm diameter, that was placed at the center of the photoreactor for monitoring photocatalytic CO₂ reduction reaction. Next, the air inside the cell was removed using vacuum and then 99.99 % CO₂ gas along with water vapour was passed for 15 minutes into the photoreactor. At last, the visible light irradiation was done by 150 W white LED light (> 400 nm). *In situ* FT-IR signal was collected through MCT detector along as function of irradiation time.

2.3 Synthesis:

Synthesis of the low molecular weight gelator (Tpy-NDI): The synthesis of Tpy-NDI is described in the following three steps.



Scheme 1: Synthetic scheme for the Low Molecular Weight Gelator (Tpy-NDI)

Step 1. Synthesis of the 4-aminobenzoic acid derivative of naphthalenediimide (NDI-Ph-COOH): Microwave-assisted synthesis technique was followed by modifying the reported procedure.¹⁸ 1,4,5,8-naphthalenetetracarboxylic dianhydride (500 mg, 1.86 mmol), 4-aminobenzoic acid (1.02 g, 7.4 mmol) was taken into a 30 mL microwave vial, and suspended in 15 mL dimethylformamide (DMF) by 15 mins of sonication. After the addition of 0.55 mL of triethylamine into the reaction mixture, the vial was closed by the lid and

sealed with Teflon tape. Placed that vial in the microwave reactor and heated at 140°C at 900 rpm for 10 minutes. After cooling down, the yellow color product was collected by filtration under suction, washed with water and methanol, followed by drying under vacuum. The yield was calculated 87%. $^1\text{H-NMR}$ (400 MHz, $\text{DMSO-}d_6$) δ : 13.15 (broad, 2H, COOH), 8.72 (m, 4H, ArH), 8.12(t, 4H, ArH), 7.61(t, 4H, ArH).

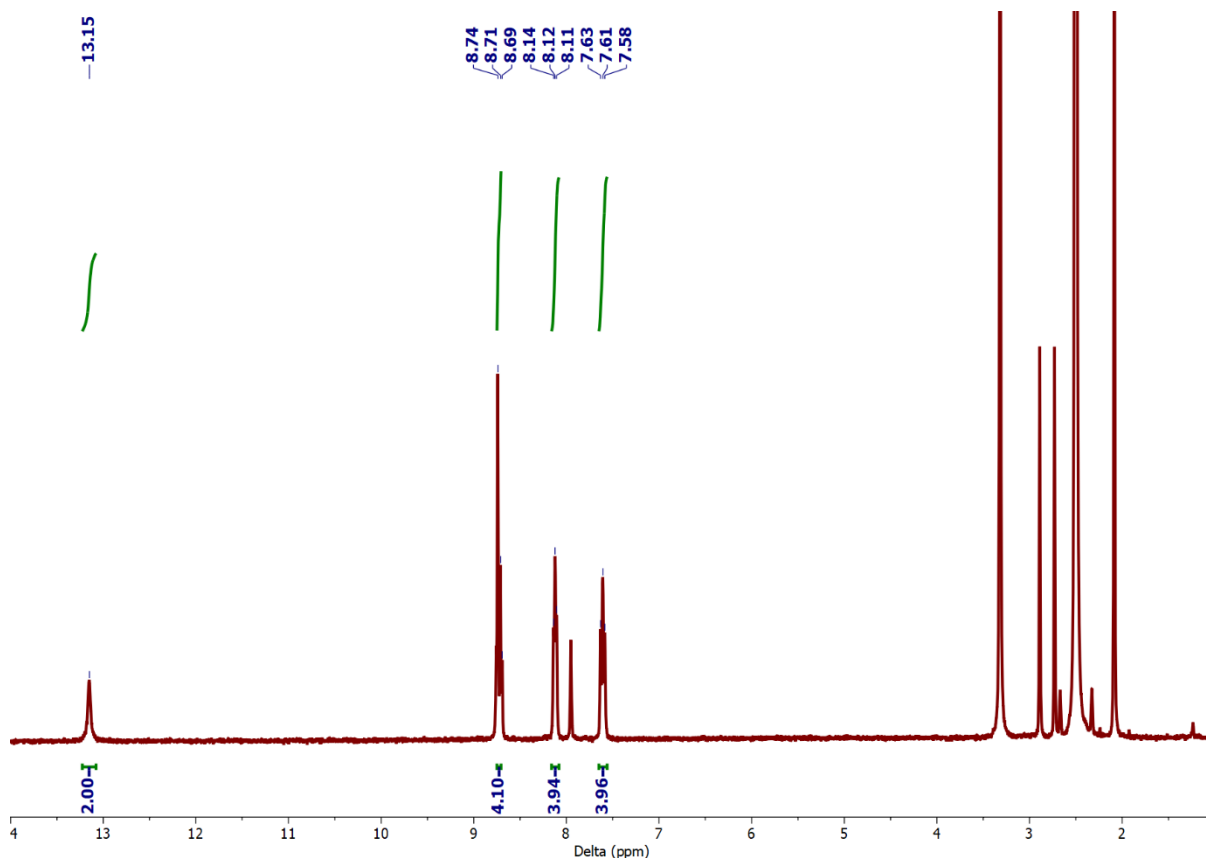


Figure 1. $^1\text{H-NMR}$ of NDI-Ph-COOH in $\text{DMSO-}d_6$

Step 2. Synthesis of 4-aminobenzoic acid chloride derivative of naphthalenediimide (NDI-Ph-COCl): Synthesis of the acid chloride has been done with a known procedure. NDI-Ph-COOH (435 mg, 1.17 mmol) was suspended in dry THF, and SOCl_2 (3.14 mL, 46.8 mmol) was added into it under inert conditions. The reaction mixture was refluxed for 8 hours at 65°C. Next, the reaction mixture was distilled at 120°C to remove excess SOCl_2 and yielded a yellowish-white solid precipitate of acid chloride. That solid was repeatedly washed with dry THF by centrifugation. The yield was calculated to be 93%. $^1\text{H-NMR}$ (400 MHz, $\text{DMSO-}d_6$) δ : 8.74 (s, 4H, ArH), 8.15 (t, 4H, ArH), 7.63 (q, 4H, ArH).

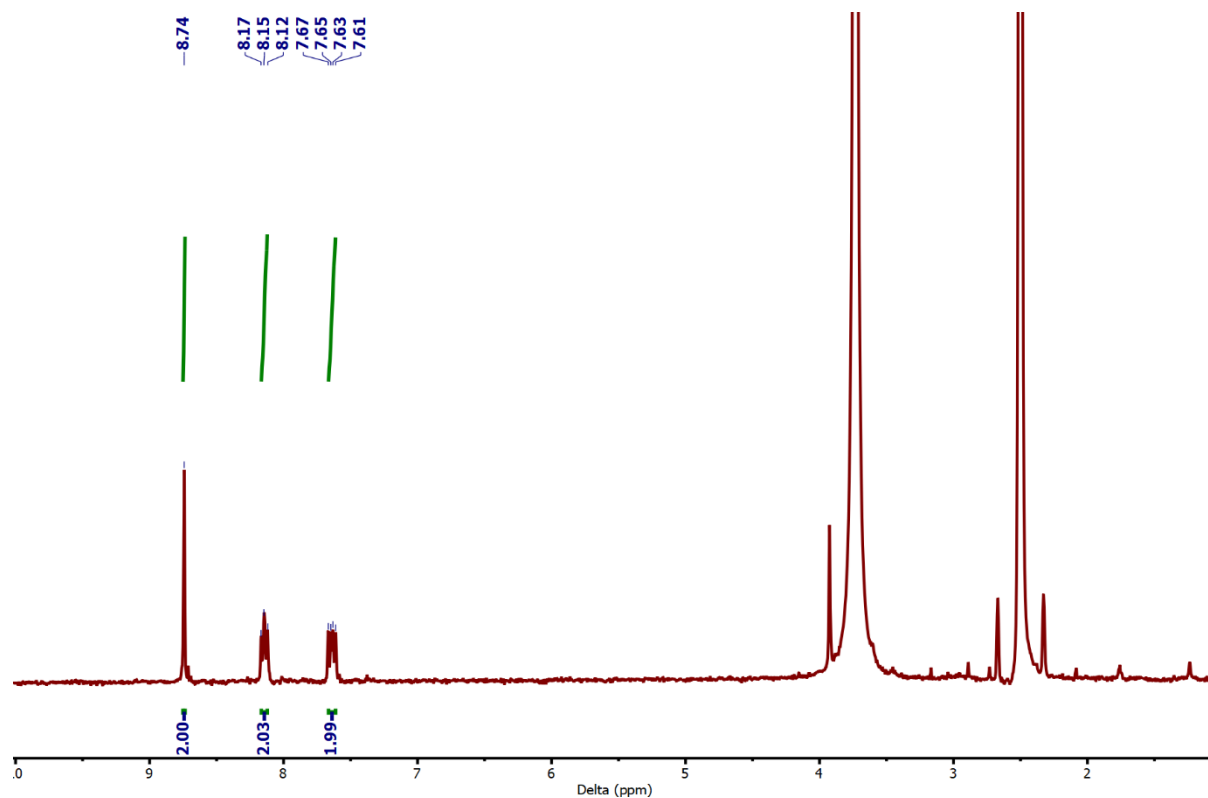
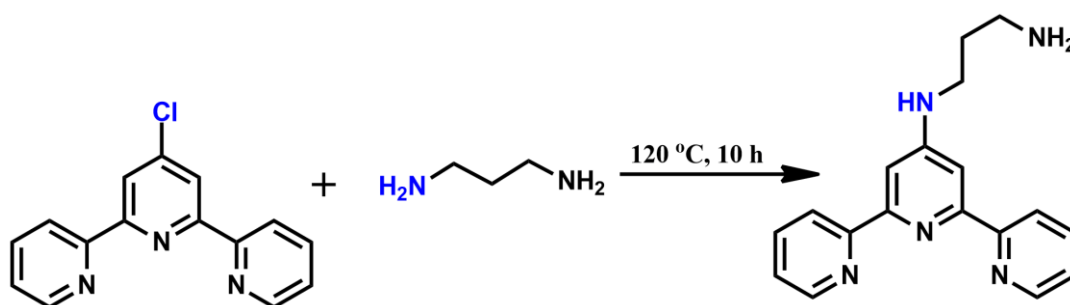


Figure 2. $^1\text{H-NMR}$ of NDI-Ph-COCl in $\text{DMSO-}d_6$

Synthesis of 2,2';6',2''-terpyridin-4'-yl-propane-1,3-diamine (Tpy-NH₂): Synthesis has been done according to the reported procedure.¹⁹ 4'-chloro-2,2';6',2''-terpyridine (300 mg, 1.12 mmol) was suspended in 1,3-diaminopropane (2.16 ml) by sonication for 10 minutes. The reaction mixture was then refluxed at 120°C for overnight. After cooling down to room temperature, distilled water (25 mL) was added, and it yielded a white precipitate. This white precipitate was filtered and further washed with distilled water. The solid was dissolved in dichloromethane and extracted twice with distilled water. The organic layers were combined and dried over Na_2SO_4 , and the solvent was removed under reduced pressure to yield a white solid product. Yield: 82%. $^1\text{H-NMR}$ (400 MHz, CDCl_3) δ : 8.65 (m, 2H, ArH), 8.58 (m, 2H, ArH), 7.82 (m, 2H, ArH), 7.65 (m, 2H, ArH), 7.29 (m, 2H, ArH), 5.08 (b, 1H, NH), 3.45 (b, 2H, NH₂), 2.89 (t, 2H, CH₂), 1.82 (m, 2H, CH₂), 1.25 (m, 2H, CH₂).



Scheme 2: Synthetic scheme for the Terpyridine amine (Tpy-NH₂)

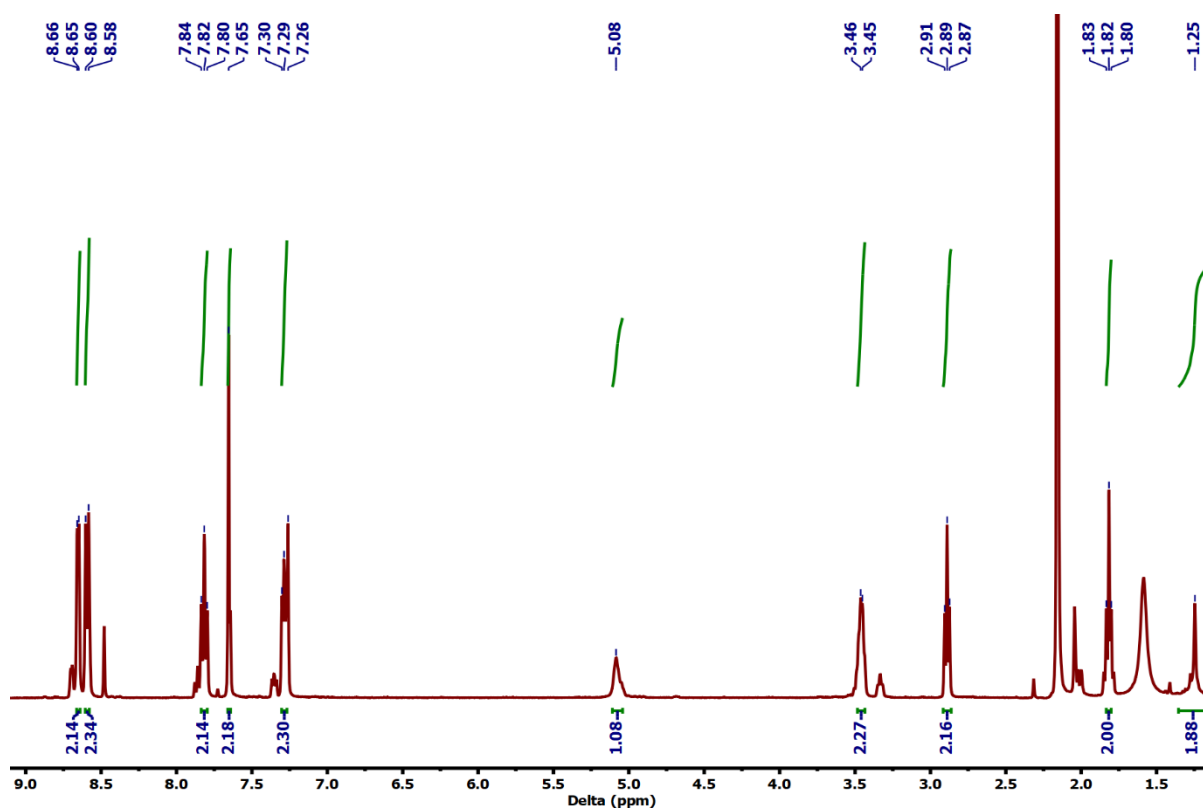


Figure 3. ¹H-NMR of Tpy-NH₂ in CDCl₃

Step 3. Synthesis of Tpy- NDI Low molecular weight gelator (LMWG):

Synthesis has been carried out by following a reported procedure.¹⁰ NDI-Ph-COCl (404 mg, 1.34 mmol) was taken in a Schlenk RB and suspended by adding dry THF (30 mL) under an inert atmosphere. Tpy-NH₂ (1.2 gm, 4.02 mmol) was dissolved in dry THF (20 mL) and triethylamine (0.5ml), also maintaining the inert condition. The second solution was added into the first solution dropwise over a time period of half an hour at 0°C in an inert condition. The reaction mixture was stirred at 0°C for 12 hours. A brown colour precipitate formed, which was collected by centrifugation and washed with THF, methanol, and acetone several

times. The yield was calculated to be 56%. ^1H NMR (600 MHz, $\text{DMSO-}d_6$): $\delta = 8.74$ (s, 4H), 8.56 (d, 4H), 8.15 (t, 2H), 8.03 (d, 4H), 7.95 (t, 4H), 7.57 (d, 4H), 7.44 (m, 4H), 6.95 (b, 2H), 3.47 (m, 4H), 3.36 (m, 4H), 1.95 (m, 4H). MALDI-TOF (m/z) calculated for $\text{C}_{64}\text{H}_{48}\text{N}_{12}\text{O}_6$: 1081.143; found: $[\text{M}+\text{H}]^+$ 1082.546

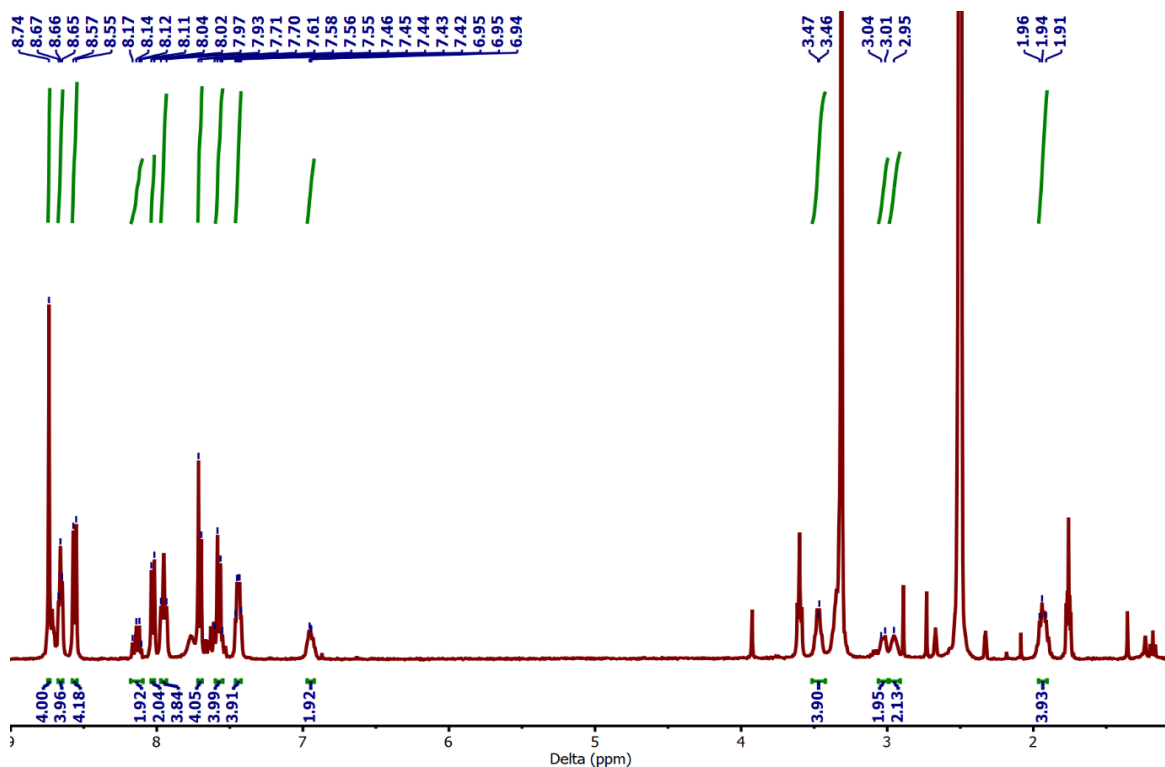


Figure 4. ^1H -NMR of Tpy-NDI in $\text{DMSO-}d_6$

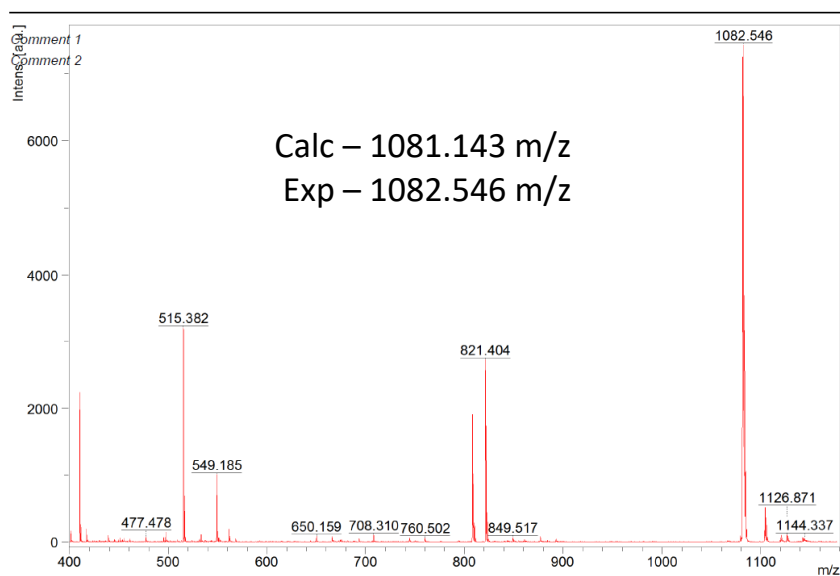


Figure 5. MALDI data of Tpy-NDI

2.4 Results and discussion:

The low molecular weight gelator (LMWG) 4,4'-(1,3,6,8-tetraoxo-1,3,6,8-tetrahydrobenzo[lmn][3,8]phenanthroline-2,7-diyl)bis(N-(3-([2,2':6',2''-terpyridin]-4'-ylamino)propyl)benzamide) was synthesised by the amide coupling method shown earlier and characterised by different spectroscopic techniques. Next, the gelation ability was examined with this LMWG under different conditions.

2.4.1 Preparation of the organogel:

Gelation was tried with different single and bi-component solvent systems using the conventional heating and cooling method. But we found that our low molecular weight gelator can only form the gel in dimethyl sulfoxide (DMSO). 5 mg of the low molecular weight gelator (**Tpy- NDI**) was taken into a glass vial, and 200 μ L of DMSO was added, followed by sonication for 15 minutes and heating at 120 $^{\circ}$ C. The thick viscous solution was kept overnight without any disturbance, and it transformed into the gel. The formation of gel was confirmed by the inverse vial test and rheology experiment.

Solvent system	Temperature	Solubility	Gel
DMSO	120 $^{\circ}$ C	Yes	Yes
DMSO + water (7:3)	120 $^{\circ}$ C	No	No
DMF	120 $^{\circ}$ C	Sparingly	No
DMF + water (7:3)	120 $^{\circ}$ C	No	No
THF	80 $^{\circ}$ C	No	No
Chloroform	80 $^{\circ}$ C	No	No
THF + Chloroform (1:1)	80 $^{\circ}$ C	No	No
Acetonitrile	80 $^{\circ}$ C	No	No

Table 1. Solvation and gelation trial of Tpy-NDI

2.4.2 Characterisation of the LMWG and organogel:

As synthesised LMWG (Tpy-NDI) was characterized by ^1H NMR, MALDI, and ATR-IR techniques. UV-vis spectrum of 10^{-6} M Tpy-NDI in DMSO indicates the presence of both NDI and terpyridine units. The characteristic vibronic band was observed in the UV-vis spectrum at 335, 352, and 372 nm for the NDI core (Fig 6a). The absorption band at 372 and 352 nm can be attributed to the π - π^* transition of the carbonyl unit and naphthalene core.²⁰

The terminal terpyridine component also shows the absorption band at 275 nm due to the π - π^* transition. Photoluminescence spectrum of 10^{-6} M Tpy-NDI in DMSO upon excitation at the lowest energy absorption band of NDI core (at $\lambda_{\text{ex}} = 350$ nm) shows two sharp peaks at 410 and 435 nm and a shoulder peak at 465 nm (Fig 6b).²¹

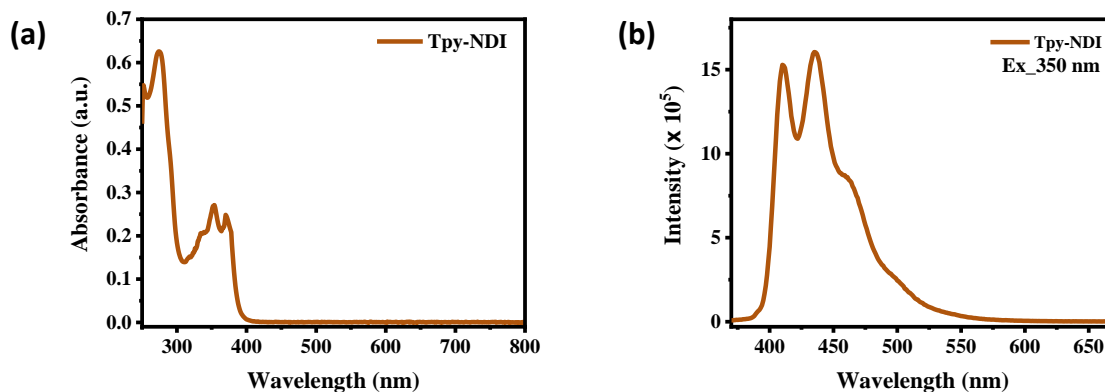


Figure 6. (a) Absorption spectrum of Tpy-NDI (LMWG) in solution state. (b) Emission spectrum of Tpy-NDI (LMWG) in solution state.

These kinds of π electron-rich planar units, along with amide connectivity, can form self-assembly with short-range ordering driven by π - π stacking and H-bonding interactions. 25 mg/mL gelator solution in DMSO was heated at 120 °C followed by cooling at room temperature, showing a light brown opaque gel formation. Gelation was confirmed by the inversion test method and rheology experiment. The rheology study showed a linear viscoelastic region under lower shear strain when the amplitude sweep method was carried out under a wide range of shear strain, starting from 0.01% to 100% with a constant angular frequency of 1.5 Hz (Fig 7a). It also exhibited the cross-over point at 100% strain.

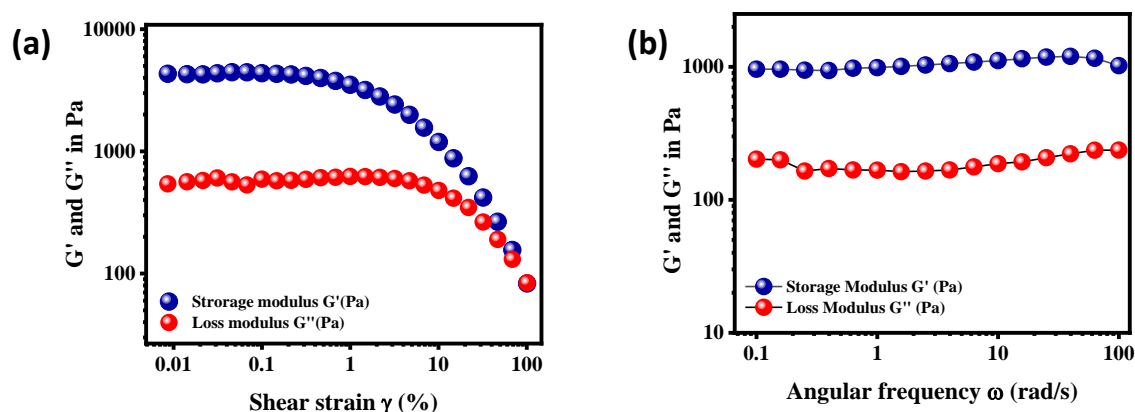
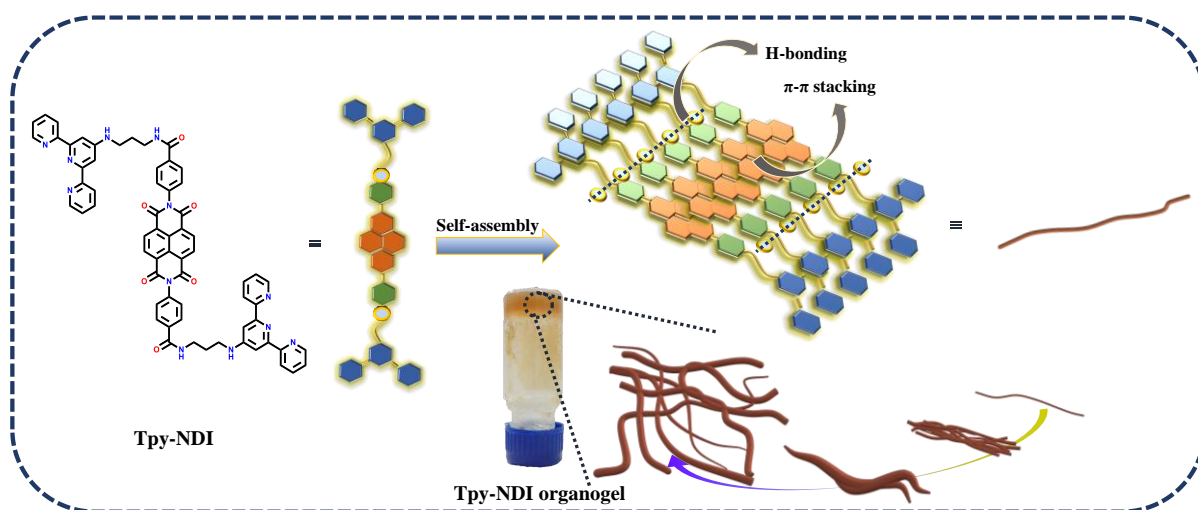


Figure 7. (a) Strain sweep measurement of Tpy-NDI-OG with $\gamma\% = 0.01$ -100% (b) Frequency sweep test for Tpy-NDI-OG at a constant strain of 0.1%.

Notably, the storage modulus (G') value was higher as compared to the loss modulus (G'') under the lower shear strain region, indicating the viscoelastic nature of the gel. Amplitude sweep experiment has also been performed by varying the angular frequency (0.1 rad/s to 100 rad/s) under a constant shear strain of 0.1% (Fig 7b). Linear and parallel lines of storage modulus (G') and loss modulus (G'') suggested that there was no dependency of these modulus values on this angular frequency region.²²



Scheme 3: Typical schematic illustration of the self-aggregation process of the Tpy-NDI LMWG with the help of H-bonding and π - π stacking interaction towards the fibrillar structure.

To investigate the aggregation nature of the Tpy-NDI gelator, UV-Vis spectra were collected with the addition of water into a DMSO solution of 10^{-5} (M) Tpy-NDI. The absorption band for 10^{-5} (M) Tpy-NDI DMSO solution was found in the range of 330 to 400 nm. These three peak maxima were attributed to the π - π^* transition of the NDI core, which is polarized along the molecular long axis. These transitions were sensitive towards the aggregation of the NDI units through the π - π interaction.²³ There are two types of self-assembled structures that can be possible for these types of π -electron rich core moieties, namely *H*-type aggregation and *J*-type aggregation. Where the face-to-face arrangement is known as *H*-type and a staircase-like arrangement is known as the *J*-type. With the addition of the water to the DMSO solution of Tpy-NDI shows a shifting of the absorbance band from 382 nm to 384 nm with a decrease in the optical density (Fig 8a). This gradual bathochromic shift of the absorption maxima (λ_{\max}) with the increasing amount of water indicates the formation of self-assembly of the NDI chromophore in the *J*-type aggregation fashion (Scheme 3).²⁴ Other Photophysical properties of the Tpy-NDI in gel state were performed by making a thin film on a quartz plate. Self-assembly of the low molecular weight gelator was studied in gel state with UV-vis spectroscopy. A significant red shift in

absorption peak maxima was observed for both the NDI core and Terpyridine terminal. In the case of 350 nm absorbance peak for NDI core, a 20 nm peak maxima shift has been observed along with a 17 nm shift in 380 nm absorbance peak (Fig 8b). This bathochromic shift in absorbance of the π electron-rich rings indicates the *J*-type aggregation of the LMWG in the gel state. The photoluminescence emission peak of the Tpy-NDI gel was found to be much broader than its molecular state in solution (Fig 8c). The optical bandgap of the Tpy-NDI xerogel was determined by diffused reflectance spectroscopic (DRS) technique. A plot of Kubelka-Munk function with energy indicates the bandgap of 3.02 eV (Fig 8d). Attenuated transmission reflectance (ATR)-IR spectra of Tpy-NDI-OG shows the characteristic peak for N-H stretching at 3381 cm^{-1} , C-H stretching at 3016 cm^{-1} , and C=O stretching at 1653 cm^{-1} (Fig 9a).

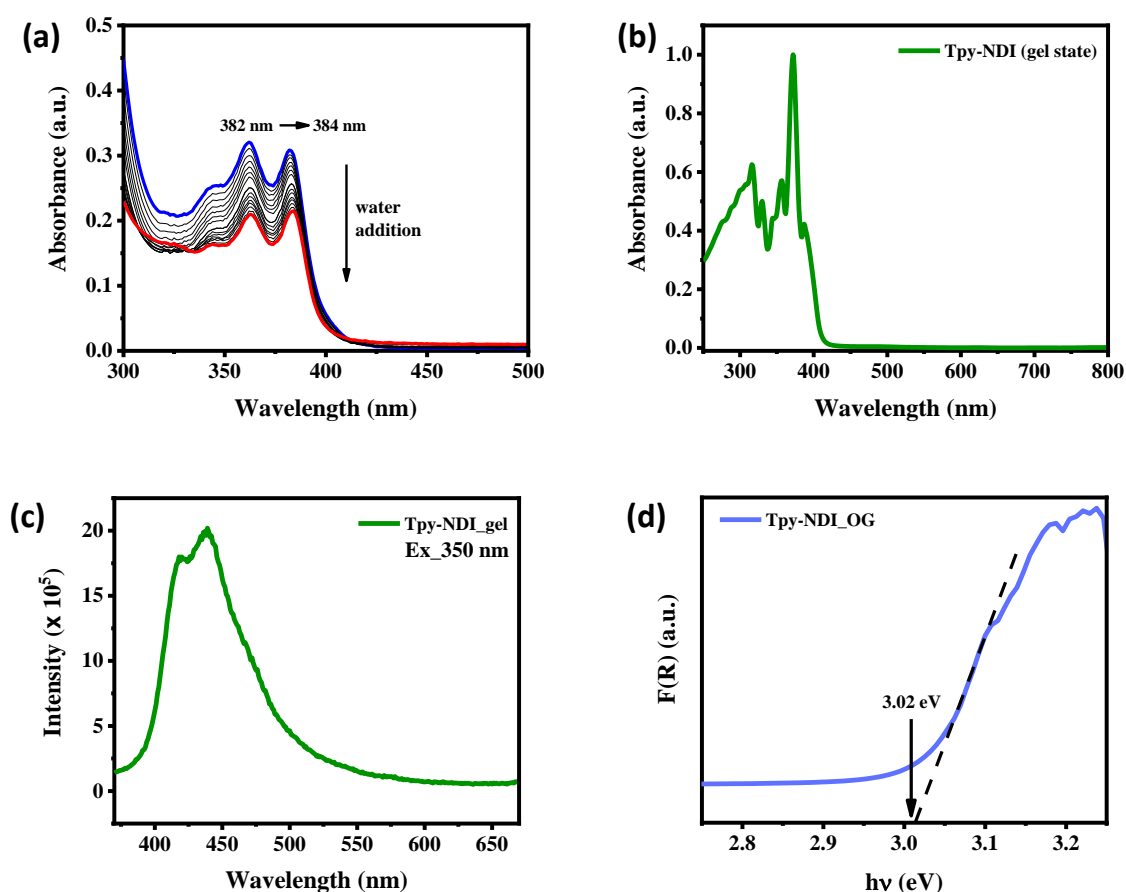


Figure 8. (a) Change in absorption spectrum of Tpy-NDI in DMSO with the addition of water. (b) Absorption spectrum of Tpy-NDI-OG. (c) Emission spectrum of Tpy-NDI-OG (d) Kubelka-Munk plot for Tpy-NDI-OG obtained by Diffused Reflectance Spectra (DRS).

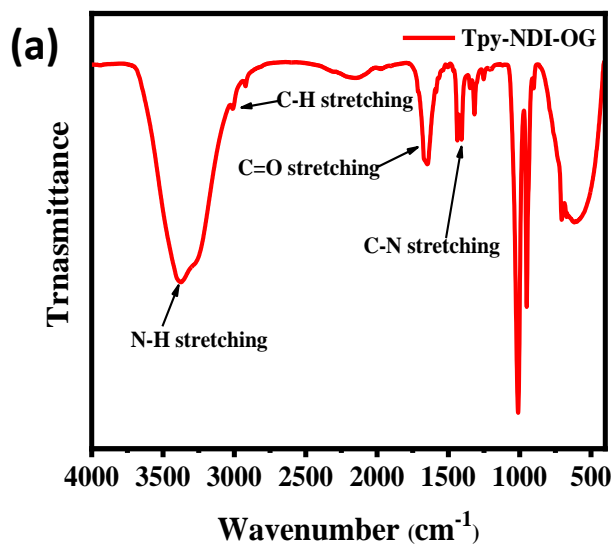


Figure 9. (a) ATR-IR spectrum of Tpy-NDI-OG.

Morphological investigation of the self-assembled structure of Tpy-NDI was done by atomic force microscopy (AFM) and transmission electron microscopy (TEM). Tpy-NDI OG shows an interconnected fibrillar assembly with a height of ~ 15 nm (Fig 10a).

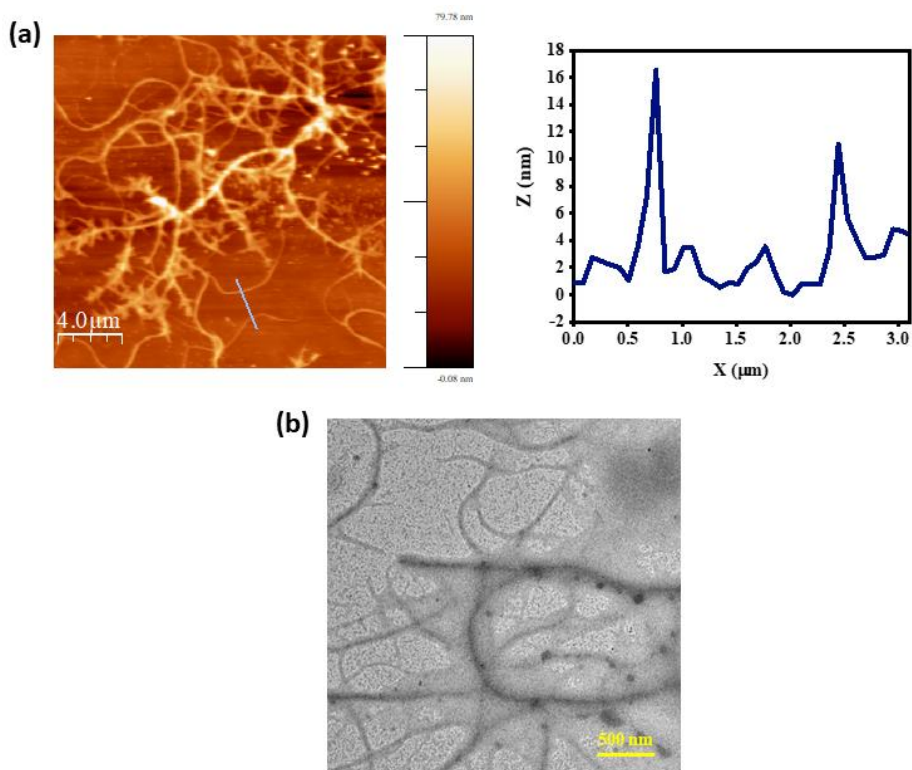


Figure 10 (a) AFM image of Tpy-NDI-OG with the height profile diagram. (b) TEM image of Tpy-NDI-OG.

2.4.3 Characterisation of the LMWG and Coordination polymer gel:

As the LMWG, Tpy-NDI has metal coordination sites at the two ends. Further, we move to get a self-assembled coordination polymer gel with appropriate metal ions. An earth-abundant, low-cost Fe (II) metal center was found to be suitable for gelation. Fe (II) terpyridine complexes were well studied to show the MLCT transition from metal d orbital to π^* of terpyridine, and this has an intense visible light absorption. Recently, the terpyridine complexes with first-row transition metal ions are getting more recognition towards different redox processes driven by photo and electrochemical methods because of their easy availability with more than one stable oxidation states. Before performing the gelation study, the stoichiometric complexation ratio was determined by the UV-Vis titration curve.²⁵ Titration was carried out by taking 2×10^{-5} M Tpy-NDI solution in DMSO as the aliquot and 1×10^{-3} M aqueous solution of FeSO₄ as titrant (Fig 11a).

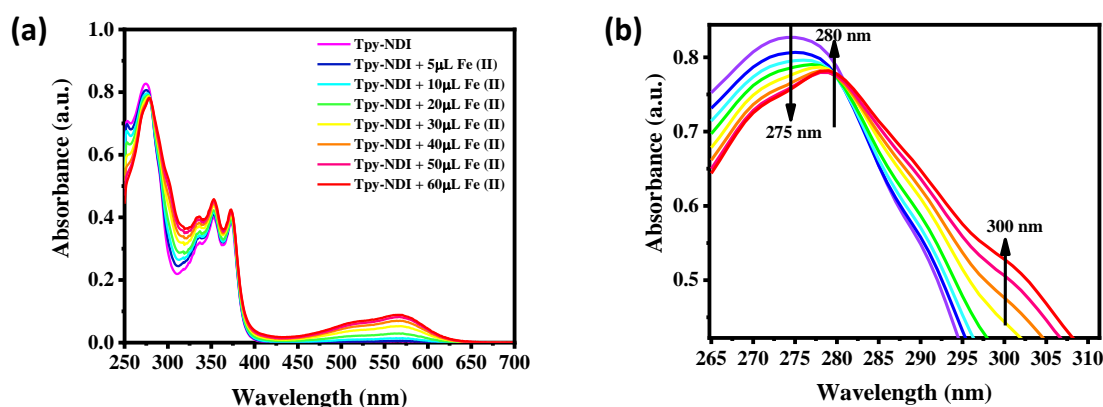


Figure 11. (a,b) Titration of Tpy-NDI LMWG (2×10^{-5} M in DMSO) with Fe(II) (1×10^{-3} M in water).

A gradual peak shifting was observed with the addition of Fe (II) metal ions solution into the Tpy-NDI solution (Fig 11b). The peak at 275 nm for the terpyridine unit slowly shifted to 280 nm, and a new peak appeared at 300 nm upon metal binding to the terpyridine terminal.¹⁰ This steady shift in absorbance and isosbestic point with increasing the concentration of Fe (II) indicates the complexation of the metal center with the ligand. It was also observed that the peak intensity for the NDI core was getting increased. This phenomenon suggests that the NDI core was coming out from the π - π interaction to the molecular phase. Upon metal ions binding to the terminal part of the LMWG, it went towards a linear state. Jobs plot and isosbestic point revealed the binding ratio of Fe (II) metal ion and Tpy-NDI is 1:1 where the absorbance gets saturated (Fig 12a). The association constant (K_a) of metal and binding sites of Tpy-NDI was determined from the Benesi-Hildebrand plot and calculated to be 1.3×10^4 (Fig 12b).

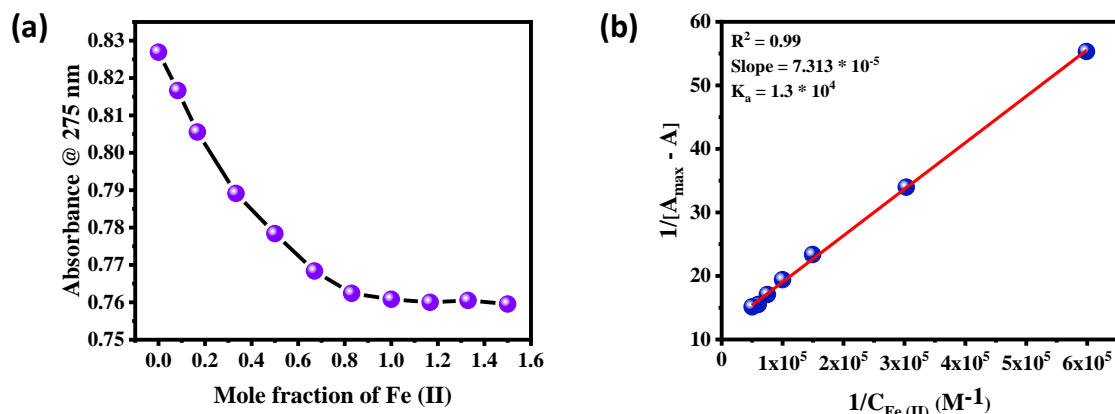


Figure 12. (a) Change in absorbance at 275 nm with the addition of Fe(II) ions. (b) Benesi-Hildebrand plot for the binding affinity of Tpy-NDI LMWG with Fe (II) ion.

After confirming the binding of the metal ions to the organo-linker, CPG formation was tried with different solvent ratios. The coordination polymer gel was formed only with the molar ratio of 1:1 of metal ions and LMWG in a 1:1 solvent mixture of water and DMSO (Scheme 4). 100 μL of 2×10^{-3} M aqueous solution of FeSO_4 was added to a solution of Tpy-NDI (5 mg in 100 μL of DMSO) and heated at 120 $^\circ\text{C}$ for 10 min, followed by cooling at room temperature, leads to the formation of deep purple color gel. Metal ions and LMWG ratio were kept to be 1:1 as determined from the titration plot. Similar to organogel, CPG formation was confirmed by the rheology experiment (Fig 13a). The amplitude sweep measurement with varying shear strain at a constant angular frequency of 1.5 Hz indicates a linear viscoelastic nature of the gel. In a lower strain percentage, i.e., in the viscoelastic region, storage modulus (G') had a higher value than that of loss modulus (G'') with a cross-over point at 30% of shear strain.

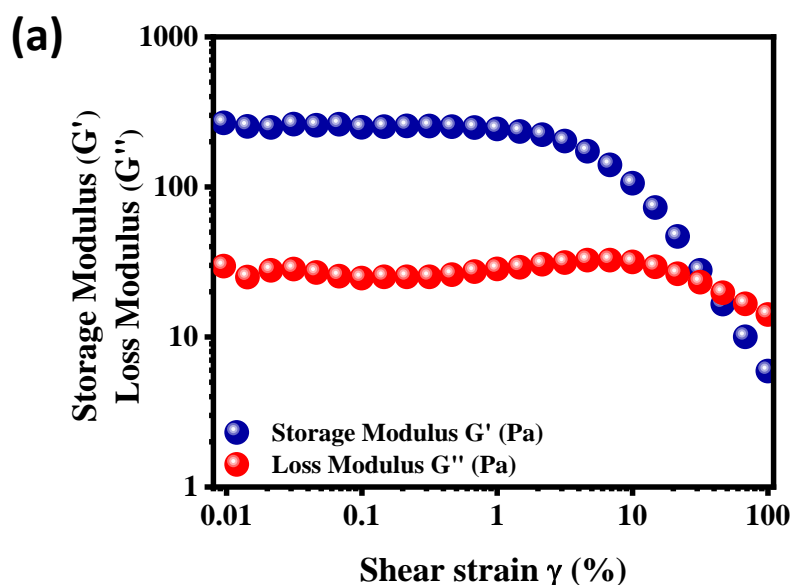
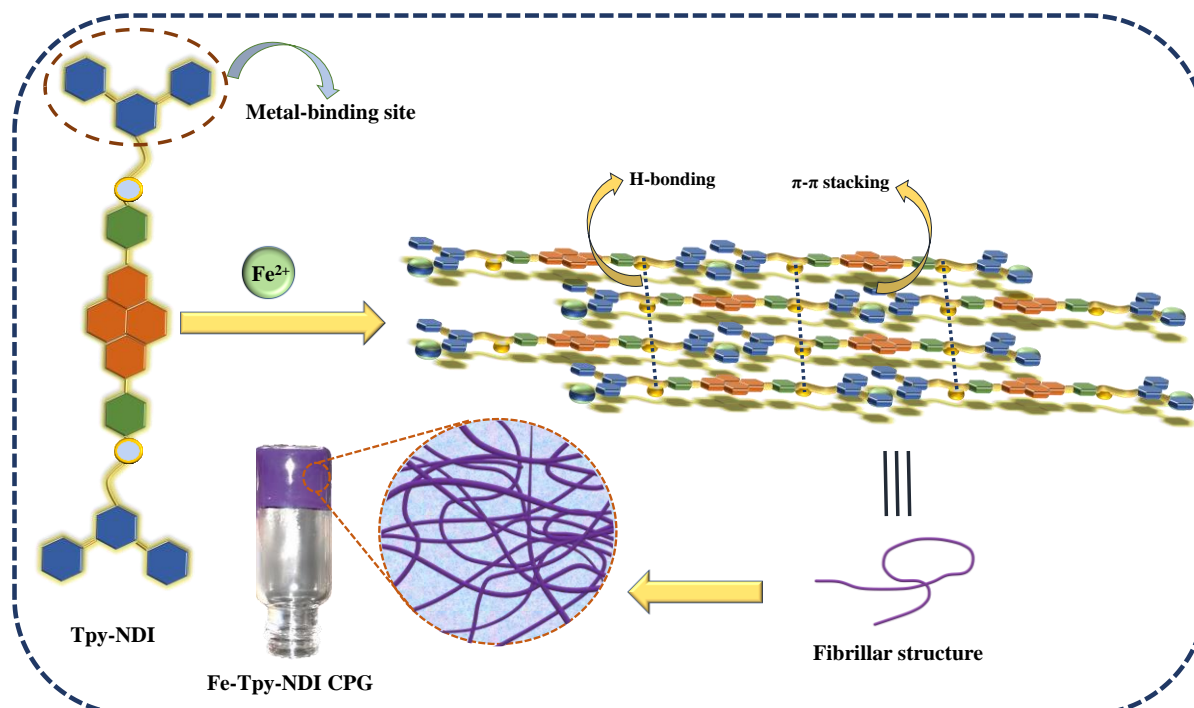


Figure 13. (a) Strain sweep measurement of Fe-Tpy-NDI-CPG with $\gamma\% = 0.01$ -100%.



Scheme 4: Schematic illustration of the self-assembled process of Tpy-NDI with the Fe²⁺ ions to the fibrillar structure.

UV-Vis spectra of the 1:1 solution mixture of the Fe (II) and Tpy-NDI (10^{-6} M) show the characteristic band for the NDI core at 335, 352, and 372 nm (Fig 14a). A broad spectrum starting from 500 nm to 600 nm indicates the MLCT band.²⁶ Photoluminescence spectrum was taken for the 1:1 solution mixture of the Fe (II) and Tpy-NDI (10^{-6} M in DMSO-water) with the excitation at 350 nm (Fig 14b). Two sharp peaks appeared at 411 nm and 436 nm, with a shoulder peak at 463 nm coming from the NDI core. The optical band gap of Fe_Tpy-NDI xerogel was calculated from the Kubelka-Munk plot. DRS study shows that CPG has a bandgap of 2.8 eV (Fig 15a). This bandgap value falls into the visible region (1.6 – 3.1 eV) and also confirms the ability of visible light absorption of the coordination polymer gel Fe_Tpy-NDI, which can act as a catalyst for solar light-driven photocatalytic redox reaction. UV-Vis spectrum was collected for the Fe-Tpy-NDI-CPG, which indicates a broad absorption at 540 to 600 nm due to MLCT transition. The photoluminescence spectrum shows a broad peak from 400 nm to 460 nm, also corroborating the aggregated structure (Fig 15b-c). Fe-Tpy-NDI-CPG was dried in vacuum at 120°C for overnight to get the dried xerogel denoted as Fe-Tpy-NDI xerogel.

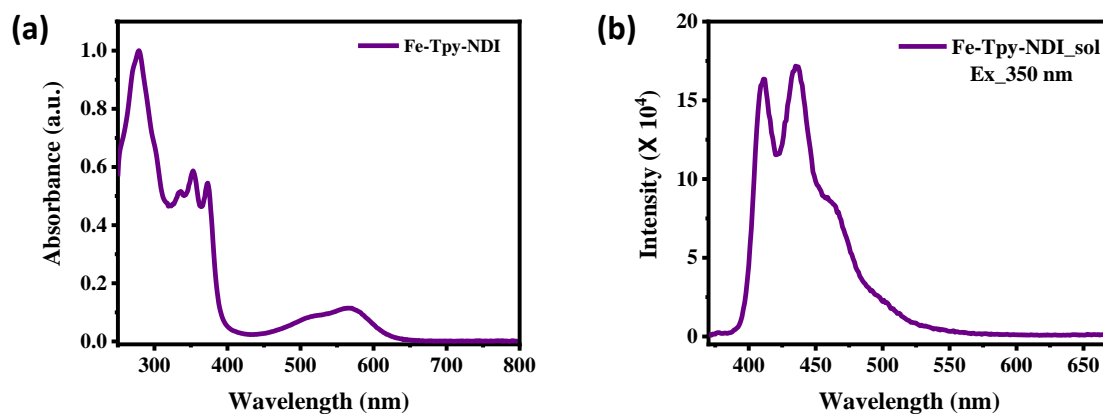


Figure 14. (a) Absorption spectrum of Fe-Tpy-NDI (1:1) in solution state. (b) Emission spectrum of Fe-Tpy-NDI (1:1) in solution state.

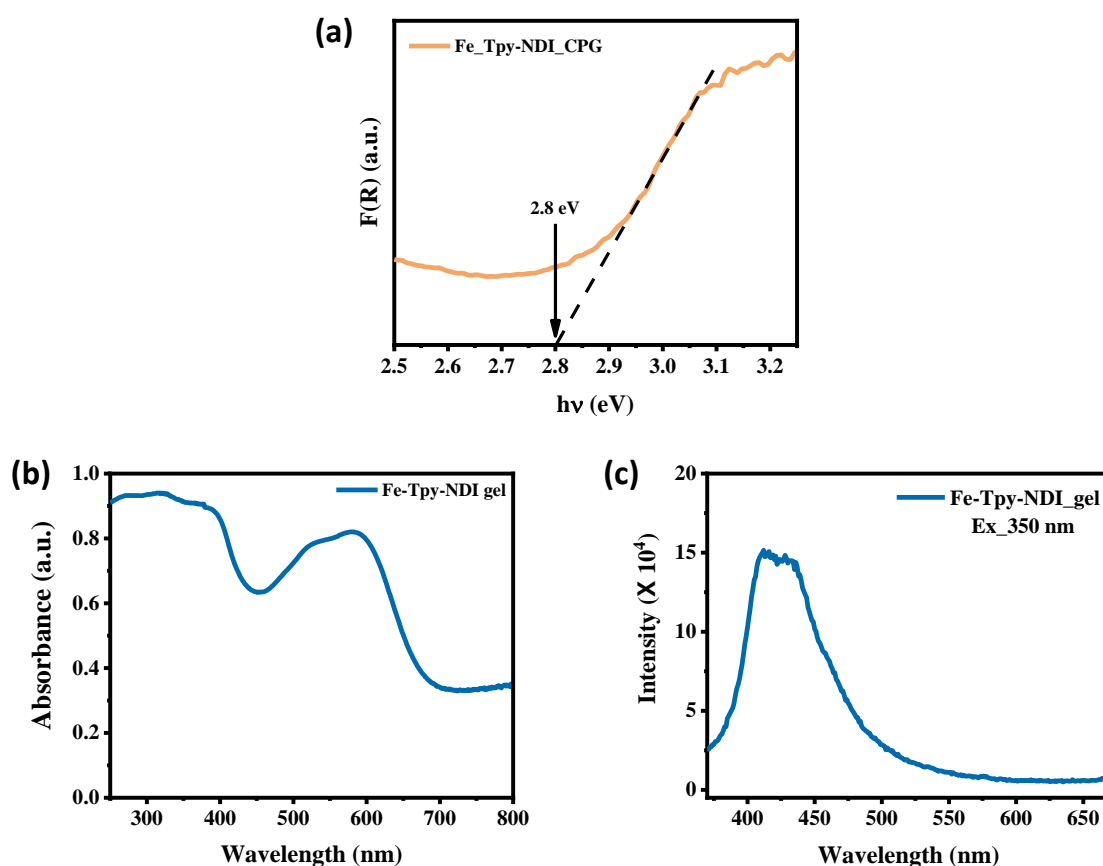


Figure 15. (a) Kubelka-Munk plot for Fe-Tpy-NDI-CPG obtained by Diffused Reflectance Spectra (DRS). (b) Absorption spectrum of Fe-Tpy-NDI-CPG. (c) Emission spectrum of Fe-Tpy-NDI-CPG.

Topographical images of the CPG were collected by field emission scanning electron microscopy (FESEM), atomic force microscopy (AFM), and transmission electron microscopy (TEM) (Fig 16a-d). It shows a flexible fibrous morphology of Fe-Tpy-NDI-CPG. The fibers were having a length in micrometer scale with the height of 30 nm as indicated by the AFM and FESEM analysis.

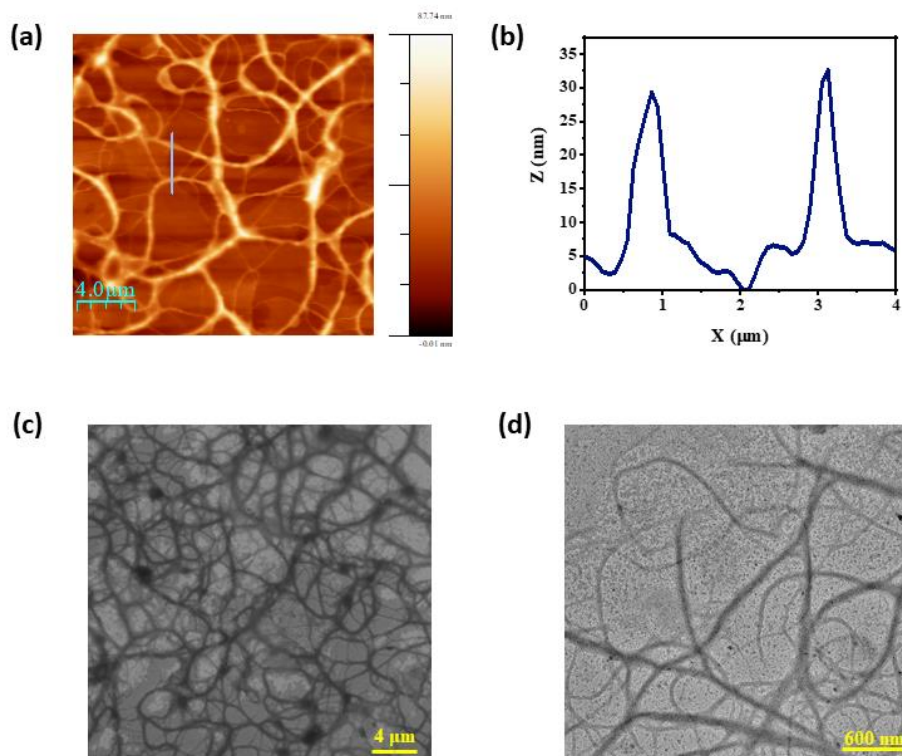


Figure 16. (a-b) AFM image of Fe-Tpy-NDI-CPG with the height profile diagram. (c) FESEM image shows the fibrous morphology of Fe-Tpy-NDI-CPG. (d) TEM image of Fe-Tpy-NDI-CPG.

Further, to ensure the feasibility of the CO₂ reduction process, the Mott-Schottky analysis has been carried out for the Fe-Tpy-NDI xerogel. 0.2 M Na₂SO₄ solution with pH=7 has been used as the electrolyte for the following experiment, and the Fe-Tpy-NDI CPG shows the n-type semiconducting nature with a positive slope. It was also found that slopes were increased with increasing the frequency, but the intersection point was found to be the same for different frequency values. The flat band potential (V_{fb}) was calculated from this curve and found to be -0.55 V (vs. NHE at pH 7) for the Fe-Tpy-NDI CPG (Fig 17a-17b).²⁷ Conduction band edge potential was calculated from this flat band potential. Valance band maximum was also calculated by adding the conduction band edge and bandgap value. These conduction band edge value suggests that the CPG is able to transfer excited state electrons from the conduction band to CO₂.

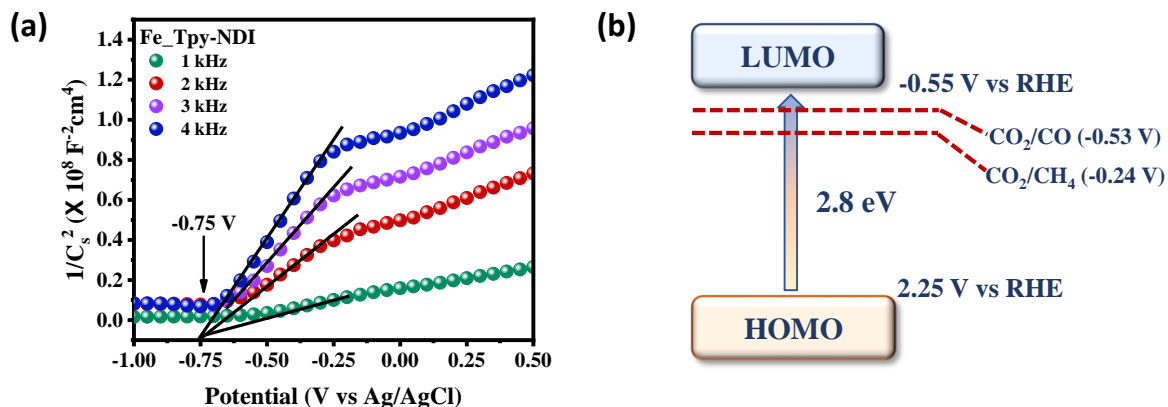


Figure 17. (a) Mott-Schottky plot for Fe-Tpy-NDI-CPG shows the valence band minima. (b) Schematic shows the feasibility of the electron transfer process from LUMO to CO_2 for reduction.

Further, the band alignments were evaluated for separated units to investigate the electron transfer feasibility in the CPG units. Theoretical calculations for $[\text{NDI}(\text{CONH}_2)_2]$ and $[\text{Fe}(\text{TPY})_2]^{2+}$ units were performed by the Density Functional Theory (DFT) method. The Lowest Unoccupied Molecular Orbital (LUMO) levels of $[\text{NDI}(\text{CONH}_2)_2]$ and $[\text{Fe}(\text{TPY})_2]^{2+}$ units were calculated to be -3.7 eV and -2.5 eV (Fig 18a). This suggested a feasible electron transfer process from the metal-coordinated terpyridine unit to the NDI core upon photoexcitation. This electron transfer initiated through the metal to ligand charge transfer (MLCT) transition and finally can be processed for the redox reaction. A reverse phenomenon came into play where the excited electrons jump from the iron-coordinated terpyridine to the π -conjugated NDI core. Further, these electrons were processed for photochemical CO_2 reduction reactions.

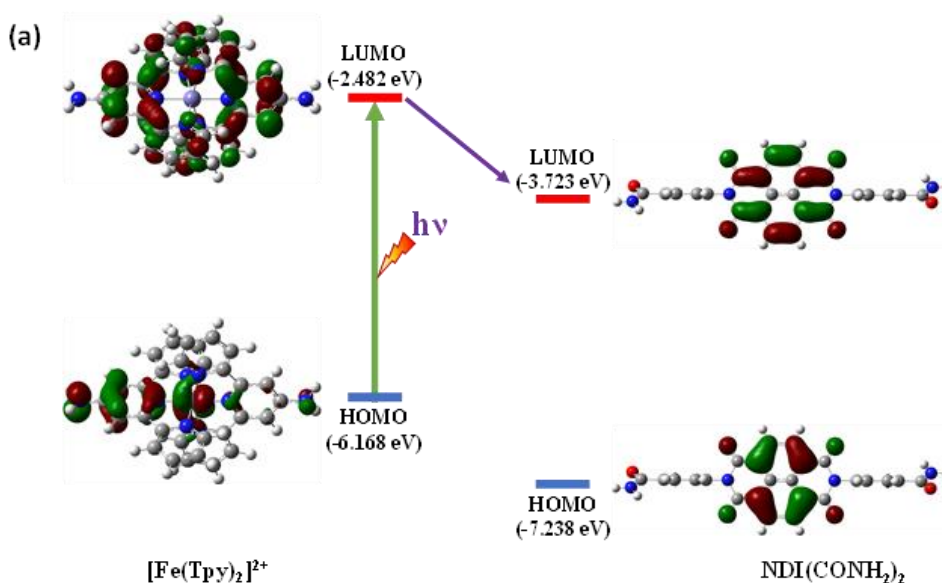


Figure 18. (a) Optimized structure and HOMO-LUMO band alignments of $\text{NDI}(\text{CONH}_2)_2$ and $[\text{Fe}(\text{TPY})_2]^{2+}$ for thermodynamic feasibility of electron transfer.

2.4.4 Visible light-driven photocatalytic CO₂ reduction: Based on the literature survey, it was found that most of the photocatalytic CO₂ reduction process has been carried out in organic solvents with triethylamine and triethanolamine as the sacrificial electron donor. Here we have investigated the photocatalytic activity towards CO₂ reduction in water medium along with electron donor substrate. However, a sacrificial electron donor with lower oxidation potential will be better, and it can tune the reaction pathway under a mild reaction environment. 1-Benzyl-1,4-dihydronicotinamide (BNAH) was found to be a suitable candidate which can fulfill these conditions.¹⁶ The electron donation capability of BNAH towards more selectivity and productivity can be explained by the lower oxidation potential of BANH ($E^{\circ}_{\text{OX}} = 0.57$ V vs. SCE) than that of TEA ($E^{\circ}_{\text{OX}} = 0.7$ V vs. SCE). The presence of more than two redox species in a reaction medium can lead to a faster electron transfer process in photocatalysis reactions. In this present study, BNAH and TEA were both used as the electron donor in the same reaction vessel and found to be more effective than the individual one. CO₂ reduction reaction was carried out under visible light irradiation ($\lambda > 400$ nm) in water medium using BNAH and TEA as sacrificial electron donors, where Fe-Tpy-NDI-CPG was employed as the catalyst. The catalytic assembly showed an outstanding performance towards photocatalytic CO₂ reduction to CH₄ under visible light irradiation without any external co-catalyst or photosensitizer. Catalytic activity was verified in both xerogel and gel states, which leads to similar results for CH₄ formation up to 12 h, but xerogel was used for further studies because of its ease of handling. 1 mg of catalyst was dispersed in 4 mL of water with 2 mg (9.3 mmol) of BNAH and 1 mL TEA in a cap sealed 30 mL quartz vial, and CO₂ was bubbled for 30 minutes prior to light irradiation. Gaseous products formed during the catalytic process were monitored by GC-MS at 2 h of intervals. Photocatalytic CO₂ reduction was found to be saturated after 16 h of continuously visible light irradiation. The highest productivity for CH₄ was found to be 41.2 mmol g⁻¹ with a maximum rate of 2.75 mmol g⁻¹ h⁻¹ with an average rate of 2.45 mmol g⁻¹ h⁻¹. More than 85% of selectivity was obtained for CH₄ in 16 h (Fig 19a-b). The maximum turnover number for CH₄ production was calculated to be 46.83 after 16 h.

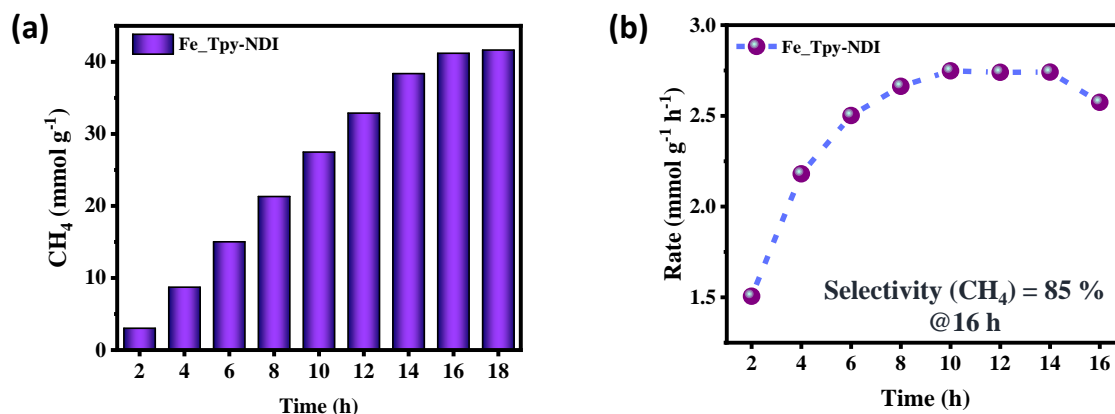


Figure 19. (a) Amount of CH₄ formation by Fe-Tpy-NDI-CPG during the visible light irradiation process in water medium with TEA and BNAH. (b) Rate of formation of CH₄ as a function of time.

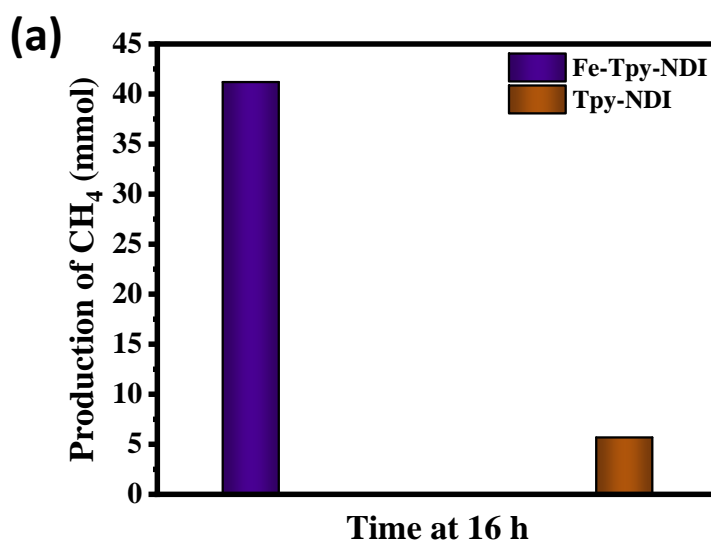


Figure 20. (a) Comparison plot of CH₄ formation by Fe-Tpy-NDI-CPG and Tpy-NDI-OG.

Several control experiments have been carried out to understand the crucial role of each component in this photochemical redox process. No detectable CO₂-reduced product was obtained without light or catalyst. To investigate the role of the metal center, a CO₂ reduction reaction has been performed with the metal-free Tpy-NDI_{OG} under similar conditions as Fe-Tpy-NDI_{CPG} with TEA and BNAH. Organogel shows a much lower catalytic activity than the coordination polymer gel. 5.6 mmol g⁻¹ CH₄ formation was observed after 16 h of visible light irradiation (Fig 20a), suggesting NDI as the active catalytic center. This also suggests an important role of the visible light absorbing metal center in the CPG matrix to act as a heterogeneous catalyst for the photochemical CO₂ reduction reaction. The role of the NDI core in the photocatalytic reduction reaction by eliminating the NDI part and only [Fe-(Tpy)₂]²⁺ complex was chosen as the catalyst under the identical condition. The aforementioned complex forms a homogeneous solution in water, whereas the Fe-Tpy-NDI CPG acts as a heterogeneous catalyst and remains in dispersion state. These studies suggest that the [Fe-(Tpy)₂]²⁺ complex acts as a light-harvesting unit for

the catalytic process, and NDI unit makes the catalyst hydrophobic by acting as the support system for the catalytic center by covalent linkage. Additionally, a negligible CO₂ reduction activity was observed under visible light irradiation for the only [Fe-(Tpy)₂]²⁺ complex. Next, the catalytic activity of the Fe-Tpy-NDI-CPG was assessed using sole sacrificial agents. The addition of individual electron donor components in the reaction mixture displayed inferior activity towards CO₂RR. The catalyst produced 1.5 mmol g⁻¹ and 1.55 mmol g⁻¹ of CH₄ using TEA or BNAH as the sacrificial agent after 12 h. The combined effect of two sacrificial donor species was already explored, and it suggests the pivotal role of TEA as a base. It is well established that the first electron donation takes place from BNAH and is converted to BNAH^{•+}, but these two species hold themselves in an equilibrium that bends towards BNAH side. Here TEA acts as a base to abstract the proton from the radical cation species and accelerates the reduction reaction kinetics by prohibiting the back electron transfer process from the catalyst. As a result, an enhanced activity was found in the photocatalytic CO₂RR process in the presence of both the electron donor. Fe-Tpy-NDI exhibited an outstanding photocatalytic activity and showed excellent stability even after 4 cycles (Fig 21a). After each run, the catalyst was collected by centrifugation, and a dispersion was made for the next cycle. After 20 min of CO₂ bubbling, it was kept under the simulated light for the next cycle. A similar production rate was observed for CH₄ up to the 4th cycle. The fibrous morphology after the completion of the reaction indicates the high stability of this heterogeneous catalyst (Fig 21b). This fact further confirms the firmness of Fe-Tpy-NDI under catalytic conditions. The turnover number for the catalyst was calculated over time, and the highest value was found to be 46.83 at 16 h (Fig 21c).

The origin of the carbonaceous product was investigated by performing a control experiment with argon instead of CO₂ under the same reaction condition, and no detectable carbonaceous product was found. Additionally, photocatalysis was monitored with isotopic CO₂, where ¹³CO₂ was bubbled prior to the irradiation of simulated solar light. The obtained chromatogram shows a mass peak at 17, which originated from the formation of ¹³CH₄. The fact also confirms that it derives specifically from the CO₂ reduction reaction (Fig 22a).

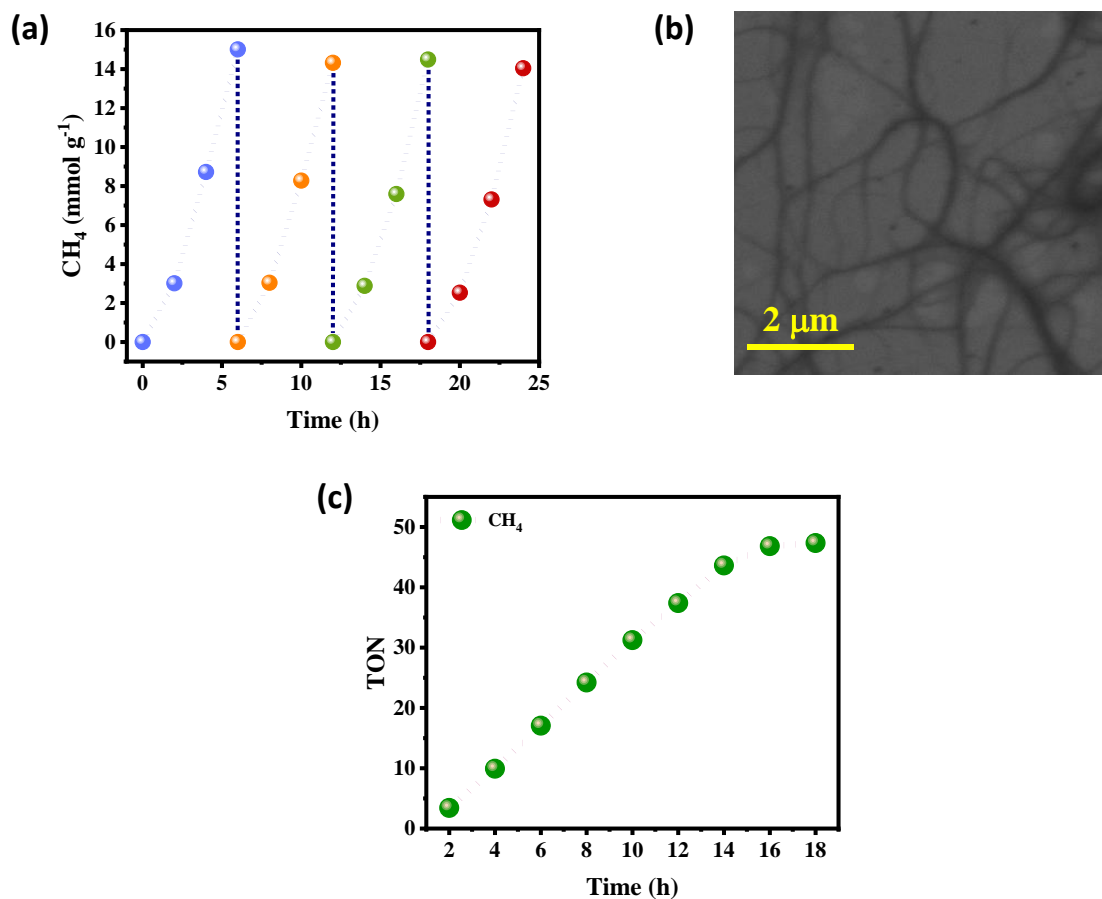


Figure 21. (a) Recyclability test for CH₄ formation by Fe-Tpy-NDI-CPG. (b) FESEM image of Fe-Tpy-NDI shows a similar morphology after the catalysis process. (c) TON for CH₄ formation by Fe-Tpy-NDI-CPG.

(a) Spectrum

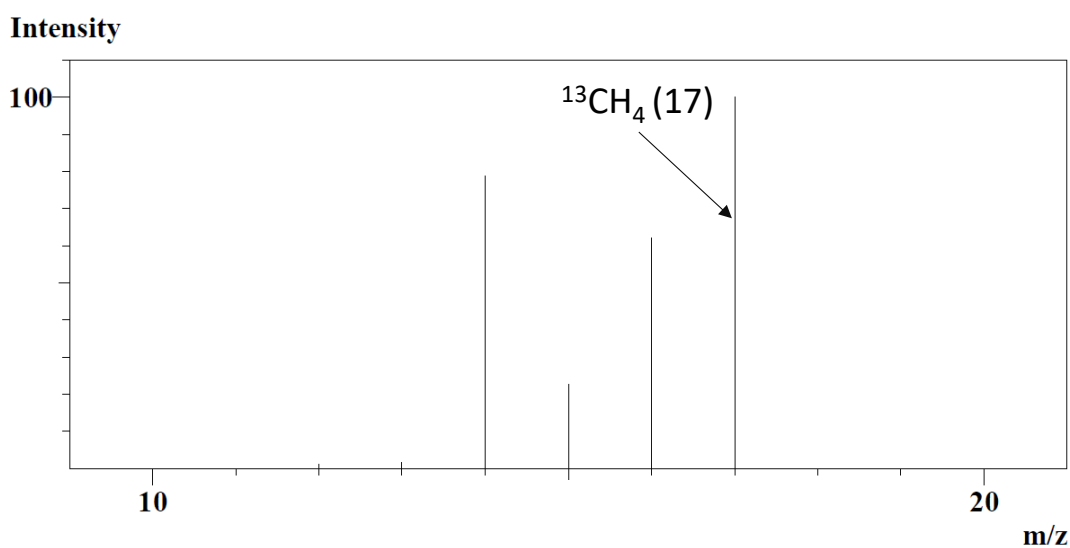


Figure 22. (a) Mass analysis for ¹³CH₄ as a product obtained from ¹³CO₂ saturated sample using Fe-Tpy-NDI under visible light irradiation for 1 hour.

2.4.5 Insights into CO₂ reduction mechanism:

To understand the exceptionally high activity towards photocatalytic CO₂RR, several photoelectrochemical experiments were performed. The Nyquist plot of Electrochemical Impedance Spectroscopy (EIS) shows the charge transfer resistance for the OG and CPG (Fig 23a). The lower semicircle area for the Fe-TPY-NDI CPG than that of Tpy-NDI OG indicates the lesser charge transfer resistance for the CPG. Further lowering of area upon visible light irradiation for the Fe-Tpy-NDI-CPG suggests an easy charge transfer process. Importantly the lowering of the area in the case of organogel under visible light is very negligible, also corroborating the lower absorbance in the visible light of the only Tpy-NDI unit. This demonstrates the difficulty in the charge separation process without UV light and very low activity towards photocatalytic CO₂RR. These studies were additionally supported by the photocurrent study for both samples (Fig 23b). The electrochemical charge transport phenomena were visualized under light and dark conditions. Samples were coated on an ITO plate, and a three-electrode system was employed for this particular experiment. A higher photocurrent in the case of Fe-Tpy-NDI CPG than organogel indicates more feasible in charge transport activity with visible light irradiation. These studies validated the better performance for the Fe-Tpy-NDI CPG than the Tpy-NDI organogel.

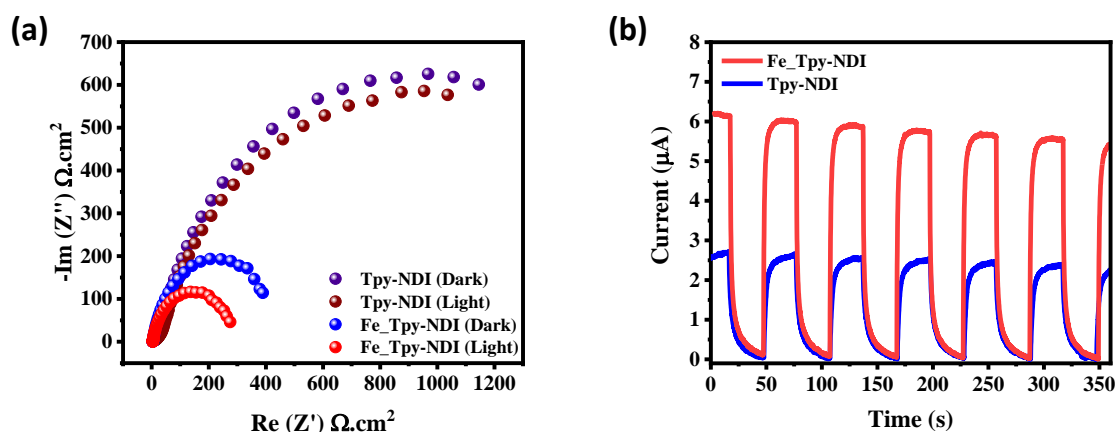


Figure 23. (a) Nyquist plot for Tpy-NDI-OG and Fe-Tpy-NDI-CPG under visible light and dark conditions. (b) Photocurrent measurement in 0.5 M Na₂SO₄ at pH=7 upon visible light irradiation in the time interval of 30 sec.

Next, *in situ* Diffuse Reflectance Infrared Fourier Transform (DRIFT) spectroscopic technique was employed to track the intermediates adsorbed on the catalyst surface along with TEA and BNAH during the photo-redox reaction (Fig 24a). New peaks appeared during

the process. Bands at 1436 cm^{-1} and 1207 cm^{-1} can be attributed to the HCO_3^{2-} species formed by the reaction of CO_2 and H_2O .²⁸ Peaks at 1339 cm^{-1} and 1674 cm^{-1} correspond to monodentate carbonate (m-CO_3^{2-}) and CO_2^- respectively.²⁹ The appearance of IR stretching frequency at 1622 cm^{-1} tells us about a key intermediate COOH^* for the photocatalytic CO_2 reduction process.⁵ The increasing intensity with time at 1492 cm^{-1} and 2082 cm^{-1} indicates the formation of adsorbed CO intermediate on the catalytic surface.⁵ Weak intensity peaks at 1087 cm^{-1} and 1849 cm^{-1} can be attributed to CHO^* , another crucial intermediate for CO_2 to CH_4 production was readily converted into other multi-electron intermediates. Production of CH_2O after 4th electron transfer was confirmed by the rising of peaks at 1249 cm^{-1} , 1709 cm^{-1} , 1779 cm^{-1} .³⁰ Peaks arising at 1045 cm^{-1} , 1125 cm^{-1} , 1161 cm^{-1} can be assigned for CH_3O^* .⁵ Apart from these, symmetric (ν_s) and asymmetric (ν_{as}) stretching vibration peak for $-\text{CH}_2$ was observed at 2886 cm^{-1} and 2983 cm^{-1} , respectively. Symmetric and asymmetric vibration peaks for $-\text{CH}_3$ also can be seen arising at 2937 cm^{-1} and 3077 cm^{-1} .³¹ These results help to understand the progress of photochemical reduction of CO_2 to CH_4 and also corroborate the reaction pathway with the pivotal intermediate.

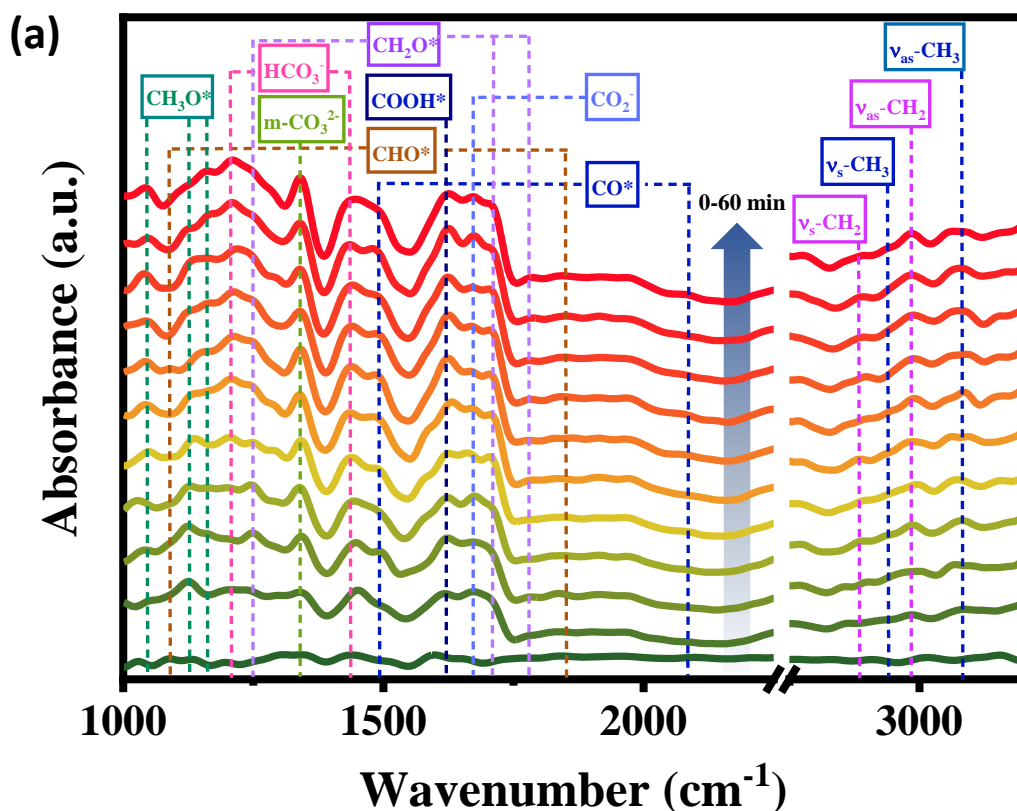


Figure 24. (a) *In situ* DRIFT spectra for a mixture of CO_2 and H_2O vapour on the Fe-Tpy-NDI-CPG under visible light irradiation.

2.5 Summary:

In this study, we have prepared a naphthalene diimide and terpyridine-based soft processable gel materials. Where terpyridine ends were used as the metal binding part of the LMWG, and it forms a coordination polymer gel with metal ion Fe(II). This CPG was used as the catalyst for photocatalytic CO₂RR, and it showed an outstanding performance towards CH₄ formation with high productivity and selectivity. The catalytic redox process was carried out in water medium with TEA and BNAH as the sacrificial electron donor. The feasible reduction process was supported by different photophysical and electrochemical experiments. The *in-situ* DRIFT study also showed the formation of possible intermediate in the CH₄ production pathway.

2.6 References:

- 1 C. Cometto, R. Kuriki, L. Chen, K. Maeda, T. C. Lau, O. Ishitani and M. Robert, *J. Am. Chem. Soc.*, 2018, **140**, 7437–7440.
- 2 D. C. Fabry, H. Koizumi, D. Ghosh, Y. Yamazaki, H. Takeda, Y. Tamaki and O. Ishitani, *Organometallics*, 2020, **39**, 1511–1518.
- 3 C. Gao, Q. Meng, K. Zhao, H. Yin, D. Wang, J. Guo, S. Zhao, L. Chang, M. He, Q. Li, H. Zhao, X. Huang, Y. Gao and Z. Tang, *Adv. Mater.*, 2016, **28**, 6485–6490.
- 4 Ž. Kovačič, B. Likozar and M. Huš, *ACS Catal.*, 2020, **10**, 14984–15007.
- 5 X. Li, Y. Sun, J. Xu, Y. Shao, J. Wu, X. Xu, Y. Pan, H. Ju, J. Zhu and Y. Xie, *Nat. Energy*, 2019, **4**, 690–699.
- 6 S. Karmakar, S. Barman, F. A. Rahimi and T. K. Maji, *Energy Environ. Sci.*, 2021, **14**, 2429–2440.
- 7 J. Albero, Y. Peng and H. García, *ACS Catal.*, 2020, **10**, 5734–5749.
- 8 H. Rao, C. H. Lim, J. Bonin, G. M. Miyake and M. Robert, *J. Am. Chem. Soc.*, 2018, **140**, 17830–17834.
- 9 J. Fu, K. Jiang, X. Qiu, J. Yu and M. Liu, *Mater. Today*, 2020, **32**, 222–243.
- 10 P. Verma, A. Singh, F. A. Rahimi, P. Sarkar, S. Nath, S. K. Pati and T. K. Maji, *Nat. Commun.*, 2021, **12**, 1–14.
- 11 P. Sutar and T. K. Maji, *Chem. Commun.*, 2016, **52**, 8055–8074.
- 12 P. Sutar and T. K. Maji, *Dalt. Trans.*, 2020, **49**, 7658–7672.
- 13 B. Maiti, A. Abramov, R. Pérez-Ruiz and D. Díaz Díaz, *Acc. Chem. Res.*, 2019, **52**,

- 1865–1876.
- 14 A. Das and S. Ghosh, *Chem. Commun.*, 2016, **52**, 6860–6872.
- 15 M. F. Kuehnel, K. L. Orchard, K. E. Dalle and E. Reisner, *J. Am. Chem. Soc.*, 2017, **139**, 7217–7223.
- 16 Y. Kuramochi, O. Ishitani and H. Ishida, *Coord. Chem. Rev.*, 2018, **373**, 333–356.
- 17 K. Gelderman, L. Lee and S. W. Donne, *J. Chem. Educ.*, 2007, **84**, 685–688.
- 18 P. Pengo, G. D. Pantoş, S. Otto and J. K. M. Sanders, *J. Org. Chem.*, 2006, **71**, 7063–7066.
- 19 P. Sutar and T. K. Maji, *Chem. Commun.*, 2016, **52**, 13136–13139.
- 20 A. Sikder, J. Sarkar, T. Sakurai, S. Seki and S. Ghosh, *Nanoscale*, 2018, **10**, 3272–3280.
- 21 S. M. Wagalgave, S. D. Padghan, M. D. Burud, M. Al Kobaisi, D. D. La, R. S. Bhosale, S. V. Bhosale and S. V. Bhosale, *Sci. Rep.*, 2019, **9**, 12825.
- 22 R. Parveen, N. Maity and P. Dastidar, *Chem. - An Asian J.*, 2018, **13**, 170–180.
- 23 H. Kar and S. Ghosh, *Chem. Commun.*, 2016, **52**, 8818–8821.
- 24 D. Chakraborty, D. Sarkar, A. K. Ghosh and P. K. Das, *Soft Matter*, 2021, **17**, 2170–2180.
- 25 P. Verma, F. A. Rahimi, D. Samanta, A. Kundu, J. Dasgupta and T. K. Maji, *Angew. Chemie Int. Ed.*, , DOI:10.1002/anie.202116094.
- 26 S. Mukherjee, P. Pal, A. Sahoo and S. Baitalik, *J. Photochem. Photobiol. A Chem.*, 2021, **407**, 113059.
- 27 S. Barman, A. Singh, F. A. Rahimi and T. K. Maji, *J. Am. Chem. Soc.*, 2021, **143**, 16284–16292.
- 28 L. Liu, H. Zhao, J. Andino, Y. Li and J. Accepted, *ACS Catal.*, 2012, **2**, 1817–1828.
- 29 J. Fu, B. Zhu, C. Jiang, B. Cheng, W. You and J. Yu, *Small*, 2017, **13**, 1603938.
- 30 W. Wang, D. Xu, B. Cheng, J. Yu and C. Jiang, *J. Mater. Chem. A*, 2017, **5**, 5020–5029.
- 31 R. Zhang, H. Wang, S. Tang, C. Liu, F. Dong, H. Yue and B. Liang, *ACS Catal.*, 2018, **8**, 9280–9286.

Chapter 3

***Self-assembly of Ga-MOC and $[\text{Ni}(\text{en})_3]^{2+}$ by
charge assisted H-bonding interaction:
Understanding of Gel to Crystal
transformation***

Abstract

This chapter discusses the self-assembly of the Ga^{III} containing metal-organic cubes (Ga-MOCs) ((Me₂NH₂)₁₂(Ga₈(ImDC)₁₂)·DMF·29H₂O) and [Ni(en)₃]²⁺ (en = ethylenediamine) binder molecules towards gel to crystal transformation. The tris-ethylenediamine Ni^{II} complex is chosen as a binder which connects Ga-MOCs through charge-assisted hydrogen bonding. The structural units promote the supramolecular self-assembly in water, leading to a hydrogel. This strong hydrogen bonding interaction results in a transition from gel to crystal. This transformation underwent with time and resulted in phase-separated solution and precipitate. The crystallisation process was studied in detail by varying the stoichiometric ratio, and a correlation was drawn with the mechanical shear modulus of the gel with the time of crystallisation. The morphological study also inclined with the rheological parameters a high contact surface overlap for the high concentration facilitates the microcrystal formation process by helping to cross the thermodynamical energy barrier.

3.1 Introduction:

The self-assembly process using small molecules¹⁻⁴ or metal-organic polyhedras (MOPs)⁵⁻⁷ as the building blocks is a powerful bottom-up technique for producing functional nanomaterials. These assembled structures are found to form a metastable gel state.⁸ For the formation of gel, the organic peptide systems are the primary choice in most cases.⁹⁻¹¹ However, there are reports of gel formations with metal-organic hybrid systems also. Most of the time, the self-assembly process is found to be unidirectional, which leads to a fibrillar nanostructure.^{12,13} Non-covalent interactions are found as the main driving force for this self-assembly process.¹⁴⁻¹⁷ The 3D entangled fibrous network acts as a sponge which restricts the flow of the liquid and makes it a soft material.¹² These supramolecular gels are generally found to be stable over time or sometimes assumed as there are no aging effects on the nanostructure.¹⁸⁻²⁰ However, a deep investigation on the aging effects shows an increase in the crystallinity of the gel matrix often found a phase transformation.²¹ A detailed gel to crystal transition study shows that in most cases, the transformation takes place with the expense of the entangled, and a cross-linked gel matrix leads to phase-separated solutions and crystals.²²⁻²⁶ There is always a competition between the gelation and crystallisation processes as both phenomena are initiated by the self-assembling of the gelators.¹² A controlled growth of the assembled structure to a particular direction leads to fibrillar structure for gelation, whereas the three-dimensional growth generally ends up with crystal formation. However, there is an argument between the structural similarity of the gel structure and the structure obtained from the single-crystal.²³ Generally, it is assumed that, there is a similarity between the gel and the xerogel state, which is nothing but an intact gel structure without the solvent molecules. Most of the time the X-ray diffraction pattern of the xerogel matched with the simulated pattern of the single crystal depicting structural similarity in both the state. In some cases, it is also found that powder X-ray diffraction pattern is not matched with the single crystal X-ray diffraction pattern.²⁷

Most of the gel to crystal transformation processes are reported with a single-component systems; only a few are available with bi or multicomponent. Smith *et al.* showed a gel to crystal transformation process with a donor-acceptor-based bi-component system.²⁸ There are some advantages of a multicomponent systems compared to a single component, such as the mechanical strength was found to be higher in a multicomponent systems than in a single component one. Despite several advantages of a multicomponent systems, the number of reports is less. Probably, because of the complicacy in the characterisation and understanding of such a systems.

An extensive study has been carried out from the different corners of the globe with the fluorenylmethyloxycarbonyl (F-moc) group functionalised hydrogelator to realise the gel to crystal transformation process.^{13,29–31} The different peptide derivative of F-moc shows excellent gelation, which also transforms into microcrystals upon the application of different external stimuli.^{21,27,32,33} Gel is considered as the metastable kinetically trapped state of the self-assembling molecules, and therefore, the crystallisation process from the gel can be triggered by different external stimuli.³⁴ Whereas, in some cases, the gel to crystal transitions are also found as a spontaneous processes. This gel to crystal transition process has the potential which is yet to be explored. The gel is a kinetically trapped state; hence theoretically, it might also be possible to transform into different definite polymorphs depending on the crystallisation environment.

Herein, we have explored a spontaneous gel to crystal transition phenomena with a bi-component system. To the best of our knowledge, this is the first report for the bi-component gel to crystal transformation process where a metal-organic hybrid system has been used. A systematic investigation also showed that the mechanical strength of the hydrogel could be tuned by changing the stoichiometric ratio of the components. A detailed morphological analysis reveals the origin of this spontaneous transformation.

3.2 Experimental section:

3.2.1 General: 4,5-Imidazolecarboxylic acid (H_3ImDC), Gallium nitrate hexahydrate [$Ga(NO_3)_3 \cdot 6H_2O$], Nickel(II) Nitrate trihydrate ($Ni(NO_3)_2 \cdot 3H_2O$) were purchased from Sigma-Aldrich chemical Co. Ltd. All solvents and triethylamine (NEt_3) were obtained from Spectrochem Pvt. Ltd. (Mumbai, India).

3.2.2 Single-crystal X-ray diffraction: X-ray single-crystal structural data of 1 was collected on a Bruker Smart-CCD diffractometer equipped with a normal focus, 2.4 kW sealed tube X-ray source with graphite monochromated Mo- $K\alpha$ radiation ($\lambda = 0.71073 \text{ \AA}$) operating at 50 kV and 30 mA. The program SAINT was used for integration of diffraction profiles and absorption correction was made with SADABS program. All the structures were solved by SIR 92 and refined by full matrix least square method using SHELXL-97. All the nonhydrogen atoms were refined anisotropically and the hydrogen atoms were fixed by HFIX and placed in ideal positions. All calculations were carried out using SHELXL 97, PLATON and X-Seed Ver 4.

3.2.3 Powder X-ray Diffraction Measurements: Powder X-ray diffraction (PXRD) patterns were collected in gel state coated on a glass plate and taken by a Rigaku Smartlab SE instrument using Cu $K\alpha$ radiation.

3.2.4 Thermal Stability Measurements: Thermogravimetric analysis (TGA) was carried out using Mettler Toledo TGA 850 instrument under inert atmosphere in the temperature range of 25-800°C at the heating rate of 5°C per min.

3.2.5 Morphological analysis: Atomic force microscopy (AFM) measurements were carried out with Asylum MFD-3D Origin to analyse the morphologies of the sample surface. Samples were prepared by making a dispersion of the xerogels in THF and coated on a silicon wafer by the drop-casting method. The Field Emission Scanning Electron Microscopic (FE-SEM) images were recorded on a Zeiss Gemini SEM 500. Samples were prepared by the drop-casting method on a small piece of Si wafer and loaded in the machine without any gold sputtering.

3.2.6 Rheological analysis: The rheological study was done in Anton Paar Rheometer MCR 92 using plane plate geometry on a Peltier glass plate. The diameter of the plate was 60mm, and the measuring unit had a diameter of 25mm. The gel samples were placed on the plate and stress sweep experiment at a constant frequency at 25 °C, and frequency sweep measurements at constant stress in the linear viscoelastic range were carried out to get the storage or elastic modulus (G') and loss or viscous modulus (G'') values of the gel materials.

3.2.7 ATR-IR Measurements: The ATR-IR experiment measurements were carried out using an FT-IR spectrophotometer (BRUKER, VORTEX 70B) in the region 4000–400 cm^{-1} .

3.3 Synthesis:

3.3.1 Synthesis of Ga(III) Metal-Organic Cube: Synthesis of Ga(III) Metal-Organic Cube was previously reported by our group, we have followed the same solvothermal method.³⁵ 4, 5-Imidazoledicarboxylic acid (4, 5-ImDC) (0.5 mmol, 78 mg), $\text{Ga}(\text{NO}_3)_3 \cdot \text{H}_2\text{O}$ (0.5 mmol, 128 mg) and 10 ml DMF were mixed in a 20 ml Teflon container and stirred for 30 minutes at room temperature. 15 μl triethylamine was added to the reaction mixture and stirred for an additional 30 minutes. After that, the Teflon container was kept inside a stainless steel autoclave which was heated at 120 $^\circ\text{C}$ for 24 hours. Next, the autoclave was slowly cooled down to room temperature, and the white product was centrifuged with washing repeatedly by methanol and dried in air. PXRD (Fig 1a). FTIR data (cm^{-1}) (Fig 1b): 3447 (b), 3086 (m), 2775 (m), 1676 (s), 1473 (s), 1363 (s), 1100 (s), 857 (m), 660 (m), 550 (m) is well-matched with the literature.

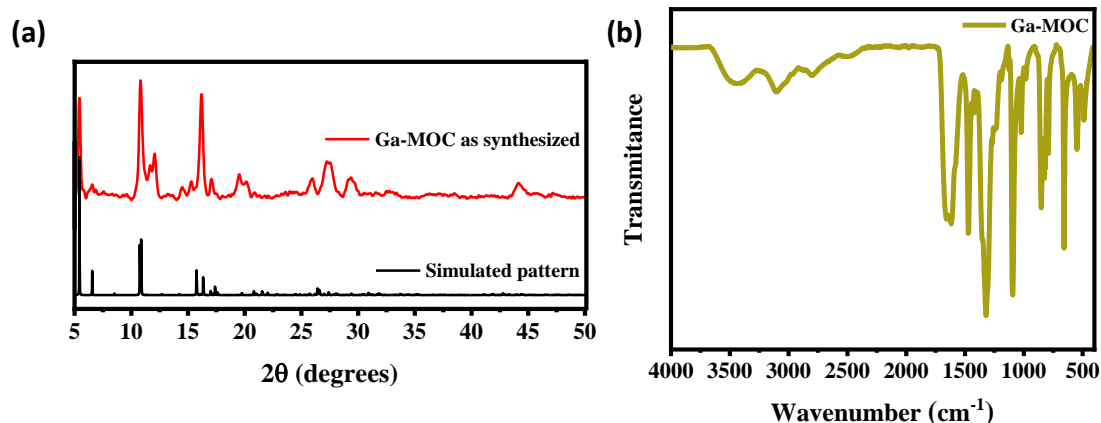


Figure 1. (a) PXRD pattern of Ga-MOC simulated (black) and as synthesised (red). Peaks indicates the phase purity (b) ATR spectra of as synthesised Ga-MOC.

3.3.2 Synthesis of tris(ethylenediamine)nickel(II) nitrate (Ni-EDA complex):

We have followed the reported procedure for the synthesis of the Ni-EDA complex.³⁶ $\text{Ni}(\text{NO}_3)_2 \cdot 6\text{H}_2\text{O}$ (500 mg, 1.72 mmol) was dissolved into 10 mL of ethanol, and 3 equivalents (a little excess) of ethylenediamine (5.5 mmol) was added dropwise into it under stirring condition over 10 minutes. A faint violet colour precipitate formed, filtered under suction, and washed with ethanol. Powder X-ray diffraction (Fig. 2a) was collected, and it is well-matched with the simulated pattern.

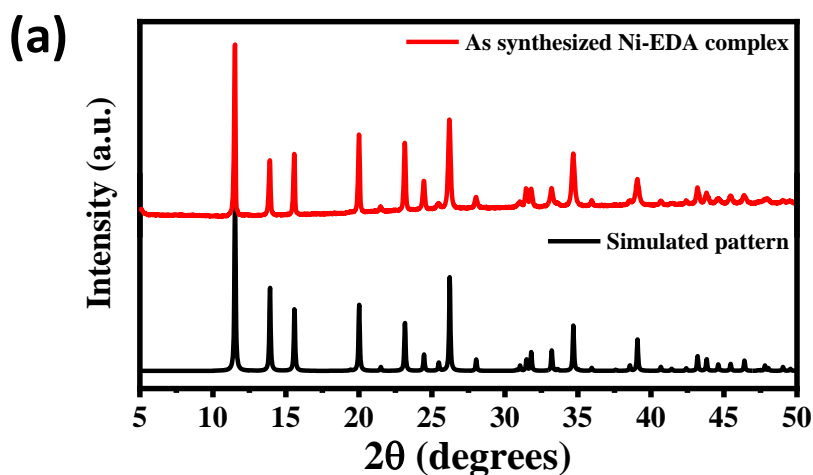


Figure 2. (a) PXRD pattern of $[\text{Ni}(\text{en})_3](\text{NO}_3)_2$ simulated (black) and as synthesised (red). Peaks indicates the phase purity.

3.4 Results and discussion:

A previous study of Ga-MOC and Cu^{II} ethylenediamine complex showed the instantaneous formation of hydrogel just after the addition of the binder solution to the Ga-MOC solution. Charge-assisted hydrogen bond (CAHB) driven gelation followed by a crystallisation process was observed after some days. This interesting phenomenon drives us to investigate the spontaneous phase transformation process in more detail. Instead of Cu^{II} ethylenediamine, a Ni metal ion-based tris ethylenediamine complex was used here to understand the universal nature of gelation and the phase transformation process. For the formation of hydrogel, a 0.01 M aqueous solution of Ga-MOC was taken into a small vial, and an aqueous solution of 0.1 M of tris(ethylenediamine)nickel(II) nitrate was added dropwise. Immediate gelation was observed with the addition of binder solution to the solution of Ga-MOC. An opaque gel was obtained with faint violet colour, the same as the colour of the Ni-EDA complex. The transition of the two free-flowing solution to an opaque stable gel indicates that the monomer units of the MOC transformed into the self-assembled structure by linking each other with the help of the binder (Ni-EDA complex). Here the pendent oxygen from the carboxylate group of the MOC framework plays an important role in solubility by making a single unit highly charged. These oxygens are not only acting as a crucial component for the solvation process but also help to arrange the MOC into a self-assembled structure by connecting themselves with the binder molecules through CAHB. The critical gelation ratio of the Ga-MOC and Ni-EDA complex was determined to be 1:4 and confirmed by the inversion test method.

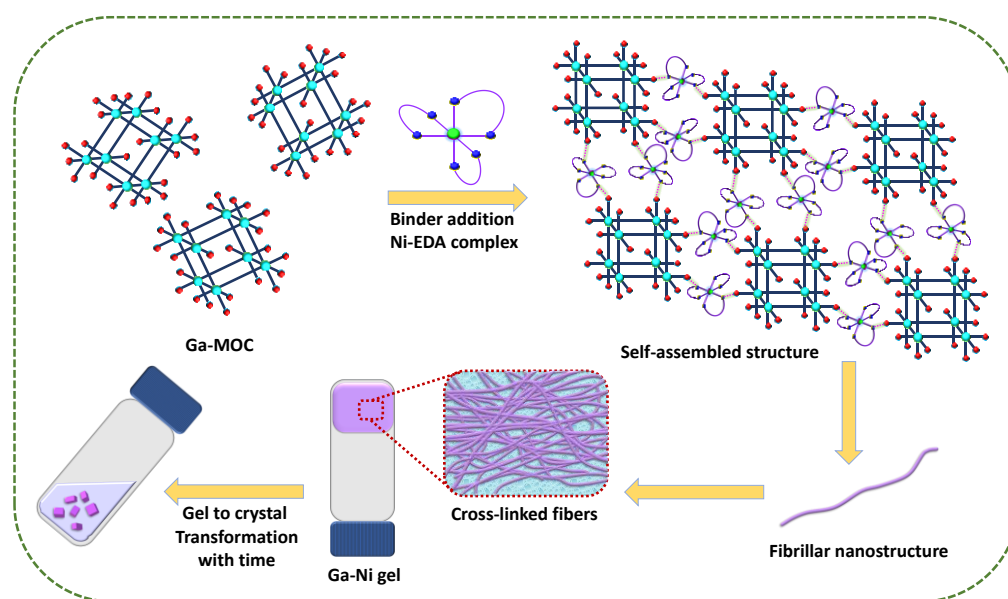


Figure 3. Schematic representation of the self-assembly process of the Ga-MOC with Ni-EDA complex to a fibrillar nanostructured hydrogel followed crystallisation process.

Gelation was checked by the inversion test method, and the rheology experiment also confirmed the formation of the gel. To investigate the viscoelastic nature of the gel, a shear strain was applied to the material with the help of two-disc plates under a constant angular frequency of 1.5 Hz. The hydrogel was scanned with a long-range of shear stress starting from a very lower value of 0.01% to 100%. The Ga-Ni hydrogel was found to be stable up to a shear strain of 5%, and after that, it transformed into sol as indicated by the cross-over point.

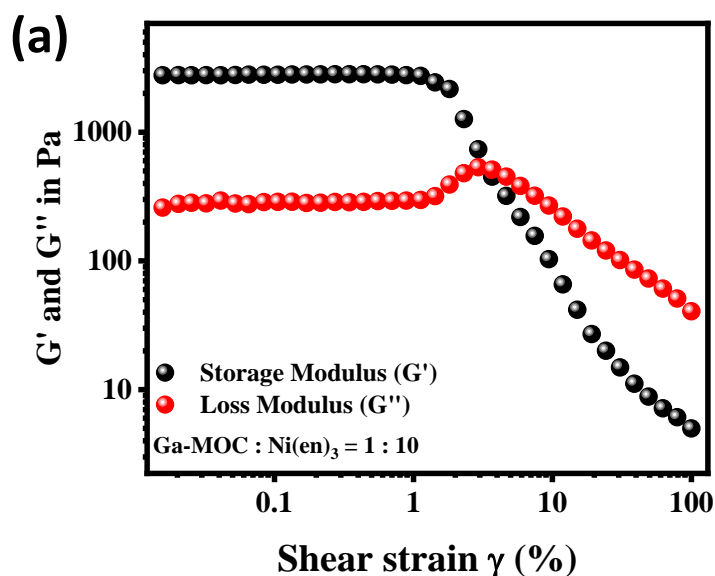


Figure 4. (a) Amplitude sweep measurement of Ga-Ni gel. Storage modulus (G') (black circle) has a higher value than loss modulus (G'') (red circle), indicating the viscoelastic nature.

The storage modulus (G') is one order higher than the loss modulus (G''), which indeed confirms the formation of gel (Fig. 4). Here the storage modulus represents the potential of the gel matrix to return to its original structure after removing the applied shear stress, and the loss modulus indicates the propensity of the material to flow with the applied shear force like a liquid. A higher value of storage modulus than the loss modulus indicates the dominating elastic nature of the gel. The linearity of both the curves under a lower shear region reveals the viscoelastic nature of the gel, which has an in-between behaviour of liquid and solid. A value of the loss factor ($\tan \delta$) in-between 0 and 1 up to the cross over point also suggests the phase difference of shear stress and the shear strain has a value medial of 0° to 90° tells that the hydrogel is not a perfect solid or a perfect liquid.⁸ Next, to investigate the thixotropic nature of the gel matrix, it was shaken to break the hydrogen bond interaction, and a gel to sol transition

occurred (Fig. 5). When the sol was kept for half an hour in undisturbed condition, again, the sol was transformed into a gel state.

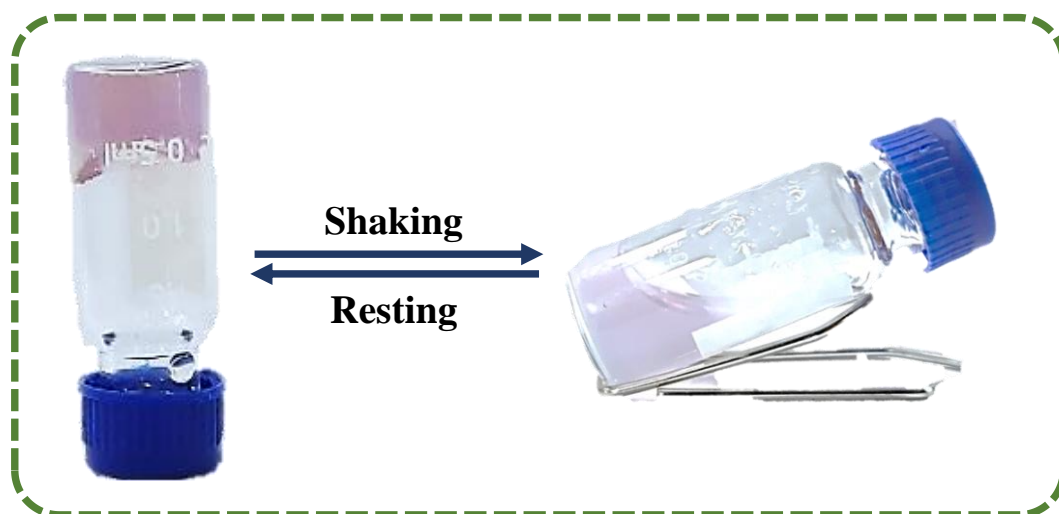


Figure 5. Mechanical stimuli driven gel to sol transition and upon resting it again transformed into gel.

The obtained hydrogel was kept in ambient condition for drying to get the powder form, and it was named as Ga-Ni xerogel. Next Attenuated Transmission Reflectance (ATR)-IR study has been carried out for Ga-MOC, Ni-EDA complex, and Ga-Ni xerogel (Fig. 6a-b). All the peaks which are presents in the individual component of the gel were also found to remain intact in the xerogel, indicating the structural stability in the xerogel. A Peak observed at 3100 cm^{-1} for Ga-MOC spectra indicates the aromatic C-H stretching frequency. Bands at 1658 cm^{-1} and 1323 cm^{-1} can be designated for C=O and C-N stretching, respectively. Two distinguish peaks at 3329 cm^{-1} , and 3297 cm^{-1} in the Ni-EDA complex indicate the N-H stretching band. However, a bathochromic shift was found for these two bands in the xerogel. Peaks came at 3323 cm^{-1} , and 3276 cm^{-1} in the Ga-Ni-xerogel spectra with a shift of 6 cm^{-1} , and 21 cm^{-1} , respectively, suggesting the involvement of the N-H bond in the hydrogen bonding.²⁶ IR spectra for the Ni-EDA complex also show the peaks at 3121 cm^{-1} , 1388 cm^{-1} , and 1029 cm^{-1} can be attributed to the C-H bond stretching, CH_2 bending, and C-N stretching, respectively. The thermal stability of the assembly was monitored by the thermogravimetric analysis curve in the xerogel state (Fig. 7). It was observed that the Ga-Ni xerogel was stable up to 190°C . The TGA curve also shows a weight loss of 24% at the temperature of 190°C . This can be attributed to the loss of the solvent molecules (water and DMF) in the Ga-MOC units.³⁵ Next 18% weight loss was found to be started at 270°C due to the degradation of the $[\text{Ni}(\text{en})_3]$ complex.

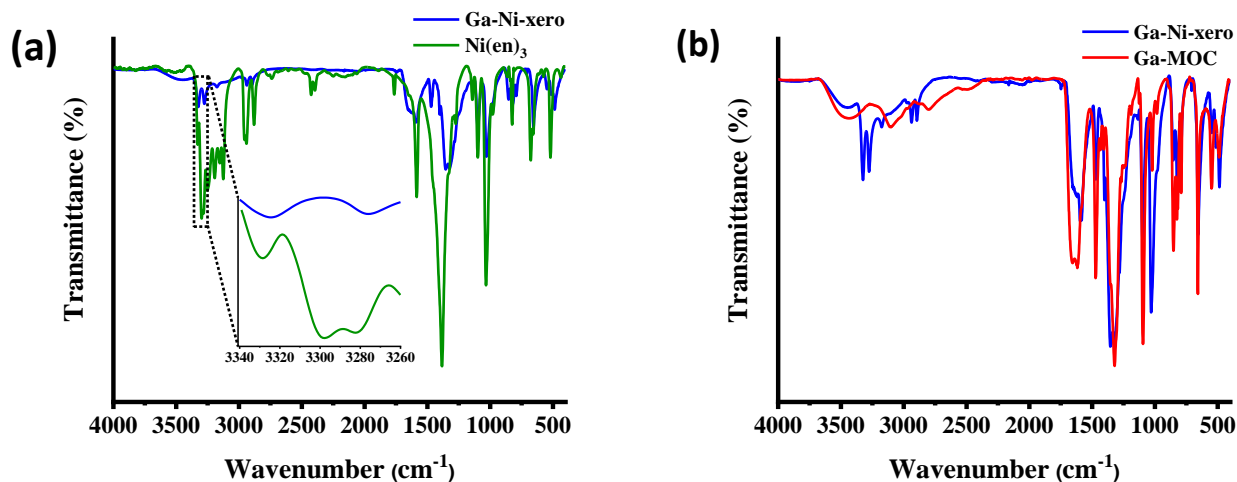


Figure 6. (a)-(b) ATR spectra of Ga-Ni xerogel (blue), Ni-EDA complex (green). Ga-MOC (red).

The morphological analysis was carried out with field emission scanning electron microscopy (FESEM) and atomic force microscopy (AFM) technique. Ga-Ni hydrogel shows a highly interconnected fibrous network structure (Fig. 8a-c). AFM analysis of the Ga-Ni gel also confirms the fibrillar nanostructure. The micrometer long fibers have a height of ~20 nm, and the width was calculated to be in the range of 300-400 nm, as indicated by the AFM studies.

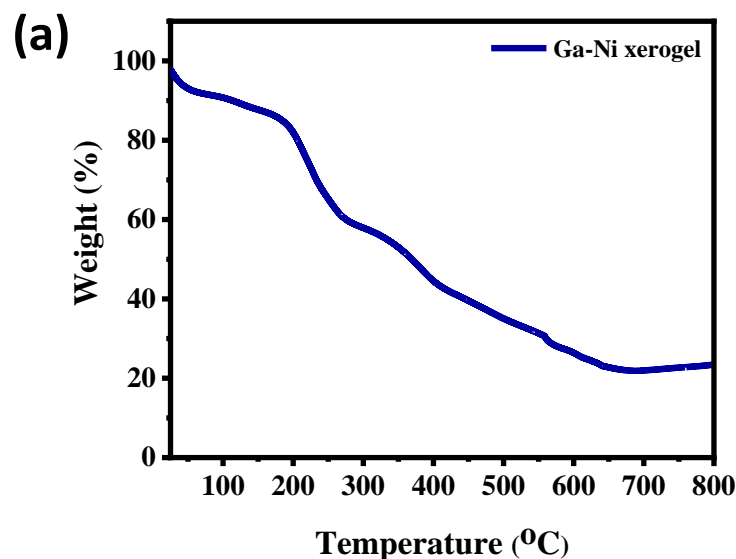


Figure 7. (a) TGA curve of Ga-Ni xerogel shows the stability up to 200°C.

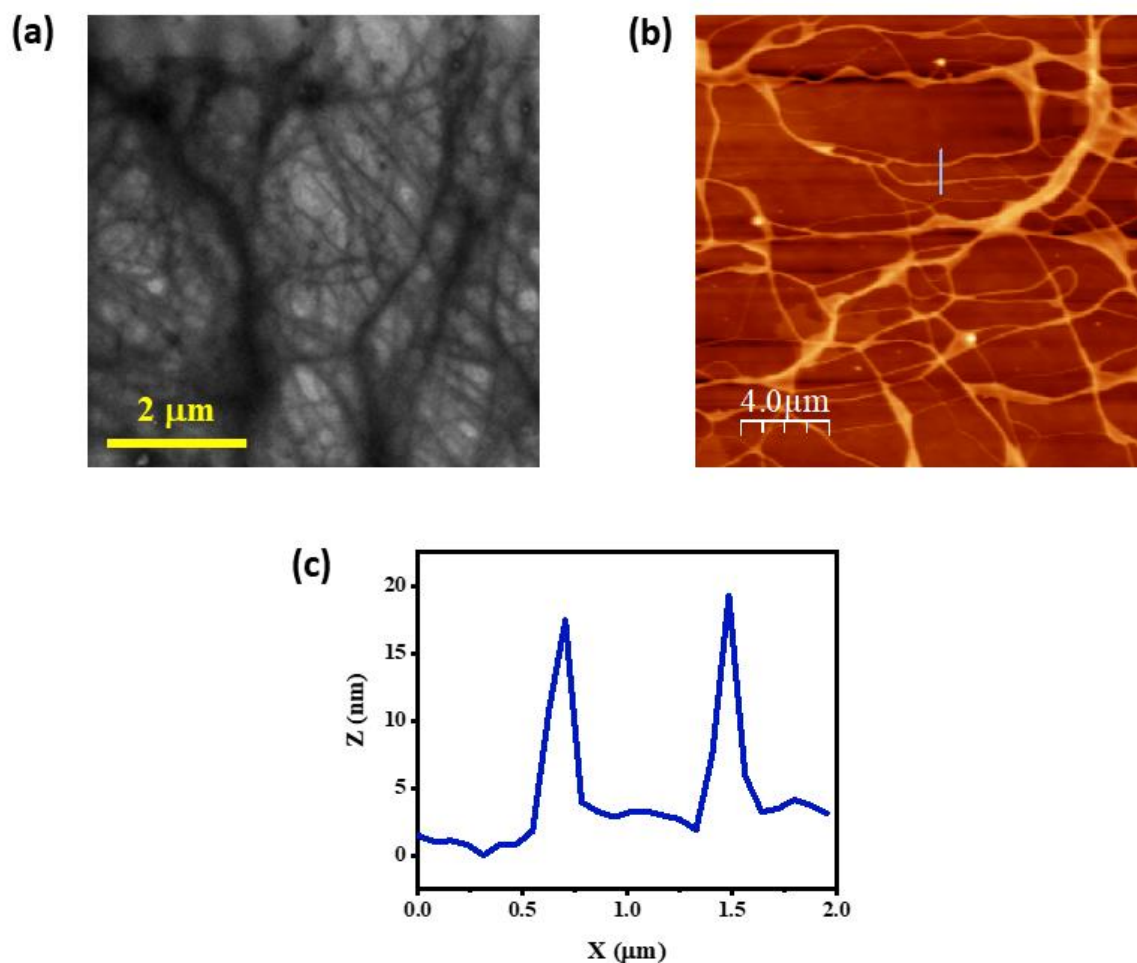


Figure 8. (a) FESEM images of Ga-Ni xerogel shows interconnected fibrous structures. (b) 2D AFM image of the Ga-Cu xerogel also confirms the fibrillar morphology. (c) Height profile diagram of the fibers obtained in AFM.

3.4.1 Gel to crystal transition:

We have also tried the combinations for other ratios to check the minimum gelation stoichiometric ratio. The Ga-MOC:Ni-EDA complex ratio was varied from 1:9 to 1:1. The rheology experiment was carried out by varying shear strain and keeping the angular frequency constant for different stoichiometric ratio gels which have already passed the inversion test (Ga-MOC:Ni-EDA complex = 1:10 to 1:4). In the cases of 1:3, 1:2, and 1:1 stoichiometric ratios, there was no gel formation rather, a free-flowing liquid was found. An interesting phenomenon was observed with the rheological experiment for different concentration ratio gel. A gradual decrease in elastic storage modulus (G') was noticed starting from 1:10 to 1:4, which indicates a decrease in the mechanical strength of the system with lowering the concentration of the binder Ni-EDA complex (Fig. 9a-f).²⁷ Therefore, according to this equation, $G = G' + iG''$, the shear modulus of the gels was also decreasing (G is the complex

shear modulus and G'' is the loss modulus). As the formation of gel is driven by the CAHB between the binder and the MOC, lowering the amount of binder in the vicinity of the Ga-MOC leads to a decrease in the number of hydrogen bonding and also the stiffness of the gel.

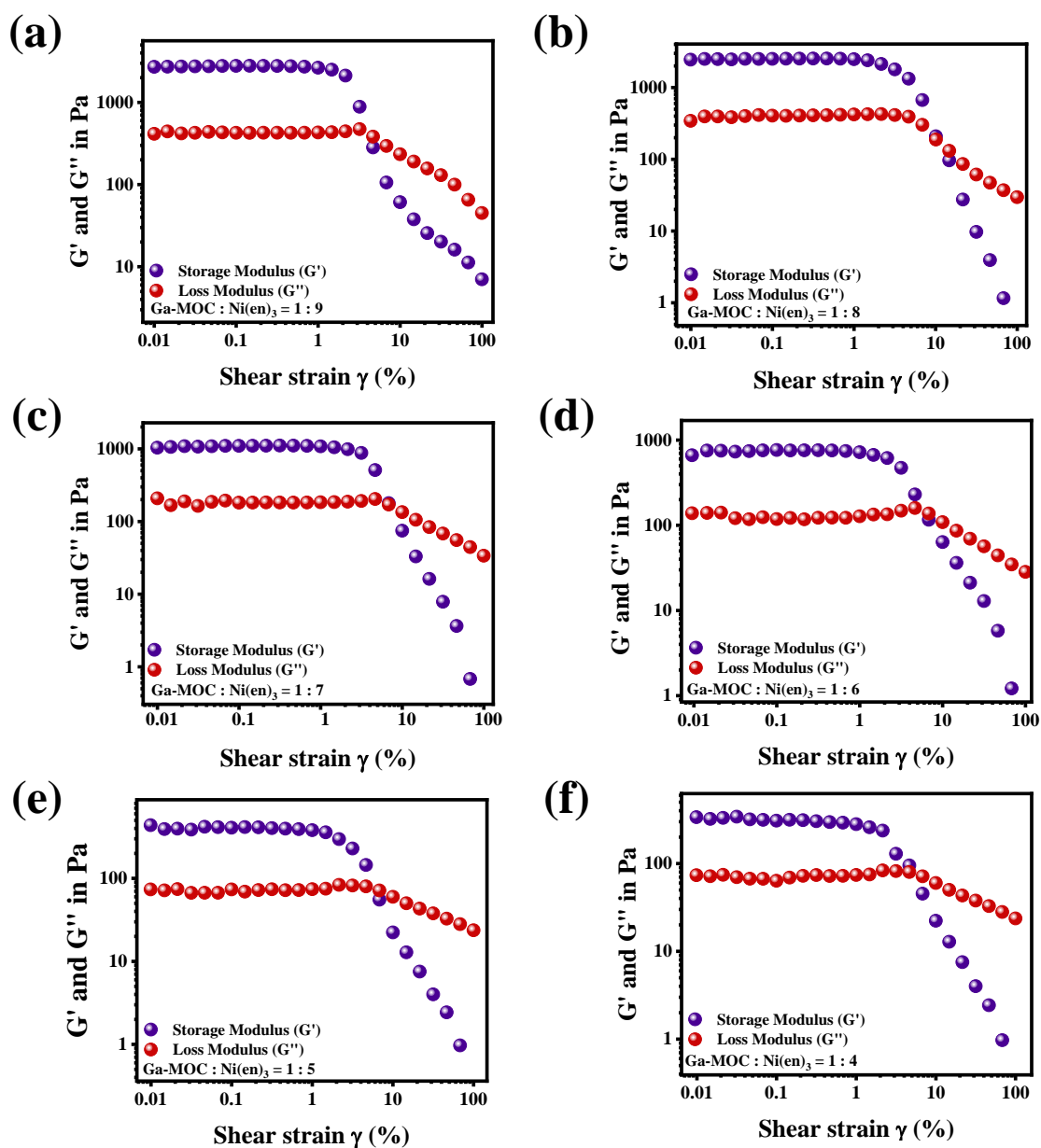


Figure 9. Strain sweep rheology measurement of Ga-Ni gel with different stoichiometric ratio (a) Gel (1:9) (b) Gel (1:8) (c) Gel (1:7) (d) Gel (1:6) (e) Gel (1:5) (f) Gel (1:4).

Herein we kept all the gel samples for a long time to check the stability and the capability of the gel matrix to capture the solvent molecules; an interesting phenomenon was observed. Without the application of any external stimuli, a gel to crystal transition takes place. It was observed that a different time scale was required in the crystallisation process for different stoichiometric ratio gel. For all the different ratio gels, the transformation was found to be spontaneous, but the transition time was different in each case. With decreasing the amount of Ni-EDA complex, the time scale goes to a higher value, also corroborating the rheology study. Visible crystals were found just after 6 hours of the formation of the gel in the case of 1:10 (Ga-MOC:Ni-EDA complex), whereas the 1:4 (Ga-MOC:Ni-EDA complex) gel sample takes 4 days to form the visible crystals. All the other ratio gels took an intermediate time for this particular conversion. This evolution process was first observed with a visible weakening of the gel matrix with the formation of some microcrystals. After the formation of microcrystals, the degree of crystallisation was found to be increased for the next 48 hours and ended up with the rupture of the integrated gel structure and a phase-separated state of solvent and the precipitate. Presumably, the transformation of the reticular fibril structure to a closed packed microcrystal leads to the degradation of the gel matrix, and there is also a decrement in the solvent holding capacity. To the best of our knowledge, there is no report to date for such kind of gel to crystal transformation without any external perturbation, where a metal-organic-cubes were used with a binder as the bicomponent system. A comparative rheological experiment was carried out for all the gel samples by keeping the shear strain constant and varying the oscillatory angular frequency. The linear behaviour of the curve for both the storage modulus (G') and loss modulus (G'') indicates the gels were stable under the strain of 1% throughout the angular frequency (ω) range from 0.1 rad/s to 100 rad/s. All the stoichiometric gel samples showed a minute dependency of the storage modulus (G') and loss modulus (G'') on the angular frequency. A gradual decrease was found in the storage modulus (G') value when the concentration of the Ni-EDA complex went to a lower value (Fig. 10a).⁵ The correlation between crystallisation time and storage modulus (G') was evaluated from the curve given in Fig. 10b. A linear relation was observed between the time of crystallisation and the storage modulus value at the angular frequency of 1 rad/s under the viscoelastic region.

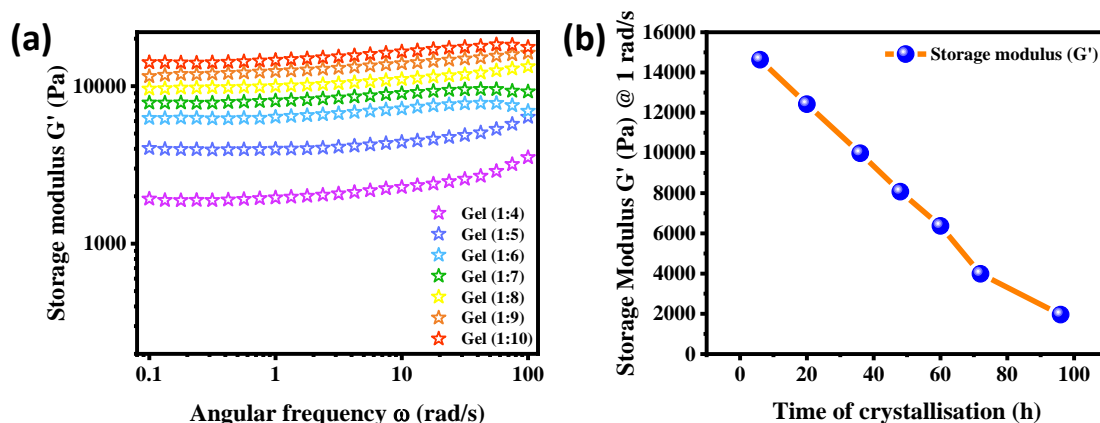


Figure 10. (a) Angular frequency sweep rheology data of different stoichiometric gel [(1:4) to (1:10)] show less dependency of the storage modulus on the angular frequency under viscoelastic conditions. (b) A plot of Storage modulus vs. time of crystallisation process showing linear relation with the gel stiffness.

To understand the topology of the different gel matrices and the correlation of the transition time scale with the different concentrations of Ni-EDA complex, a detailed FESEM, and AFM study were performed. The study was done with four different concentration ratios (1:4, 1:6, 1:8, 1:10) and all of them showed an interconnected fibrillar network structure under the electron microscope (Fig. 11) and AFM (Fig. 12). A distinct change in the connectivity of the fiber network was found in each case under FESEM.^{27,34} A higher association was observed with increasing the ratio, which also corroborated with the higher stiffness and higher elastic modulus. As there was an increase in the number of nodes in the fibrillar structure along with the fibrillar density, the stiffness of the gel increased. The higher elastic modulus (G') value in the rheology experiment with increasing the concentration ratio also indicates a rise in complex shear modulus ($G = G' + iG''$). The topographical images from FESEM and AFM gave a visual representation of that only. Higher mechanical strength with the increment in the fibrillar connectivity generated from the enhanced hydrogen bonding interaction leads to a faster crystallisation process. This increase in the fusion of the fibers also transforms the solvated gel state to a rhombus shape crystal. A comparative AFM study showed that the height of the fibrils obtained in all cases are almost same and was calculated to be in the range of 15-20 nm. Next, the width of the fibrils were also calculated, and it was found that Ga-Ni gel (1:10) had the fibrils width in the range of ~ 400 nm, whereas in the case of Ga-Ni gel (1:4), the width was found to ~ 200 nm. Presumably, the lower concentration of the Ni-EDA complex binder restricts the growth process of the fibrils.

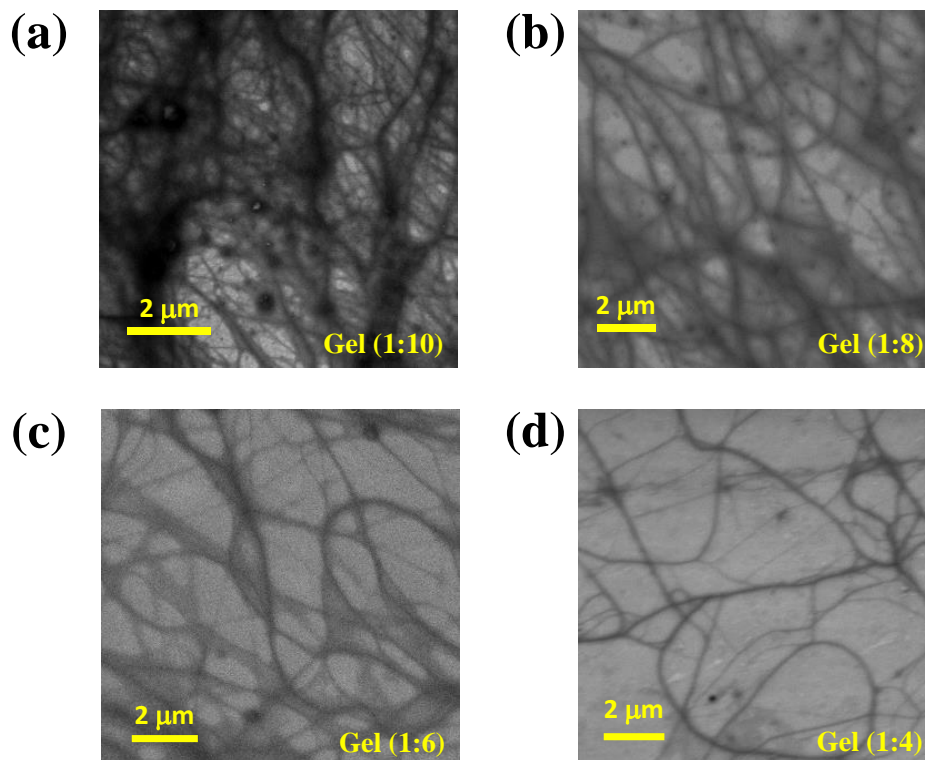


Figure 11. FESEM images of Ga-Ni gels showing fibrous nanostructure. (a) Gel (1:10) (b) Gel (1:8) (c) Gel (1:6) (d) Gel (1:4), a decrement in contact surface overlap with the lowering of the Ni-EDA complex concentration.

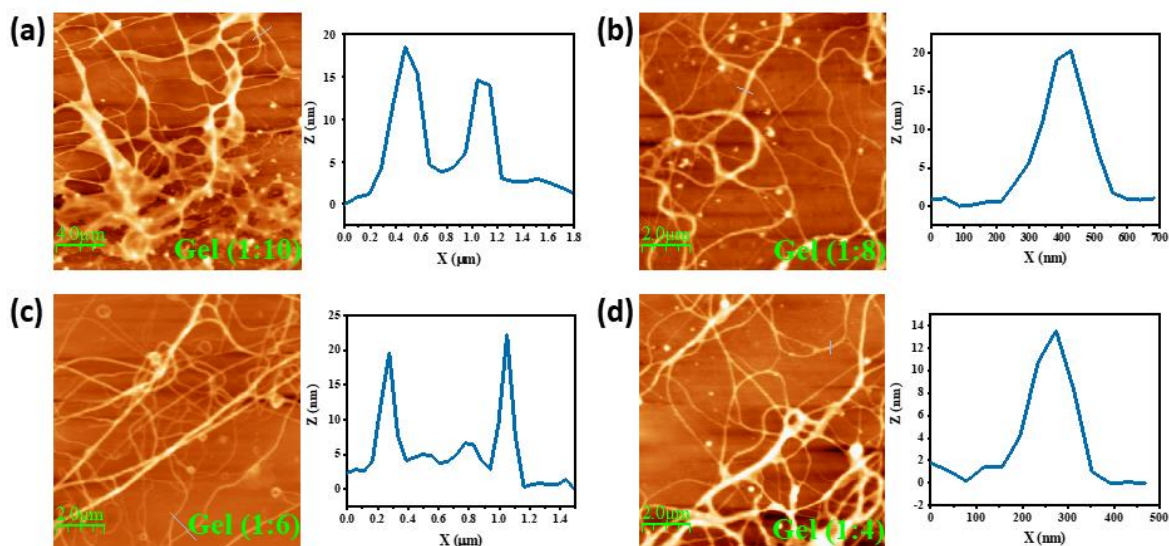


Figure 12. Atomic force microscopic images of Ga-Ni gels with different stoichiometric ratio shows the fibrillar structure. (a). Gel (1:10) (b). Gel (1:8) (c). Gel (1:6) (d). Gel (1:4).

The gel state is considered as the thermodynamically metastable form of the self-assembled aggregated structure with a local minimum, and the crystal is known for having a close-packed, highly ordered structure with a global minimum.^{34,37} Now, these two states of material are connected through an energy barrier, and the assembly has to cross it during the phase transformation process (Fig. 13). The hydrogen bond formed just after the addition of the binder to the Ga-MOC solution was not in a very well-oriented fashion. This has crucial importance in holding the components into the gel state and helps to attain the local minimum. Proper placement of the binder molecules helps the system to attain the global minima. The fibrillar structure of the gel samples indicates the metastable trap state of the system, which remains in equilibrium with its soluble parts. In comparison, the lower fibrillar connectivity is not sufficient to overcome the energy barrier to attain the global minimum. At the junction of these fibers, the amount of contact surface overlap (CSO) is much higher, and these nodes help in the ripening process by acting as a seed for crystal growth. Therefore, the lower concentration ratio gels have a lower number of the contact point (node) that remains stable as in gel state for a longer time. Consequently, the higher concentration ratio gels were able to reach the transition state easily with having a lower depth of metastable local minimum. Rebalance in the orientation of the binders and stronger association by the hydrogen bond interaction stabilises the aggregation state into a long-range crystalline network.

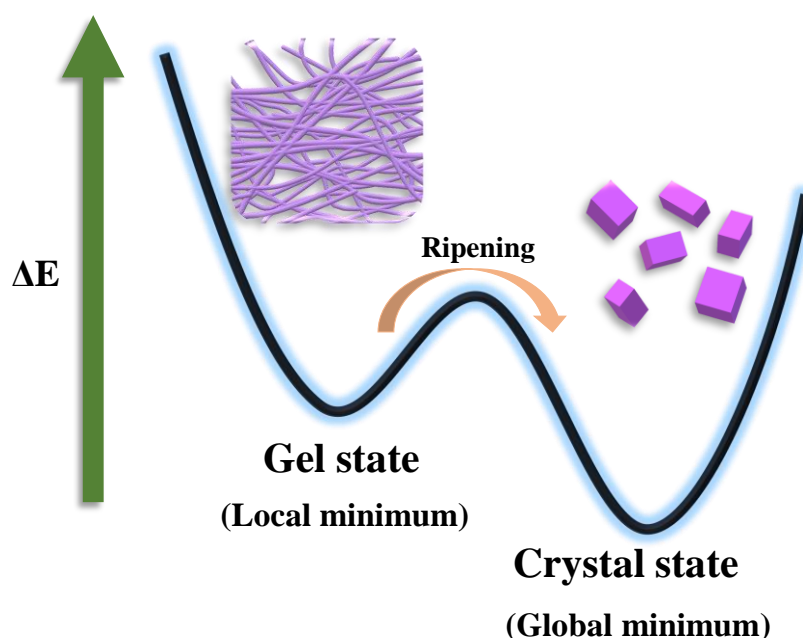


Figure 13. Schematic of the switching of local minimum fibrillar Ga-Ni gel state to the global minimum crystal state through the strong hydrogen bond interaction between Ga-MOC and Ni-EDA complex.

3.4.2 Single Crystal X-ray Diffraction Analysis (SCXRD):

To understand the role of the binder (Ni-EDA complex) towards gelation and crystallisation process, the stoichiometric ratio of the Ga-MOC and the Ni-EDA complex was varied from 1:1 to 1:10. The rheological data confirmed that the gel was obtained only in the cases of 1:4 to 1:10 stoichiometric ratio. There was no gelation and crystallisation process found in the case of 1:1, 1:2, and 1:3 ratio combination as the initial interaction was not sufficient to form the gel. For the increasing ratio of the Ni-EDA complex, the gel was found to be stiffer, as indicated by the rheological study. The crystallisation process was found for all the cases where it is forming the gel. This indicates that the gelation is the crucial step in the crystallisation process, where it helps to hold the Ga-MOC and Ni-EDA binder in close vicinity for further close packing. We have diffracted all the crystals obtained from different stoichiometric gels, and the obtained cell parameters are given in table 1. The geometrical shape of the crystals was also found to be improving with the increasing amount of Ni-EDA complex, as given in Fig.14. When we have diffracted the crystals, it was found that a minor number of spots were coming for the crystals obtained from 1:4, 1:5, and 1:6 stoichiometric gel. Whereas for all other stoichiometric ratios (1:7 to 1:10), the obtained crystals gave a good number of diffraction spots. This study suggested the lower crystallinity of the single crystals for the lower stoichiometric. In contrast, the improvement in the crystallinity was found with the increasing amount of Ni-EDA complex. This indicated the important role of the binder in gelation and followed by crystallisation process. SCXRD for the crystals starting from the 1:7 to 1:10 ratio gel indicates that the Ga-MOC was crystallising in the triclinic $P\bar{1}$ space group with the help of a binder Ni-EDA complex. To investigate the arrangements of the Ga-MOC and Ni-EDA in the 1:4, 1:5, and 1:6 ratio crystals, we have compared the PXRD pattern of all the xerogel, and it was found to be the same in all cases (Fig. 15). Therefore, the Ga-MOC and Ni-EDA complex combined to form the long-range ordered crystals in the same arrangements, but with the lowering in the concentration of the binder, the crystallinity was found to be decreasing.

<i>Stoichiometric ratio gel</i>	a (Å)	b (Å)	c (Å)	α (°)	β (°)	γ (°)	Volume (Å ³)
<i>1:7</i>	17.91	18.15	18.21	116.13	107.52	95.63	4879
<i>1:8</i>	18.06	18.11	18.19	116.04	107.52	95.21	4922
<i>1:9</i>	18.14	18.16	18.23	116.18	107.82	94.81	4964
<i>1:10</i>	17.93	18.14	18.20	116.01	106.97	95.73	4910

Table 1. Unit cell parameters of different crystal shows a similarity obtained from different stoichiometric ratio Ga-Ni gel.

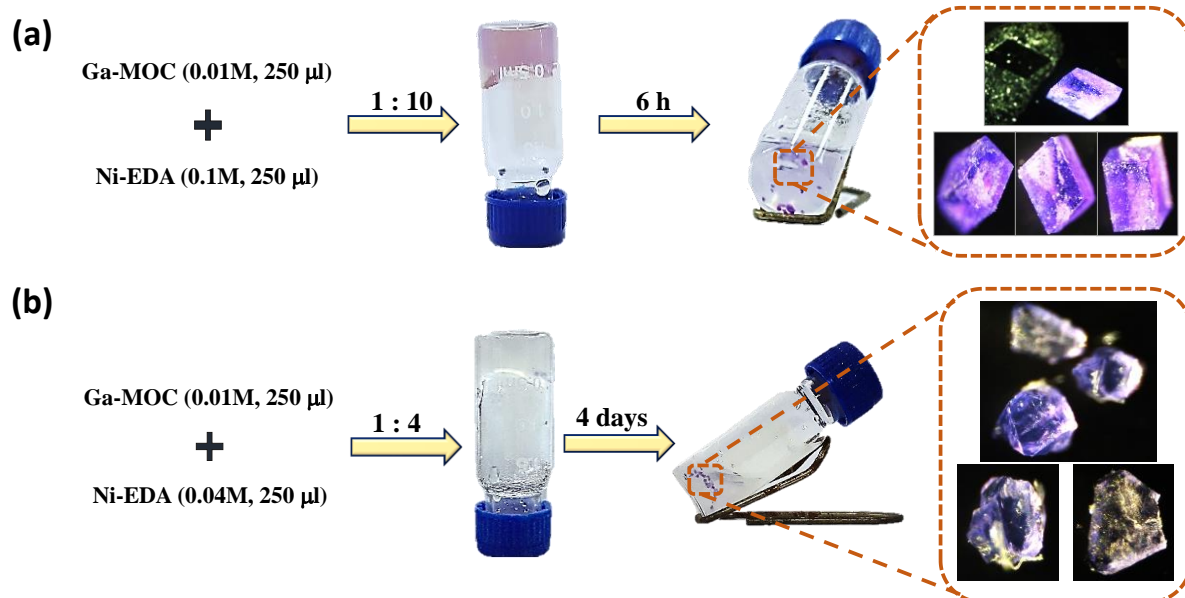


Figure 14. (a) formation of Ga-Ni gel (1:10) followed by transformation in rhombus shaped crystals within 6 hours. (b) Formation of the Ga-Ni gel (1:4) and transformation into crystals with undefined geometrical shape after 4 days.

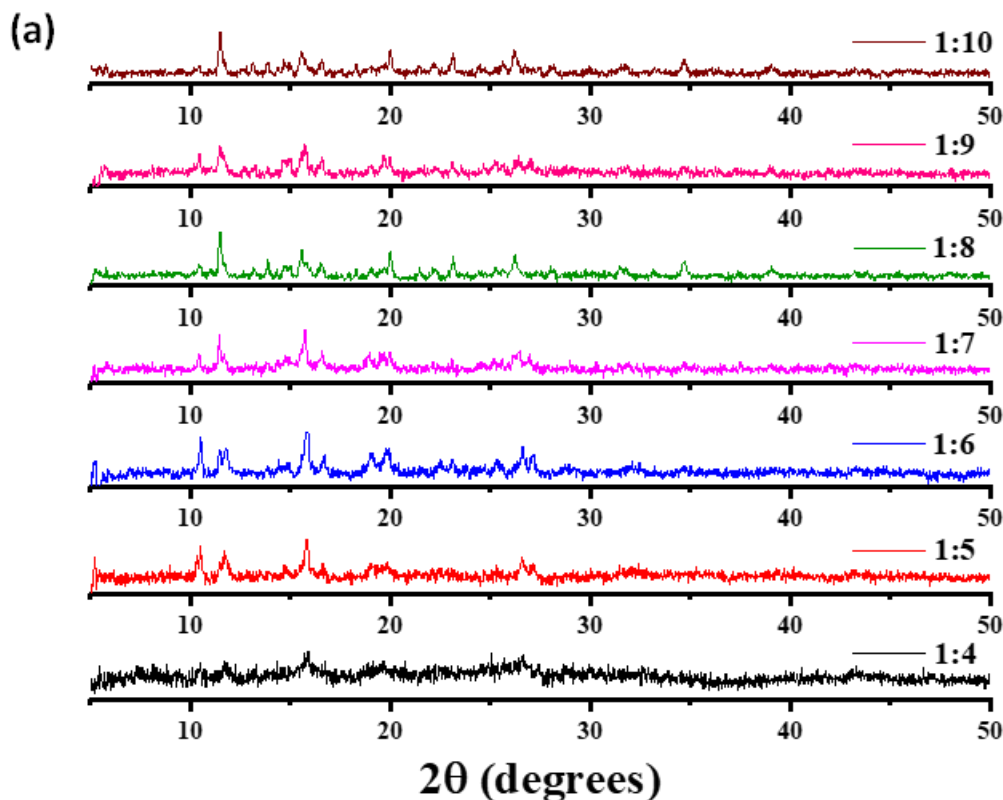


Figure 15. (a) PXRD pattern comparison of the xerogel obtained from the different stoichiometric gel.

A rhombus-shaped crystal was taken from the 1:10 ratio gel, and the single-crystal X-ray diffraction study was performed to understand the packing of the Ga-MOC with the binder Ni-EDA complex. X-ray diffraction data were collected with a violet coloured crystal having the dimension of $271 \mu\text{m} \times 271 \mu\text{m} \times 138 \mu\text{m}$. The SCXRD analysis showed that the self-assembly of the Ga-MOC with the binder crystallises into a triclinic $P\bar{1}$ space group. The unit cell contains a single number of Ga-MOC and is surrounded by the six Ni-EDA complexes. Each MOC had 12- charges which compensated with the 12+ charges from the six Ni-EDA complexes leading charge neutralisation within a unit cell. SCXRD also confirmed the structural stability of the Ga-MOC and the Ni(en)₃ complex in both gel and crystal states. The only interaction was found in this self-assembled structure is the charge-assisted hydrogen bonding. As shown in Fig. 16, the Ga-MOC was encircled by six Ni-EDA complexes which are not properly seated at the faces of the cube rather, it found a suitable position for better non-covalent hydrogen bonding interaction

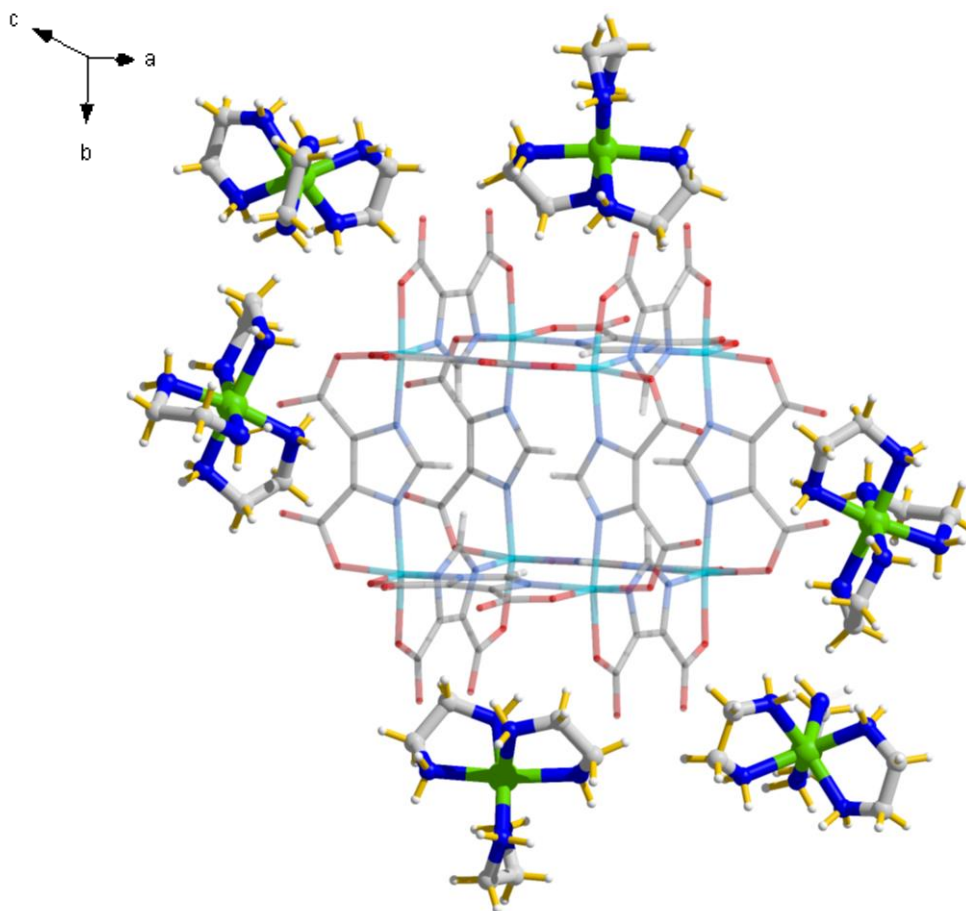


Figure 16. SCXRD study shows the Ga-MOC (wires/stick model) encircled by six Ni-EDA complexes (ball and stick model).

In the 1:10 ratio gel, the orientation of the Ga-MOC and the Ni-EDA complex is very much random in the gel state. Which actually readjust themselves into a proper directional fashion and results in the formation of crystals. Further, it was found to be a single MOC is connected with the other six MOC, where the Ni-EDA complex acted as the linker through the hydrogen bonding network. The non-covalent bond distances were found to be in the range of 2.37 Å to 2.45 Å suggesting a strong H-bonding interaction.³⁸ Fig.17 shows the connectivity of a single MOC with the four others in the X and Y directions (connectivity was shown in only two directions for clear visualisation whereas the same is also present in the 3rd direction). Strong hydrogen bonding interaction between the pendent oxygen groups of the Ga-MOC and the hydrogen from the ethylene diamine ligand helped to cross the thermodynamical energy barrier from the gel to crystal and started the ripening process. Therefore, the charged assisted hydrogen bonding (CAHB) not only played a vital role in the gelation but also drove the phase transformation process with the proper orientation of the Ga-MOC and the binder in a long-range order structure.

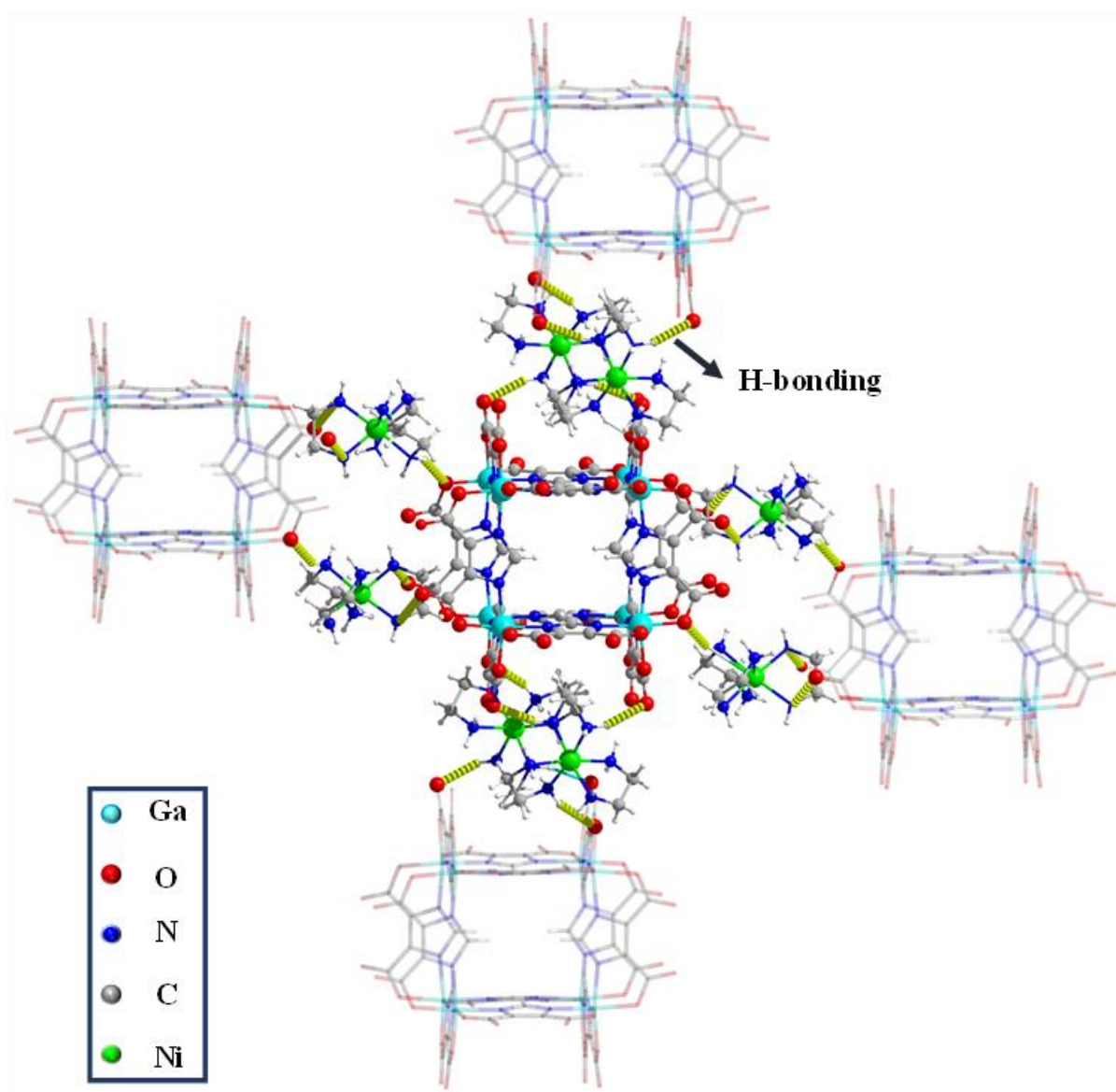


Figure 17. Interlinked hydrogen-bonded structure of Ga-MOC by the Ni-EDA complex linkers in two directions (3rd direction is not shown for visual clearance).

Next, to understand the structure of the crystalline state and the structure in the xerogel state, the PXRD pattern of the Ga-Ni-xerogel 1:10 (Ga-MOC:Ni-EDA complex) was compared with the simulated pattern obtained from the SCXRD (Fig. 18a). It shows a similar pattern for both, indicating a close structural similarity between the xerogel state and the single crystal state. However, the peak intensity of the xerogel was found to be less as compared to the SCXRD, suggesting the lower long-range ordering present in the case of the xerogel.

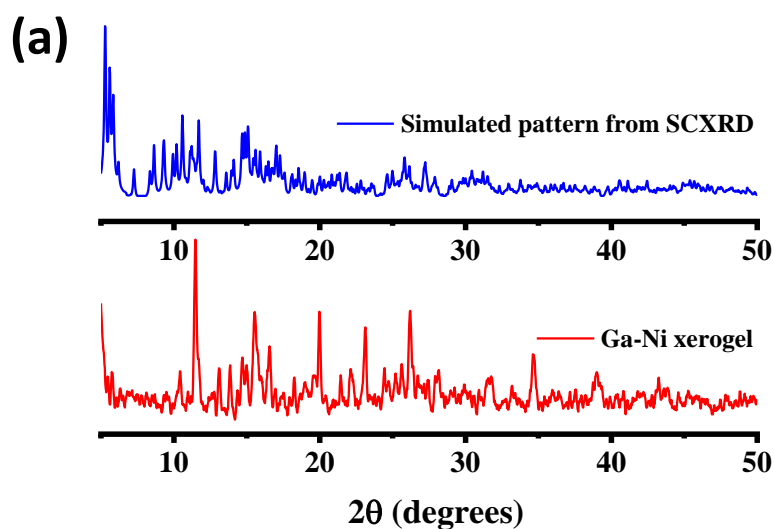


Figure 18. (a) X-ray diffraction pattern comparison of the simulated pattern obtained from the SCXRD and PXRD of the xerogel.

3.5 Summary:

In summary, we have explored a bicomponent gel to crystal transition process. Ga^{III} metal ions-based metal-organic cubes were used for the gelation. It is assembled in a proper arrangement with the help of a binder (Ni-EDA complex). The extended self-assembly was found to form instantaneously after the addition of Ni-EDA into the Ga-MOC solution. A strong charge-assisted hydrogen bond interaction holds the building block in a proper orientation. Over a period of time, a gel to crystal transition was found without any external stimuli. This transformation process ended up with the rupturing of the gel matrix, leading to a phase-separated solution and crystals. The binder concentration was varied from higher to lower value, where the gelation and crystallisation process was found to be highly affected. With the lower concentration of the binder, the mechanical strength of the gels was found to be lowering down. The crystallisation process was also dependent on the concentration ratio and a higher time required for crystal formation in the low Ni-EDA complex concentration. A detailed rheological and morphological analysis showed the origin of the concentration dependency of the gel to crystal transition process. The SCXRD data showed the arrangements of the molecular building blocks with the help of the hydrogen bonds.

3.6 References:

- 1 N. M. Sangeetha and U. Maitra, *Chem. Soc. Rev.*, 2005, **34**, 821–836.
- 2 S. Banerjee, R. K. Das and U. Maitra, *J. Mater. Chem.*, 2009, **19**, 6649–6687.
- 3 Q. Zhang, C. Y. Shi, D. H. Qu, Y. T. Long, B. L. Feringa and H. Tian, *Sci. Adv.*, 2018, **4**, 1–9.
- 4 J. Zheng, R. Fan, H. Wu, H. Yao, Y. Yan, J. Liu, L. Ran, Z. Sun, L. Yi, L. Dang, P. Gan, P. Zheng, T. Yang, Y. Zhang, T. Tang and Y. Wang, *Nat. Commun.*, 2019, **10**, 1604.
- 5 A. Legrand, G. A. Craig, M. Bonneau, S. Furukawa, S. Minami, K. Urayama and S. Furukawa, *Chem. Sci.*, 2019, **10**, 10833–10842.
- 6 Z. Wang, C. Villa Santos, A. Legrand, F. Haase, Y. Hara, K. Kanamori, T. Aoyama, K. Urayama, C. M. Doherty, G. J. Smales, B. R. Pauw, Y. J. Colón and S. Furukawa, *Chem. Sci.*, 2021, **12**, 12556–12563.
- 7 A. V. Zhukhovitskiy, M. Zhong, E. G. Keeler, V. K. Michaelis, J. E. P. Sun, M. J. A. Hore, D. J. Pochan, R. G. Griffin, A. P. Willard and J. A. Johnson, *Nat. Chem.*, 2016, **8**, 33–41.
- 8 M.-O. M. Piepenbrock, G. O. Lloyd, N. Clarke and J. W. Steed, *Chem. Rev.*, 2010, **110**, 1960–2004.
- 9 B. Mondal, D. Bairagi, N. Nandi, B. Hansda, K. S. Das, C. J. C. Edwards-Gayle, V. Castelletto, I. W. Hamley and A. Banerjee, *Langmuir*, 2020, **36**, 12942–12953.
- 10 C. Yan and D. J. Pochan, *Chem. Soc. Rev.*, 2010, **39**, 3528–3540.
- 11 T. Shao, N. Falcone and H. B. Kraatz, *ACS Omega*, 2020, **5**, 1312–1317.
- 12 A. Vidyasagar and K. M. Sureshan, *Angew. Chemie - Int. Ed.*, 2015, **54**, 12078–12082.
- 13 J. Liu, F. Xu, Z. Sun, Y. Pan, J. Tian, H. C. Lin and X. Li, *Soft Matter*, 2015, **12**, 141–148.
- 14 K. V. Rao, K. Jayaramulu, T. K. Maji and S. J. George, *Angew. Chemie - Int. Ed.*, 2010, **49**, 4218–4222.
- 15 S. Bhattacharjee and S. Bhattacharya, *Chem. Commun.*, 2015, **51**, 7019–7022.

- 16 S. Panja, A. Seddon and D. J. Adams, *Chem. Sci.*, 2021, **12**, 11197–11203.
- 17 P. Sutar, V. M. Suresh and T. K. Maji, *Chem. Commun.*, 2015, **51**, 9876–9879.
- 18 S. Sarkar, S. Dutta, S. Chakrabarti, P. Bairi and T. Pal, *ACS Appl. Mater. Interfaces*, 2014, **6**, 6308–6316.
- 19 S. D. Sahoo and E. Prasad, *Soft Matter*, 2020, **16**, 2075–2085.
- 20 B. Wang, J. Li, C. Hou, Q. Zhang, Y. Li and H. Wang, *ACS Appl. Mater. Interfaces*, 2020, **12**, 46005–46014.
- 21 S. Saha, E. M. Schön, C. Cativiela, D. Díaz Díaz and R. Banerjee, *Chem. - A Eur. J.*, 2013, **19**, 9562–9568.
- 22 R. Mohanrao, K. Hema and K. M. Sureshan, *Nat. Commun.*, 2020, **11**, 1–8.
- 23 D. Giuri, L. J. Marshall, C. Wilson, A. Seddon and D. J. Adams, *Soft Matter*, 2021, **17**, 7221–7226.
- 24 D. Giuri, L. J. Marshall, B. Dietrich, D. McDowall, L. Thomson, J. Y. Newton, C. Wilson, R. Schweins and D. J. Adams, *Chem. Sci.*, 2021, **12**, 9720–9725.
- 25 T. Yuan, Y. Xu, J. Fei, H. Xue, X. Li, C. Wang, G. Fytas and J. Li, *Angew. Chemie - Int. Ed.*, 2019, **58**, 11072–11077.
- 26 T. Guterman, M. Levin, S. Kolusheva, D. Levy, N. Noor, Y. Roichman and E. Gazit, *Angew. Chemie - Int. Ed.*, 2019, **58**, 15869–15875.
- 27 X. Liu, J. Fei, A. Wang, W. Cui, P. Zhu and J. Li, *Angew. Chemie*, 2017, **129**, 2704–2707.
- 28 J. R. Moffat and D. K. Smith, *Chem. Commun.*, 2008, **44**, 2248–2250.
- 29 W. Liyanage, W. W. Brennessel and B. L. Nilsson, *Langmuir*, 2015, **31**, 9933–9942.
- 30 E. R. Draper, K. L. Morris, M. A. Little, J. Raeburn, C. Colquhoun, E. R. Cross, T. O. McDonald, L. C. Serpell and D. J. Adams, *CrystEngComm*, 2015, **17**, 8047–8057.
- 31 H. Arakawa, K. Takeda, S. L. Higashi, A. Shibata, Y. Kitamura and M. Ikeda, *Polym. J.*, 2020, **52**, 923–930.
- 32 Y. Xu, C. Kang, Y. Chen, Z. Bian, X. Qiu, L. Gao and Q. Meng, *Chem. - A Eur. J.*,

- 2012, **18**, 16955–16961.
- 33 P. Zhu, X. Yan, Y. Su, Y. Yang and J. Li, *Chem. - A Eur. J.*, 2010, **16**, 3176–3183.
- 34 S. Satapathy, P. Prabakaran and E. Prasad, *Chem. - A Eur. J.*, 2018, **24**, 6217–6230.
- 35 P. Sutar, V. M. Suresh, K. Jayaramulu, A. Hazra and T. K. Maji, *Nat. Commun.*, 2018, **9**, 3587.
- 36 S. A. Reisinger, A. S. de Sousa, M. A. Fernandes, C. B. Perry, P. R. Varadwaj and H. M. Marques, *Inorg. Chem. Commun.*, 2010, **13**, 584–588.
- 37 I. Ramos Sasselli, P. J. Halling, R. V. Ulijn and T. Tuttle, *ACS Nano*, 2016, **10**, 2661–2668.
- 38 P. A. Sigala, E. A. Ruben, C. W. Liu, P. M. B. Piccoli, E. G. Hohenstein, T. J. Martínez, A. J. Schultz and D. Herschlag, *J. Am. Chem. Soc.*, 2015, **137**, 5730–5740.

Chapter 4

***Co-assembly of Ga-MOC and [Cu(en)₂(NO₃)₂]
towards soft materials: Gel to Crystal
transformation and electrocatalytic CO₂
reduction***

Abstract

A sustainable route for renewable energy storage by minimizing greenhouse gas is the electrochemical CO₂ reduction reaction (CO₂RR). However, the electrochemical CO₂RR possesses some limitations to achieve high efficiency. This chapter reports the supramolecular self-assembly of Gallium-based metal-organic cubes (Ga-MOCs) by linking each other with a binder making it a heterogeneous substance. The charge-assisted hydrogen bonding plays a crucial role in the gelation, and it was also observed that a spontaneous gel to crystal transformation is happening. The detailed morphological study showed the change of fibrillar structure to toroidal nanoring leads to crystallisation. A redox-active metal center (Cu²⁺) was incorporated into the binder to explore the electrochemical process. This multi-stimuli responsive gel was further used for the electrochemical CO₂ reduction process in water medium. The robust electrocatalyst showed an efficient conversion of CO₂ to CO with a faradaic efficiency of 92%, along with high partial current density. Furthermore, the durability of the xerogel catalyst was analysed by running the electrochemical process at a constant potential for 16 hours. This 3D entangled fibrous network of the heterogeneous hydrogel opened an avenue for developing new molecular electrocatalysts for energy applications.

4.1 Introduction:

Ordered and functional architectures can be established via supramolecular assembly based on various non-covalent interactions such as hydrogen bonding, π - π interactions, and van der Waals interactions.^{1,2} In particular, the controlled assembly of a single component promotes the formation of multiple phases with a rich diversity of physical and chemical properties. Utilizing low molecular weight gelators (LMWGs)³ or metal-organic polyhedras (MOPs)⁴⁻⁹ with a particular binder tends to form gel phase materials with typical fiber-like morphology. In fact, charge-assisted hydrogen bond (CAHB)-based non-covalent interaction produces versatile gel-based architectures with discrete properties. Owing to their dynamic and adaptive nature, the structure and function of supramolecular assemblies are tunable by slight variations of the molecular arrangements. This bottom-up approach has already found various applications in optoelectronics,^{10,11} biomedicine,^{12,13} electrical engineering,¹⁴ catalysis,¹⁵ chemical separation,^{16,17} and artificial photosynthesis,¹⁸ as it enables the formation of self-assemblies with desired properties. Yet, while allowing external stimulus-response, the gel permits altering the inherent supramolecular nature that may disrupt the gel matrix over time or under varying conditions. One such process is the spontaneous transition of gelator molecules into a crystalline phase. This gel-crystal transition happens due to thermodynamically more favorable crystalline formation than the kinetically trapped gel phase.¹⁹⁻²¹ The phase transition from gel to crystal is of great significance due to the evolution of advanced macroscopic functionalities.

The twin pressure of energy and environmental crisis has provoked pronounced attention to the recycling of CO₂.^{22,23} To carbon neutrality, using an electrochemical method to convert CO₂ into chemical fuel is a superior approach.^{24,25,26} This process deals with energetic electrons at the cathode to reduce CO₂ into value-added chemicals such as CO,^{27,28} formic acid (or formate),²⁹ methane,^{30,31} methanol,³² ethylene,^{33,34} ethanol,^{35,36} etc. The presence of two strong C=O bonds in the CO₂ molecule and the required bond rearrangement reflects the high overpotential and the low reaction efficiency, which remains a fundamental problem limiting practical applications.^{37,38} The first electron transfer to form CO₂^{•-} anion radical occurs at a high negative potential of -1.90 V (vs. SHE) without any electrocatalysts, making the reaction energetically uphill to take place. The multiple reaction pathways of CO₂ reduction limit the reaction selectivity.³⁹ CO₂ reduction can proceed via two, four, six, eight, twelve, or even more electron-transfer pathways, producing a large spectrum of possible reduction products. In addition, CO₂RR needs the participation of free protons or

proton donors (e.g., HCO_3^-) to disrupt the C-O double bond. It is thereby very trivial that hydrogen evolution reaction (HER) always exists as the competing side reaction, which is often kinetically favoured over CO_2RR , unfortunately. As a result, we urgently need to develop proper electrocatalysts to significantly expedite the reaction rate and steer the reaction selectivity toward the target product. The recent progress of electrocatalysts design for CO_2 reduction has gained considerable attention. Cu-based materials are the most sought-after catalyst for generating versatile products among the designed electrocatalysts.^{24,26,40-43} However, the utilisation of gel material is rarely explored towards electrochemical CO_2 reduction.

Our previous study demonstrated the employment of organic molecular binders led to the self-assembly of MOC.⁴⁴ Herein, Ga-based MOC was employed to produce three-dimensional supramolecular assembly through CAHB using Cu-ethylenediamine (en)-based complex as a binder. The entire phase transition phenomenon from solution to gel to crystal was monitored. The incorporation of a redox-active Cu center assisted in producing self-assembled structure and was also utilized as a heterogeneous catalyst. Hence, the three-dimensional architecture was exploited as heterogeneous electrocatalysts in CO_2RR . The Ga-Cu-MOC showed high selectivity towards CO formation from CO_2 with maximum Faradaic efficiency of 92% in water. The incorporation of the Cu-EDA complex assisted in producing 3D gel matrix and acted as a redox center to initiate the catalytic CO_2 reduction cycle. Interestingly, the gel matrix displayed superior long-term durability up to 16 h with a steady current. The reaction intermediate was identified using *in situ* FT-IR study. We anticipate that this approach to electrochemical CO_2 reduction based on a 3D-Ga-Cu-MOC hydrogel will also direct the development of other highly efficient 3D structured electrocatalysts in the near future.

4.2 Experimental section:

4.2.1 General: 4,5-Imidazolecarboxylic acid (H_3ImDC), Gallium nitrate hexahydrate [$Ga(NO_3)_3 \cdot 6H_2O$], Copper(II) Nitrate trihydrate ($Cu(NO_3)_2 \cdot 3H_2O$) were purchased from Sigma-Aldrich chemical Co. Ltd. All solvents and triethylamine (NEt_3) were obtained from Spectrochem Pvt. Ltd. (Mumbai, India).

4.2.2 Single-crystal X-ray diffraction: X-ray single-crystal structural data of 1 was collected on a Bruker Smart-CCD diffractometer equipped with a normal focus, 2.4 kW sealed tube X-ray source with graphite monochromated Mo- $K\alpha$ radiation ($\lambda = 0.71073 \text{ \AA}$) operating at 50 kV and 30 mA. The program SAINT was used for integration of diffraction profiles and absorption correction was made with SADABS program. All the structures were solved by SIR 92 and refined by full matrix least square method using SHELXL-97. All the nonhydrogen atoms were refined anisotropically and the hydrogen atoms were fixed by HFIX and placed in ideal positions. All calculations were carried out using SHELXL 97, PLATON and X-Seed Ver 4.

4.2.3 NMR Measurements: 1H NMR is recorded on a Bruker AV-400 spectrometer (400 MHz) with chemical shifts recorded as in parts per million (ppm) and all spectra were calibrated against DMSO ($\delta=2.6$ ppm). Solvent suppression was done for each of the sample for clear observation. For the sample preparation 50 μ l of D_2O , 50 μ l of DMSO with known concentration and 500 μ l of the sample was taken for the experiments.

4.2.4 Powder X-ray Diffraction Measurements: Powder X-ray diffraction (PXRD) patterns were collected in gel state coated on a glass plate and taken by a Rigaku Smartlab SE instrument using Cu $K\alpha$ radiation.

4.2.5 Thermal Stability Measurements: Thermogravimetric analysis (TGA) was carried out using Mettler Toledo TGA 850 instrument under inert atmosphere in the temperature range of 25-800°C at the heating rate of 5°C per min.

4.2.6 Morphological analysis: Atomic force microscopy (AFM) measurements were carried out with Asylum MFD-3D Origin to analyse the morphologies of the sample surface. Samples were prepared by making a dispersion of the xerogels in THF and coated on a silicon wafer by the drop-casting method. The Field Emission Scanning Electron Microscopic (FE-SEM) images were recorded on a Zeiss Gemini SEM 500. Samples were prepared by the

drop-casting method on a small piece of Si wafer and loaded in the machine without any gold sputtering.

4.2.7 Rheological analysis: The rheological study was done in Anton Paar Rheometer MCR 92 using plane plate geometry on a Peltier glass plate. The diameter of the plate was 60mm, and the measuring unit had a diameter of 25mm. The gel samples were placed on the plate and stress sweep experiment at a constant frequency at 25 °C, and frequency sweep measurements at constant stress in the linear viscoelastic range were carried out to get the storage or elastic modulus (G') and loss or viscous modulus (G'') values of the gel materials.

4.2.8 Zeta Potential Measurements: Zeta potential analysis was carried out in NanoZS (Malvern UK) employing a 532 nm laser.

4.2.9 ATR-IR Measurements: The ATR-IR experiment measurements were carried out using an FT-IR spectrophotometer (BRUKER, VORTEX 70B) in the region 4000–400 cm^{-1} .

4.2.10 Preparation of working electrode: A 1X0.5 cm^2 carbon paper was taken as the working electrode and connected with copper wire with the help of crocodile clip. Connection area were wrapped with Teflon tape to ensure no contact with the electrolyte during the electrolysis. The electrical connectivity was tested by the multimeter. For the ink preparation, 2 mg of the catalyst was taken along with 2 mg of Vulcan carbon to increase the conductivity. These two components were dispersed in 1 mL of a solution made up with 600 μL of isopropyl alcohol, 380 μL of mili Q water and 20 μL of Nafion. A homogeneous product was obtained after sonication for 30 min. 100 μL of the resulting mixture was coated evenly on both side of the carbon paper, and dried for 3 hours in ambient conditions. The same ink was coated on a glassy carbon electrode for the Linear Sweep Voltammetry (LSV) and Cyclic Voltammetry (CV) measurement.

4.2.11 Electrochemical setup: An undivided electrochemical cell equipped with three electrodes was used for LSV and CV testing. Glassy carbon electrode (area = 0.07065 cm^2) used as a working electrode, Ag/AgCl as the reference and Pt plate as the counter electrode in 0.2 M KHCO_3 solution saturated with CO_2 (or Ar) in LSV measurement. For the CV experiment non-aqueous solution was used to avoid the HER or other redox processes. 0.2 M tetrabutylammonium hexafluorophosphate solution in acetonitrile was used as the electrolyte for CV performance.

An air-tight H-type electrochemical cell was used for further experiment which consists of two compartments namely anodic and cathodic. These two parts were separated by a cation exchangeable Nafion membrane. Cathodic compartment was our main focus and comprised of the working electrode and Ag/AgCl as the reference electrode. In anodic compartment Pt plate was used as the counter electrode. 0.2 M KHCO₃ solution was used in both the chambers as the electrolyte and CO₂ was bubbled in both prior to the electrochemical experiment. A continuous CO₂ flow of 10 mL/min was employed to the cathodic chamber during the electrolysis and the outlet was connected with a gas bag as the gas collector where excess CO₂ itself act as a carrier gas. Gaseous products collected in gas bag were analysed by GCMS and after each chronoamperometry solution were collected for liquid analysis by NMR.

All the potential was converted from Ag/AgCl to RHE scale by following the equation.

$$E \text{ (RHE)} = E \text{ (Ag/AgCl)} + 0.197 + 0.059 \times \text{pH}$$

Faradaic Efficiency calculation:

According to the definition of Faradaic Efficiency

$$\text{FE}\% = \frac{Q_i}{Q_{total}}$$

Where Q_i represents the specific amount of charge required for a particular reduced product and Q_{total} represents the total charge passed during the process. Here i represents H₂, CO, HCOO⁻ and CH₃OH. For the gaseous products analysis done by the gas-chromatography and ideal gas law has been followed. FE for H₂, CO was calculated by following the equation.

$$\text{FE}\% = \frac{nFVvP^{\circ}}{RTi} \times 100\%$$

Where n is the number of electron required for the particular product (here it is 2), F is the Faradaic constant, V (vol%) is the volume concentration of the gas, v is the gas flow rate in mL/min at ambient condition, i is the steady state cell current in mA, $P^{\circ} = 1.01 \times 10^5$ Pa, $R = 8.314 \text{ J mol}^{-1} \text{ K}^{-1}$, $T = 273.15 \text{ K}$ and $F = 96485 \text{ C mol}^{-1}$

For the measurement of the liquid products ^1H nuclear magnetic resonance was used in quantitative way. DMSO and phenol was used as the internal standard with known concentration. Peak areas were quantified for both the product and standard to determine the amount of the products. The relative peak intensity ratio was calculated according to this formula.

$$\text{Relative peak area ratio} = \frac{\text{singlet peak area at 3.23 ppm (methanol)}}{\text{singlet peak area at 2.6 ppm (DMSO)}}$$

Faradaic efficiency for all the liquid products were calculated as follows,

$$\text{FE}\% = \frac{\alpha n F}{Q} \times 100\%$$

Where α is the number of electron required for that particular product. n is the amount of the liquid product in mol, calculated from the relative peak area ratio. F is the faradaic constant and Q is the total charge passed during the full run.

4.2.12 Chronoamperometric experiment: To calculate the faradaic efficiency of all the products and to check the durability of the catalyst, chronoamperometric analysis was carried out at different potential starting from 0.68 V to 1.18 V (vs RHE) for 7200 s each. Both the compartments of the electrochemical cell were bubbled with CO_2 for 30 min prior to the experiment and a constant CO_2 flow rate of 10 mL/min was maintained throughout the experiment. We have also changed the KHCO_3 solution before starting at each potential and collected the electrolyte for the quantification of the liquid product through ^1H NMR analysis.

4.2.13 ^1H -Nuclear Magnetic resonance analysis: For the quantification of the liquid products such as formate and methanol obtained during the electrolytic process performed for 2 hours, ^1H NMR studies was used in a quantitative manner. NMR for the liquid samples were recorded in Bruker Ultrashield Plus 400 (operated at 400 MHz) using DMSO and phenol mixture as the internal standard. Concentration of the product was determined from the relative peak area ratio of the product versus internal standard with known concentration. For the sample preparation, 600 μL of the electrolyte solution was taken after catalysis along with 50 μL of DMSO and phenol mixture having the known concentration of 4 mM and 20 mM respectively and 50 μL of D_2O .

4.2.14 Gas-Chromatography analysis: All the gaseous products obtained during the electrocatalysis process were collected in a multilayer gas sampling bag. The gases were identified and quantified by the Gas Chromatography Mass Spectrometry analysis. Helium

was used as the carrier gas and calibration was done with H₂ and CO. After completion of chronoamperometric study at each potential for 2 hours gas sample was collected by the Hamilton syringe and injected into the sampling loop of the GCMS analyser. CO was analysed by the flame ionized detector with a methanizer and for H₂ thermal conductivity detector was used.

4.2.15 Turn Over Frequency calculation: Based on the two-electron pathway for the production of CO turn over frequency was calculated by following this equation.

$$\text{TOF} = \frac{\text{Turnover number for CO production / geometrical area}}{\text{Number of active sites / geometrical area}}$$

For the calculation of turnover number for CO production the below equation was followed.

$$\text{TON} = \frac{J \times t \times FE \text{ for CO}}{2F} \times N_A$$

Where J is the current density and time was denoted by t . N_A is the Avogadro constant to cancel out the per mole term in Faradaic constant designated by F and the 2 in the denominator was taken because production of CO is a two-electron process. Turnover number was calculated at the potential of 0.98 V vs RHE because of the highest faradaic efficiency obtained for CO.

Number of active per cm² was calculated by the following equation.

$$N = N_A \times \frac{\text{weight of copper on the electrode}}{\text{Molar weight of Copper}}$$

4.2.16 *In situ* diffuse reflectance FT-IR measurements: The *in situ* FT-IR measurements were carried out by FT-IR spectrophotometer (BRUKER, Pat. US, 034, 944) within a electrocatalytic chamber. The catalytic ink was coated on a graphite electrode and runed it as working electrode with Pt spring as counter electrode and Ag/AgCl as the reference electrode. Next, the air inside the cell was removed using vacuum and then 99.99 % CO₂ gas along with water vapour was passed for 15 minutes into the photoreactor. The IR source was focused on the working electrode surface to observed the changes in absorbance. *In situ* FT-IR signal was collected through MCT detector as a function of time with applied potential.

4.3 Synthesis:

4.3.1 Synthesis of Ga(III) Metal-Organic Cube: The synthesis of Ga(III) Metal-Organic Cube was previously reported by our group; we have followed the same solvothermal method. 4, 5-Imidazoledicarboxylic acid (4, 5-ImDC) (0.5 mmol, 78 mg), Ga(NO₃)₃.H₂O (0.5 mmol, 128 mg), and 10 ml DMF were mixed in a 20 ml Teflon container and stirred for 30 minutes at room temperature. 15 μl triethylamine was added to the reaction mixture and stirred for an additional 30 minutes. After that, the Teflon container was kept inside a stainless steel autoclave, heated at 120 °C for 24 hours. Next, the autoclave was slowly cooled down to room temperature, and the white product was centrifuged with washing repeatedly by methanol and dried in air. PXRD pattern matches with the simulated one (Fig 1a). FTIR data (cm⁻¹) (Fig 1b): 3447 (b), 3086 (m), 2775 (m), 1676 (s), 1473 (s), 1363 (s), 1100 (s), 857 (m), 660 (m), 550 (m) is well-matched with the literature. Mass peak (Fig 1c) in MALDI at 821.393 m/z for the unit [(Ga₈(ImDC)₁₂)(7H⁺)(2Na⁺)(H₂O)]³⁻ also indicates the successful synthesis of Ga-MOC as per the earlier report.

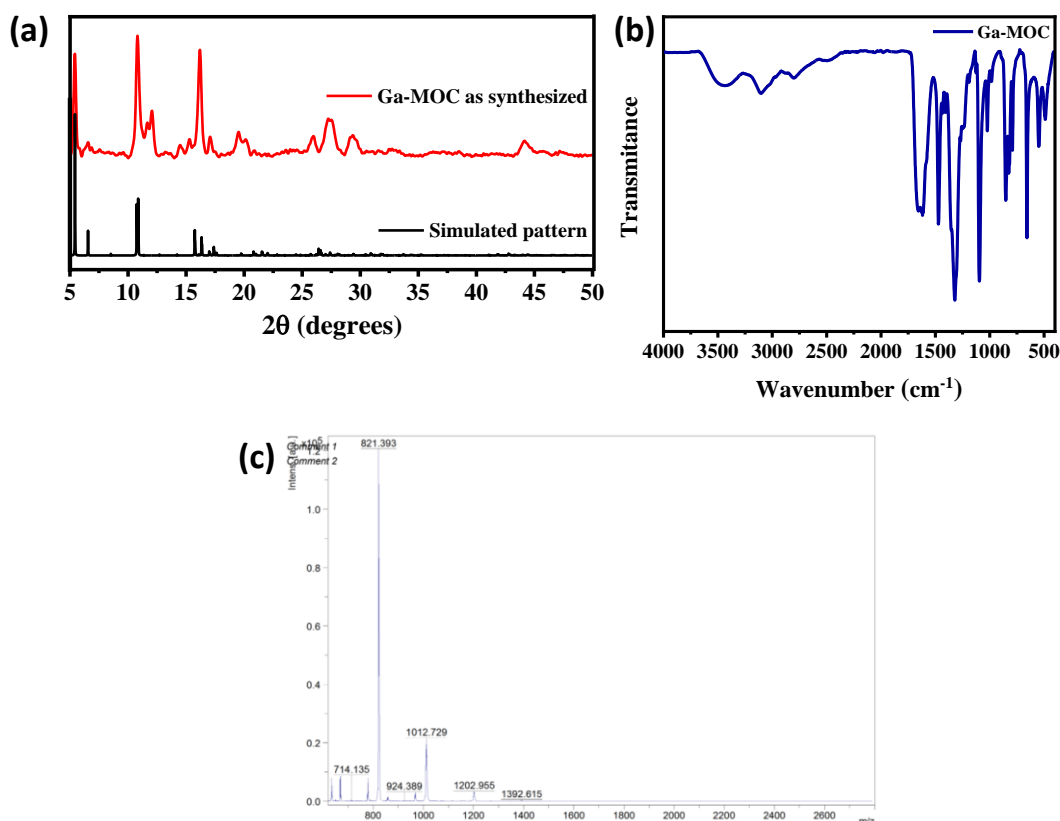


Figure 1. (a) PXRD pattern of Ga-MOC simulated (black) and as synthesised (red). Peaks indicate the phase purity. (b) ATR spectra of as synthesised Ga-MOC. (c) Negative mode acquisition of MALDI of the aqueous solution of Ga-MOC, peak at m/z 821.393 ($z=3-$) corresponding to the moiety [(Ga₈(ImDC)₁₂)(7H⁺)(2Na⁺)(H₂O)]³⁻.

4.3.2 Synthesis of bis(ethylenediamine)copper(II) nitrate (Cu-EDA complex): We have followed the reported procedure for the synthesis of the Cu-EDA complex.⁴⁵ $\text{Cu}(\text{NO}_3)_2 \cdot 6\text{H}_2\text{O}$ (500 mg, 1.7 mmol) was dissolved into 10 mL of ethanol, and 2 equivalents of ethylenediamine (3.4 mmol) were added dropwise into it under stirring condition over 10 minutes. Violet colour precipitate formed, filtered under suction, and washed with ethanol. Powder X-ray diffraction (Fig. 2a) was collected, and it is well-matched with the simulated pattern.

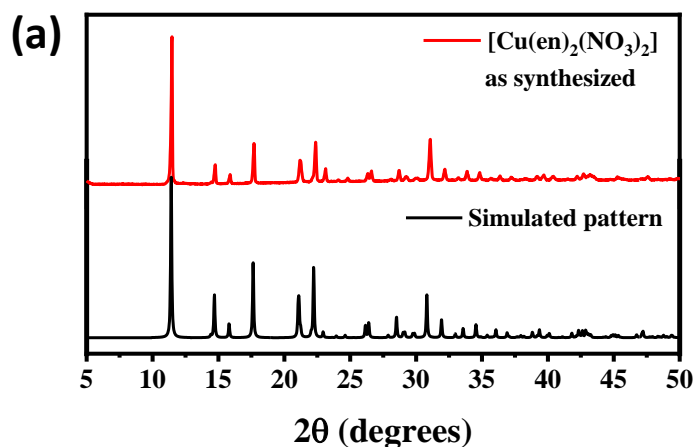


Figure 2. (a) PXRD pattern of Cu-EDA complex simulated (black) as synthesised (red). Exact matching of peaks indicates the successful synthesis.

4.3.3 Preparation of Ga-Cu hydrogel: Due to the high negative charges (with general formula = $[\text{M}_a\text{L}_b]^{n-}$) on each of the metal-organic cubes, these are very much water-soluble in nature. This fact was utilized to use an aqueous solution of both the Ga-MOC and Cu-EDA complex for the gelation process. Solutions were made by dissolving 17 mg of Ga-MOC in 0.5 mL and 15 mg of Cu-EDA complex in 0.5 mL of water. Instantaneous gelation took place just after the addition of binder Cu-EDA complex solution in Ga-MOC, and the gel colour was appeared to be violet. The formation of gel was confirmed by the inversion test method and rheology experiment. Xerogel was prepared by the air-drying method under ambient conditions. The dried obtained xerogel was further used as a catalyst for electrocatalytic CO_2 Reduction Reaction.

3.4 Results and discussion:

The surface negative charges of Ga-MOC arises from the free carboxylate group of 4,5-ImDC, which makes it water-soluble. As indicated by the mass analysis, these MOCs were also stable in the water medium. The peripheral carboxylate oxygens were not only made the cubes polar but also it plays an important role in the gelation. After the addition of the Cu-EDA complex solution to the aqueous solution of the Ga-MOC results in gel formation. Here the negatively charged oxygens help to form the charge-assisted hydrogen bonding with the binders (Cu-EDA complex) and arrange the cubes into a self-assembled structure. The MOCs were arranged in a well-oriented fashion through the CAHB interaction and led to the fibrillar structure (Fig-3).

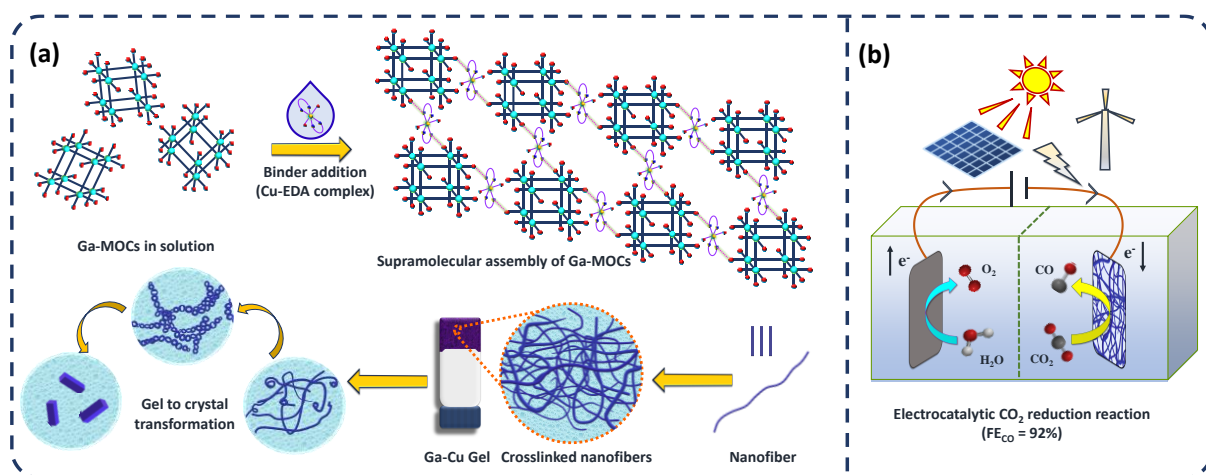


Figure 3. Schematic illustration of the self-assembled structure of Ga-MOC with Cu-EDA complex towards electrocatalytic CO₂ reduction. (a) Formation of the Cu-EDA complex binder-driven hydrogel of the Ga-MOC and the gel to crystal transformation process. (b) Electrocatalytic CO₂ reduction process with hydrogel as the catalyst.

Gelation was confirmed by the invert vial test, and the Ga-Cu hydrogel was found to be stable when the vial was inverted upside down. Furthermore, the viscoelastic nature of the hydrogel was revealed by rheological experiments. Amplitude sweep measurements were carried out by varying shear strain and angular frequency, which indicates the higher value of storage modulus (G') than that of loss modulus (G'') under the viscoelastic region (Fig 4a and 4b). As shown in fig 5a, both the modulus displayed a linear nature under the lower shear strain region, and also a crossover point appeared at a shear strain of 5%, representing the phase change from gel to sol. Whereas in the case of angular frequency variation at a constant shear strain of 0.5% depicted a long-term storage behaviour under a wide range starting from 0.1 rad/s to 100 rad/s. This linearity indicates the non-dependency of the shear modulus on

the Angular frequency. A higher value of G' than G'' suggests a solid-like structure with a stable network of forces. Both liquid and solid-like behaviour of the gel can be confirmed by the value of loss factor ($\tan \delta$). For a perfectly viscous material (liquid), the phase difference (δ) between stress and strain is 90° , but in the case of an ideally elastic material (solid), this is calculated to be 0° . Now, if any material has the value of loss factor ($\tan \delta$) in between 0 to 1 can be described as a viscoelastic material that experiences both liquid and solid-like properties. Ga-Cu hydrogel also shows the same under the lower shear strain region. PXRD pattern of xerogel indicates the crystalline ordered structure constructed by Ga-MOC and Cu-EDA complex binder (Fig. 5a). Bragg's reflections' similarity with Ga-MOC indicates MOC is intact in the gel.

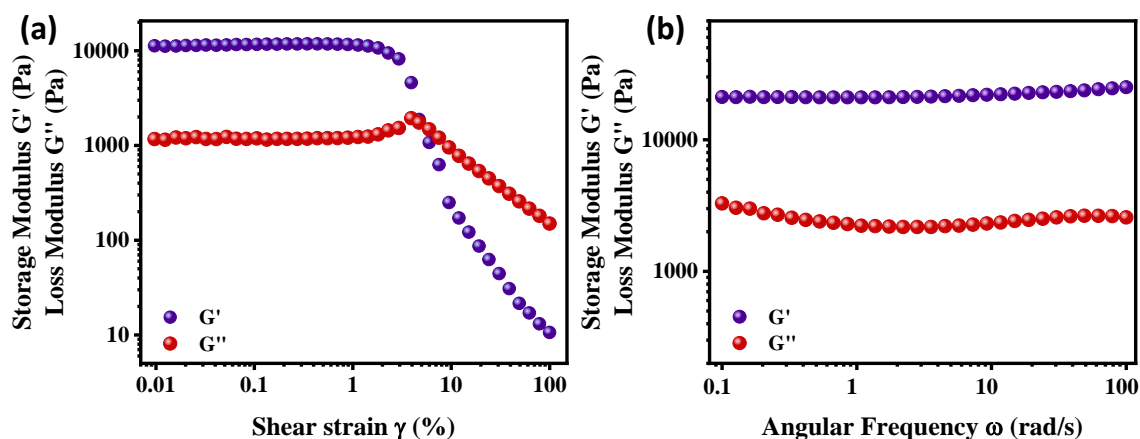


Figure 4. (a) Amplitude sweep measurement of Ga-Cu gel. Storage modulus (G') (blue circle) has a higher value than loss modulus (G'') (red circle), indicating the viscoelastic nature. (b) Oscillatory frequency sweep measurement of Ga-Cu gel where the shear modulus is independent on angular frequency.

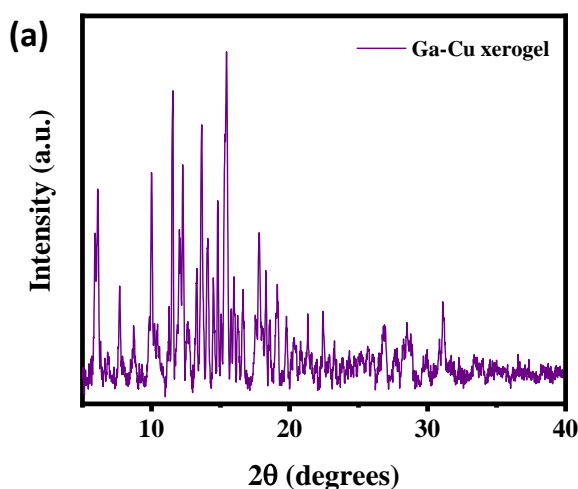


Figure 5. (a) PXRD pattern of Ga-Cu xerogel.

Next, the morphology of the xerogel was investigated by field emission scanning electron microscope (FESEM). Ga-Cu xerogel shows a highly interconnected fibrous nanostructure under the electron microscope. It was further confirmed by the atomic force microscopy (AFM) analysis. A thoroughly cross-linked micrometer-long fibers were also found in AFM. Height of the fibers was calculated to be 10-15 nm, and the width was calculated to be in the range of 300-400 nm (Fig. 6 a-c).

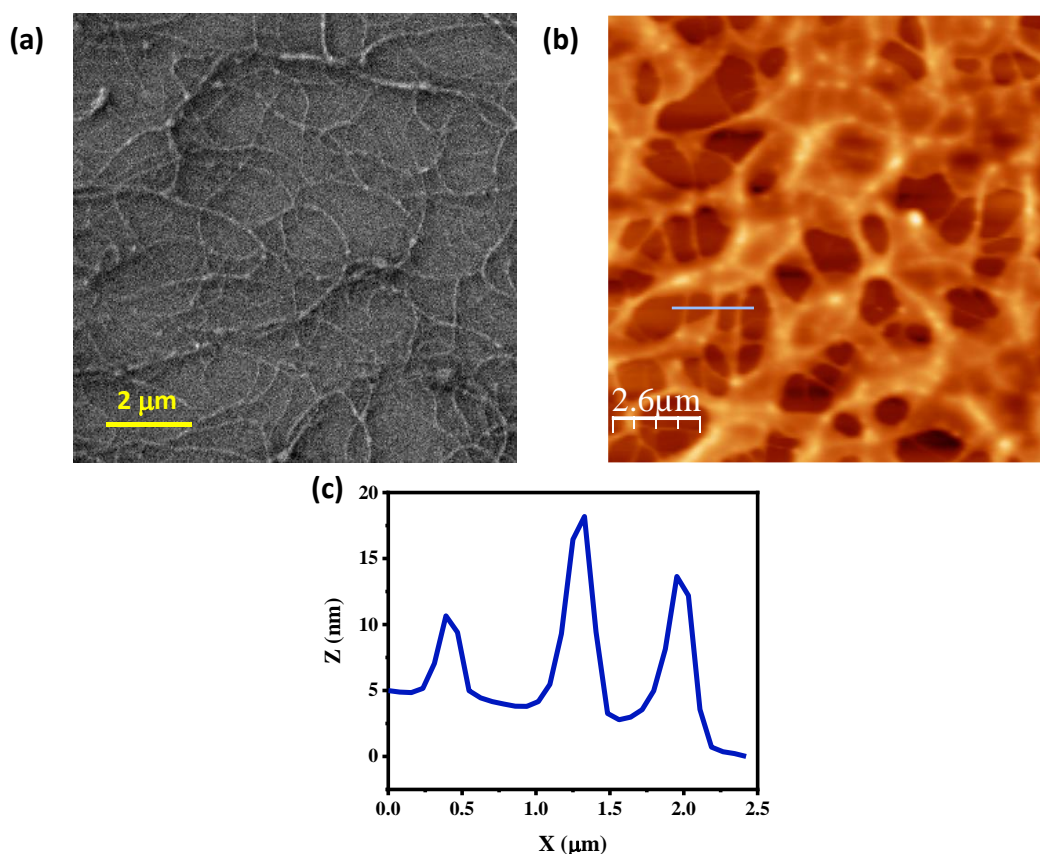


Figure 6. (a) FESEM images of Ga-Cu xerogel shows interconnected fibrous structures. (b) 2D AFM image of the Ga-Cu xerogel also confirms the fibrillar morphology. (c) Height profile diagram of the fibers obtained in AFM.

This Ga-Cu hydrogel was also responsive to different external stimuli and exhibited excellent reversibility also (Fig. 7). It was transformed into sol just after shaking, which again returned into its gel phase upon resting. This behaviour indicates the self-assembly of the Ga-MOC with the help of Cu-EDA complex binder, made up of weak H-bonding, which can be damaged by a little perturbation, but it regains its original phase upon standing. Such kind of dynamic behaviour suggests the thixotropic nature of Ga-Cu hydrogel. The aforementioned self-assembly showed a transition from gel to sol when it was exposed to different pH. The pH of the as-prepared gel was measured to be 6.8, but upon the addition of 1 (M) HCl, a spontaneous transformation occurred into the sol state. At lower pH (pH = 4.72), the

carboxylate oxygen gets protonated, which destroys the charge-assisted hydrogen bonding, leading to demolish of the self-assembled gel structure. This transformation was found to be reversible upon the addition of basic solution (1 M NaOH), and upon resting for half an hour, it again comes into the gel phase with a pH value of 6.72.

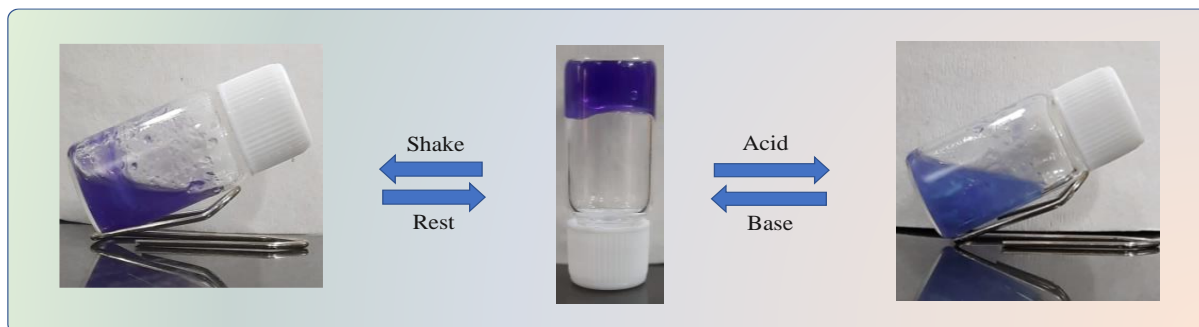


Figure 7. Stimuli-responsive behaviour of the Ga-Cu gel. Upon shaking, it turns into sol and again comes back to gel. With addition of 1N HCl gel (pH = 6.8) turns to sol (pH = 4.72) which again transform into gel (pH = 6.72) with addition of 1 NaOH.

Next, to check the stability of the gel, the Ga-Cu hydrogel was kept in undisturbed condition for several days. Here we observed an interesting phenomenon with this hydrogel. A phase transformation from gel to crystal was happening spontaneously over a period of 17 days. This kind of evolution process is well known to be triggered by different external stimuli such as agitation, cryogenic treatment, irradiation, pH change, and change in polarity of the solvent. Herein, a spontaneous transition was observed without any disturbance, and crystals with cubic geometrical shapes were found under the optical microscope (Fig. 8a-b). The conversion was initially observed by the visible weakening of the gel matrix, and an increase in the degree of crystallisation was found over one month.

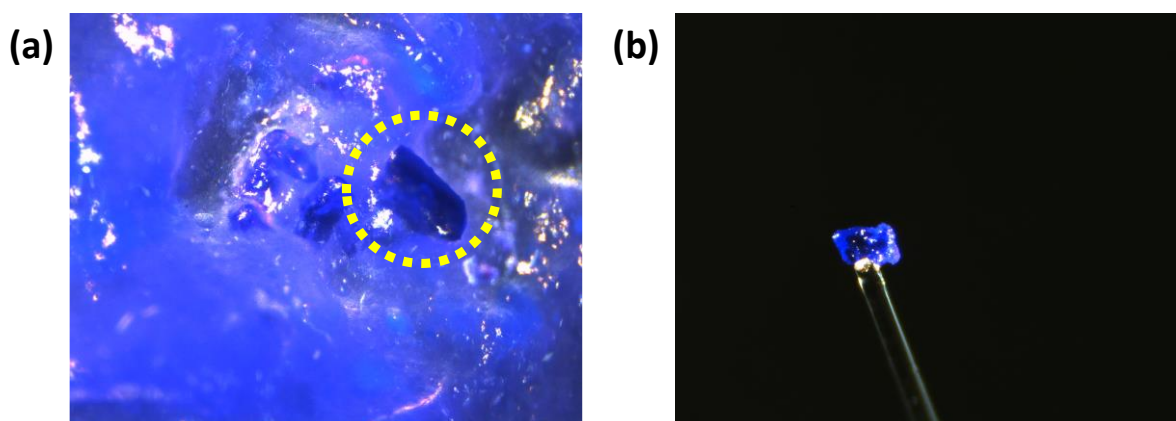


Figure 8. (a) Microscopic image shows the formation of crystal from the GA-Cu hydrogel. (b) Block-shaped microcrystal mounted on a glass wire.

This whole event leads to the loss of hydrogel matrix integrity and ends up with the two separated phases, sol and crystals. Presumably, a rise in fibrillar connectivity conducts the crystallisation process, where uniformly distributed self-assembled fibers get converted into an insoluble well-ordered crystals. To understand the mechanism of the phase transformation process, we have investigated the hydrogel morphology by AFM with the time scale (Fig 9a). For the first day, the cross-linked fibrous morphology was obtained; after five days also, the fibers remained stable, as evident from the AFM analysis. After ten days, we saw a change in morphology under the AFM, and the fibers were started to transform into microrings. This transformation started from the fiber's end, and after fifteen days, all the fibers were fully transformed into microrings. This process concentrates the fibers in a particular fashion, leading to the facile crystallisation process.

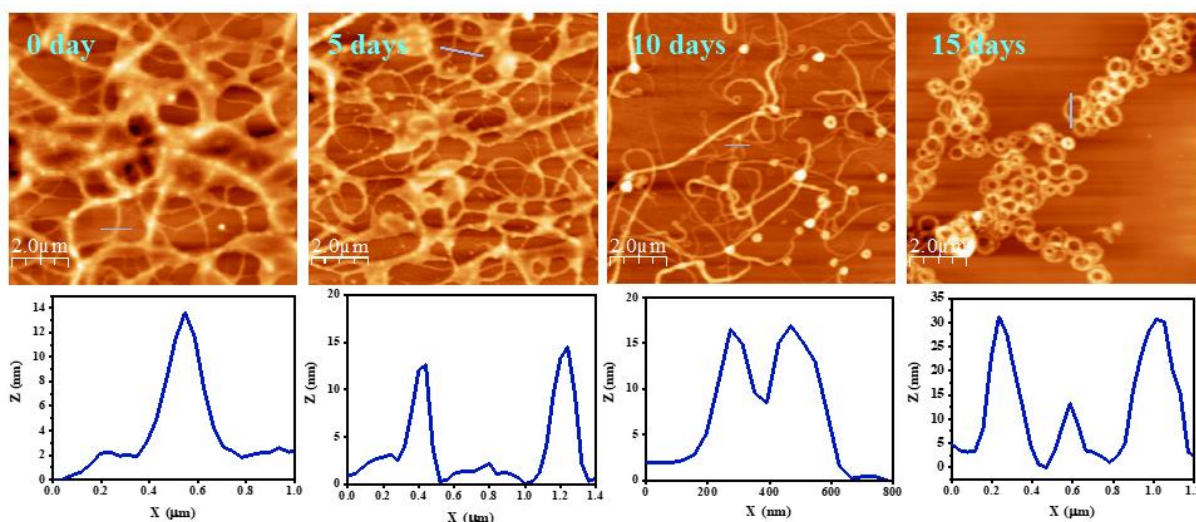


Figure 9. (a) A time scale AFM images of the fibrillar structure of Ga-Cu hydrogel. A transformation from nanofiber to microrings was observed after 15 days of the standing of the gel.

There was a competition between the two components of the gel toward solvation and intermolecular interaction, which led to the formation of a gel. But as the gel is nothing but a thermodynamically metastable trap state for any assembled structure, therefore, it always tries to go towards a more stable, lower energetic structure. In this present study, this spontaneous transition reveals the potential of charge-assisted hydrogen bonding to build the order structure and capability to cross the thermodynamic energy barrier toward crystallisation. Next, we took out a good quality block-shaped crystal from the gel and mounted it on a glass wire for the Single Crystal X-Ray Diffraction (SCXRD) study. The details of the Ga-Cu crystal structure obtained after SCXRD were discussed below.

4.4.1 Single Crystal X-ray Diffraction Analysis (SCXRD):

The single-crystal x-ray diffraction analysis of the Ga-MOC-Cu was examined to determine the packing of Ga-MOC and Cu-EDA complex units in the crystal phase. The obtained block-shaped crystals were blue colored with $280\ \mu\text{m}\times 189\ \mu\text{m}\times 128\ \mu\text{m}$ dimensions. The SCXRD analysis displays the monoclinic $P2_1/n$ space group. Detailed cell parameters are given in Table 1. Each unit cell consists of two formula units of Ga-MOC and Cu complexes, with one unit of Ga-MOC in the center and partial contribution from eight units of Ga-MOCs at the corner. Each Ga-MOC unit is encircled by six Cu-EDA complexes leading to charge neutralisation between the anionic MOC and cationic metal complex, supported by zeta potential calculations (Fig. 14a-b). Based on the crystal structure, the spatial arrangement of adjacent Ga-MOC units is shown in (Fig. 10). Two adjacent Ga-MOC units are held together by the non-covalent H-bonding and dipole-dipole interactions.

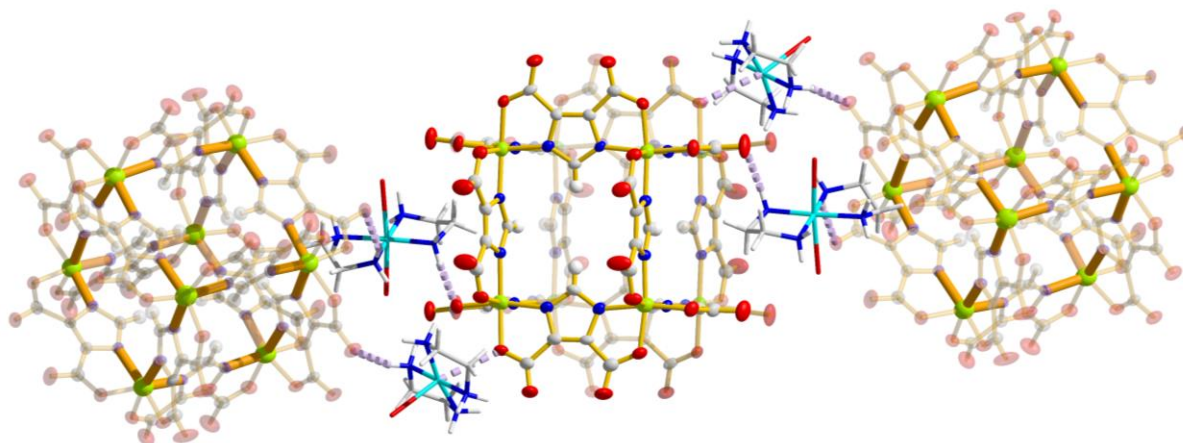


Figure 10. Ellipsoid model of Ga-MOC-Cu based on the crystal structure showing the interlinked gelator Ga-MOC units by Cu-EDA binders

Fig 11 shows two adjacent Ga-MOC units held together by two Cu-EDA complexes via two different types of interactions (violet and green dotted line). The gel state generally consists of a random array of Ga-MOC gelator units suspended in a pool of solvent and Cu-EDA complex binder molecules. We have observed gel to crystal phase transformation, which occurs due to the displacement of several solvent molecules resulting in the compact arrangement of gelator and binder units. In our case, two kinds of non-bonding interactions play a significant role in directing the phase transformation.

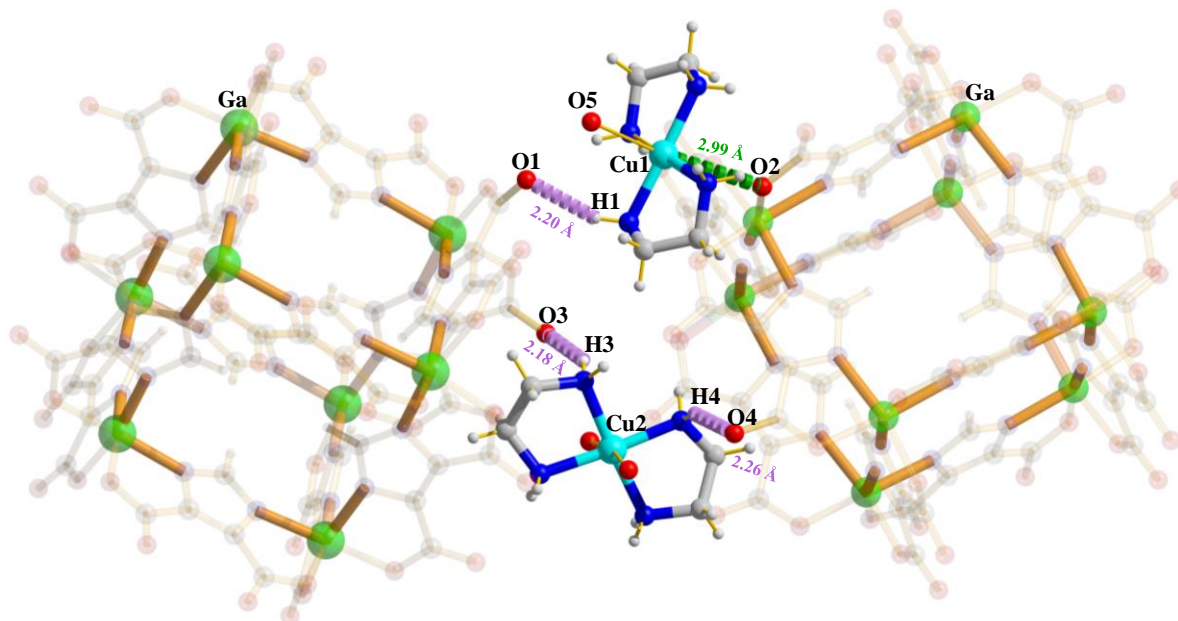


Figure 11. High-resolution X-ray diffraction single crystal structure of Ga-MOC-Cu showing the non-covalent interaction between two Ga-MOC and the two Cu-EDA binder units, with appropriate experimental distances for the respective sites. (Violet dashed lines: H-bonding interactions, Green dashed lines: dipole-dipole interaction) Note: most of the atoms in the Ga-MOC unit have been made transparent for proper visualisation of the role of Cu-EDA binder units.

Firstly, H-bonding plays a vital role not only in the self-assembly of gelator molecules during gel formation but also acts as an invisible string to pull together the Ga-MOC units until a compact packing is achieved during the phase transformation. Secondly, the dipole-dipole interaction between the metal center in the Cu-EDA complex (5 coordinated) and the Oxygen atom in the Ga-MOC unit, i.e., Cu1 and O2. In the gel state, the coordination number of each Cu-EDA complex is expected to be 6, including four coordinating sites from two EDA ligands and two axially coordinated H₂O ligands. During phase transformation, one of the axially coordinated H₂O molecule dissociates, and the Cu – center shifts towards the Ga-MOC unit, keeping the Oxygen atom (O2) from the gelator unit axially inclined towards the vacant 6th coordination site. The distance measured between Cu1 and O2 is 2.99 Å, which is longer than the other axial Cu1-O5 bond length of 2.508 Å. Both these non-covalent interactions stabilize the gelator and binder in the unit cell.

Parameters	Ga-Cu
Empirical formula	C ₉₀ H ₁₀₈ Cu ₆ Ga ₈ N ₅₉ O ₅₈
Formula weight	3883.35
Crystal system	Monoclinic
Space group	P2 ₁ /n
a, Angstrom	18.3277(17)
b, Angstrom	23.2153(19)
c, Angstrom	18.9579(19)
β, deg	96.950(3)
V, Angstrom ³	8007.0(13)
Z	2
T, K	293
μ, mm ⁻¹	2.209
D _{calcd} , g/cm ³	1.692
F (000)	4090
Reflections [I>2σ(I)]	10983
Unique reflections	15197
Total reflections	108809
R _{int}	0.110
GOF on F ²	1.07
R ₁ [I>2σ(I)] ^a	0.0765
R _w [all data] ^b	0.2237
Δρ max/min [e Angstrom ⁻³]	3.80, -1.53

$$^a R_1 = \frac{\sum ||F_o| - |F_c||}{\sum |F_o|}; \quad ^b R_w = \left[\frac{\sum \{w(F_o^2 - F_c^2)^2\}}{\sum \{w(F_o^2)^2\}} \right]^{1/2}$$

Table 1. Cell parameters and structure refinement parameters of Ga-Cu

Next, Attenuated Transmission Reflectance (ATR) study was carried out for Ga-MOC, Cu-EDA complex, and Ga-Cu xerogel (Fig. 12a). Peaks at 3158 cm^{-1} , 3248 cm^{-1} , 3271 cm^{-1} for the Cu-EDA complex indicated the N-H stretching frequency of ethylenediamine. Stretching frequency for C-H was observed at 2886 cm^{-1} , 2954 cm^{-1} . The peak at 1604 cm^{-1} can be attributed to N-H bending vibration.

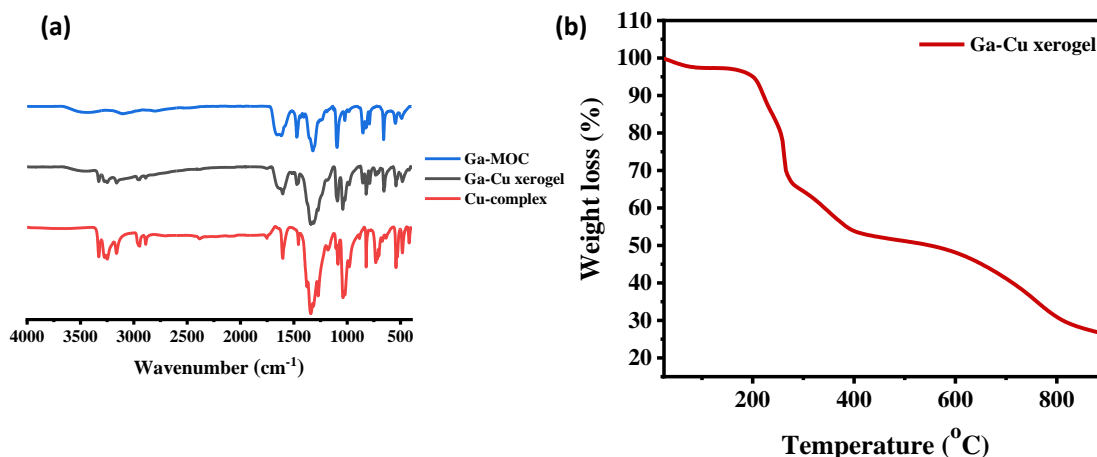


Figure 12. (a) ATR spectra of Ga-MOC (blue), Ga-Cu xerogel (black), Cu-EDA complex (red). 13. (b) TGA curve of Ga-Cu xerogel shows stability up to 200°C .

O-H stretching and bending peaks were observed at 3331 cm^{-1} and 1459 cm^{-1} , respectively, indicating the presence of water in the complex. Cu-N bond stretching frequency also can be found at 480 cm^{-1} . A weak band can be observed at 3100 cm^{-1} for Ga-MOC spectra, indicating the aromatic C-H stretching frequency. Peaks at 1658 cm^{-1} and 1323 cm^{-1} can be designated for C=O and C-N stretching. Interestingly, all peaks for Ga-MOC and Cu-EDA complex can be found intact in Ga-Cu xerogel, implying the structural integrity of both components in the xerogel state. The decomposition temperature curve of TGA reveals the stability of the xerogel at higher temperatures, and it is quite stable up to 200°C (Fig. 12b). A primary weight loss was started from 200°C due to the loss of the guest molecules inside the Ga-MOC, water, and DMF. Weight loss at 260°C corresponds to the breaking of the Cu^{II} -complex, oxidation of the ethylenediamine takes place at this temperature. Third, weight loss at 400°C can be attributed to the breaking of the MOC and oxidation of the imidazolecarboxylate unit. Next, zeta potential measurement has been carried out to understand the surface binding of the Cu-EDA complex to the Ga-MOC having carboxylate groups at its periphery (Fig. 13a-b). For only Ga-MOC, it showed a zeta potential of -34 mV , which indicates the negatively charged surface of the cubes. However, a shift of the zeta potential was observed upon the subsequent addition of the binder. This result again confirms the tie-up between the two charged species by the charge-assisted hydrogen bonding.

Interestingly it was found that the zeta potential goes near to zero value (0.33mV) with the addition of six equivalent of Cu-EDA complex, also corroborating the neutralisation of negative charges on each MOC ($[(\text{Ga}_8(\text{ImDC})_{12})]^{12-}$) by the Cu-EDA complex having positive charges $\{[\text{Cu}(\text{en})_2]^{2+}\}$. With the addition of more than six equivalent of Cu-EDA complex binder solution to the aliquot, two peaks appeared near to zero and on the positive side. This reveals the binder accumulation on the MOC surface as the zeta potential indicates the positive values with increasing the concentration of Cu-EDA complex binder along with some neutral units. The CO_2 affinity of the Ga-Cu xerogel was determined by CO_2 adsorption study (Fig. 14a). The experiment was performed at room temperature (298 K) after activating the sample at 120 °C under vacuum overnight. It showed a CO_2 uptake of 6.37 mL g^{-1} at a relative pressure of 1, also corroborating the intake and easy diffusion of CO_2 through the fibrous network of the xerogel. It also suggests the binding probability of CO_2 to the metal center, which fulfills the primary step for the CO_2 reduction reaction and indicates the capability of this heterogeneous catalyst toward the reduction process.

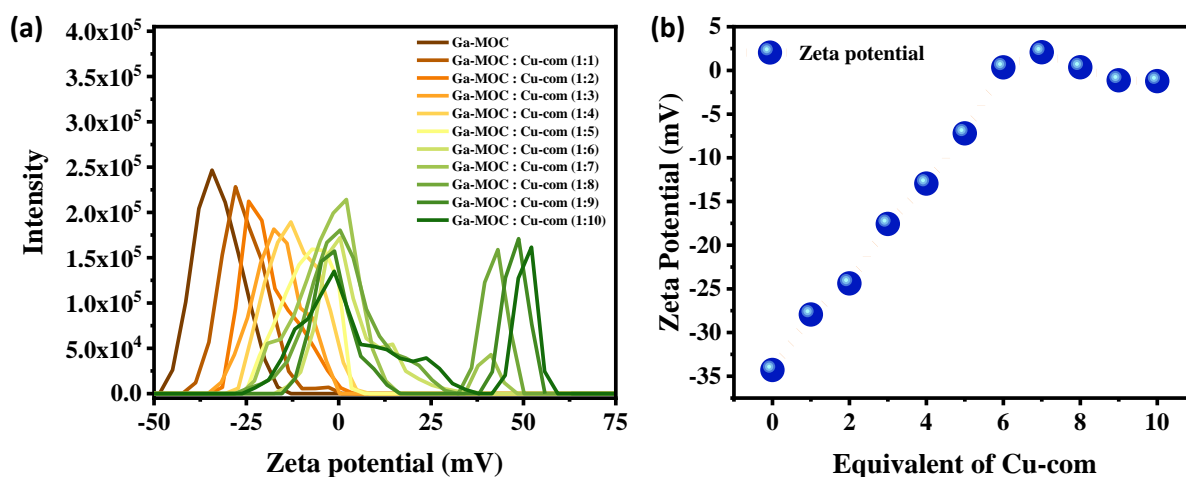


Figure 13. (a) A titration curve of zeta potential where Ga-MOC (10^{-4} M) was taken as the aliquot and Cu-EDA complex (10^{-4} M) was added as titrant. (b) Negative zeta potential curve with the addition of Cu-EDA complex, where the negative value lowers down with the addition of Cu-EDA complex.

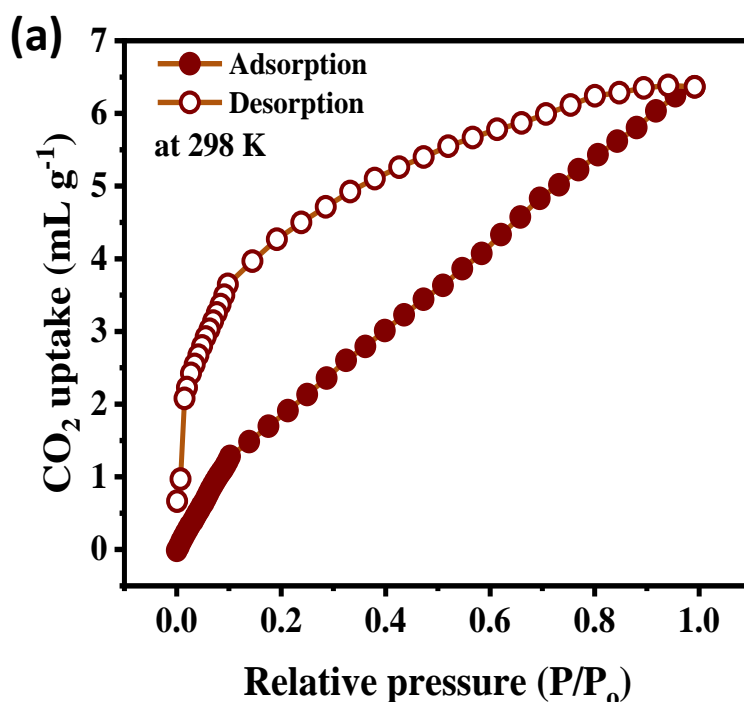


Figure 14. (a) CO₂ adsorption curve of Ga-Cu xerogel at 298 K where filled circles indicate the adsorption and empty circles indicate the desorption curve.

4.5 Electrochemical CO₂ reduction:

In order to evaluate the catalytic potential of as-prepared Ga-Cu xerogel, the electrochemical CO₂ reduction process was performed in a gas-tight H-cell having two compartments separated by a proton exchange membrane (Nafion 117). A three-electrode system was implemented for the electrochemical process, where Ag/AgCl was used as a reference electrode, and Pt (1x0.5 cm²) plate was used as the counter electrode. To avoid the unwanted oxidation process of the CO₂-reduced products on the anode, it was separated from the working electrode. The working compartment consists of working and reference electrodes, and another one had only the counter electrode. 0.2 M KHCO₃ was used as the electrolyte, and 99.99% pure CO₂ was purged for half an hour prior to the electrochemical process in order to get the saturated state. CO₂ was also bubbled into the cathodic compartment with a constant flow rate during the redox reaction, and a magnetic stirring process was employed to ensure the mass transfer action to the electrode. Fig 15 shows a schematic of the setup used for the electrochemical CO₂ reduction reaction.

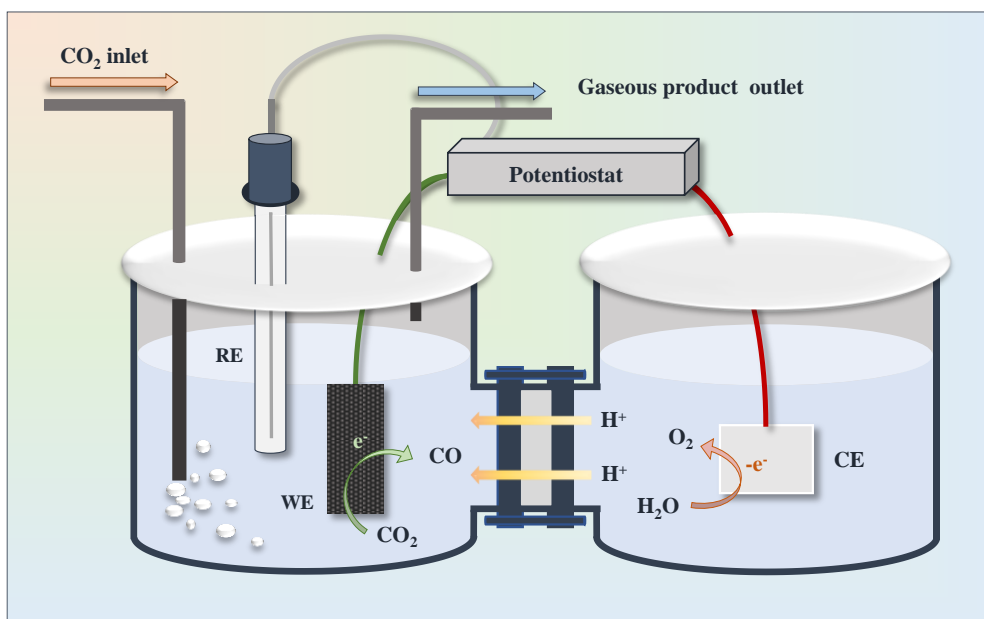


Figure 15. Schematic of the electrochemical setup used for the CO₂RR process. Two separate compartments were used for the cathodic and anodic process, where carbon paper was used as the working electrode, Pt plate as the counter electrode, and Ag/AgCl as the reference electrode.

To confirm the electrochemical CO₂ reduction process by the Ga-Cu xerogel, first linear sweep voltammetry (LSV) was carried out in two different conditions (Fig 16a). The polarisation curve for argon saturated KHCO₃ solution exhibited a cathodic current density of 22 mA/cm² (at -1.38 V vs. RHE) due to the hydrogen evolution process, but a higher current density of 28 mA/cm² (at -1.38 V vs. RHE) was found for the CO₂ saturated solution.

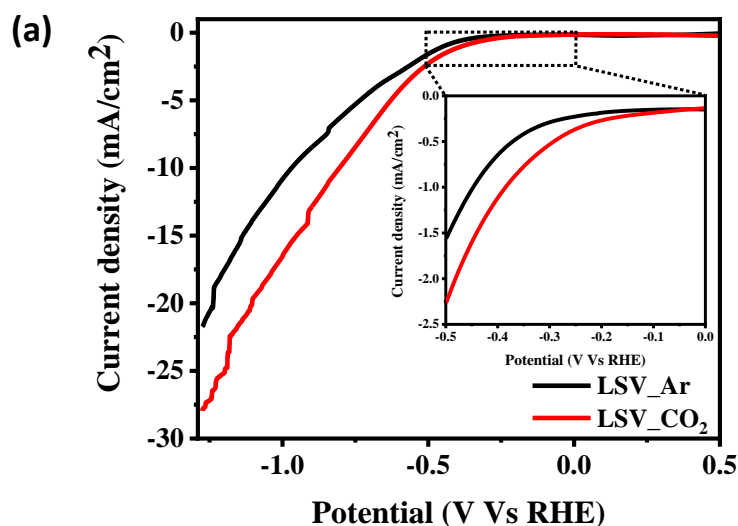


Figure 16. (a) LSV curve of Ga-Cu xerogel in argon saturated (black) and CO₂ saturated 0.2 M KHCO₃ solution by using GC electrode. Inset indicates the lower overpotential of the reduction process in CO₂ saturated solution.

The higher current density for the CO₂ saturated electrolyte confirms a process was happening at the working electrode other than the proton reduction process. To get an indication of the onset potential for the CO₂ reduction process, the electrochemical reduction was carried out at different lower potential regions.⁴⁶ The CO formation was observed in GC-MS at a potential as low as -0.28 V vs. RHE which depicts the onset potential for CO₂RR (Fig. 17a). The overpotential was calculated to be as low as 180 mV.

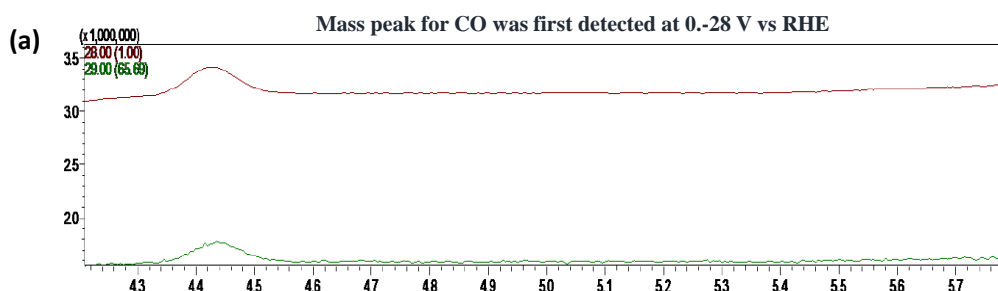


Figure 17. (a) The first peak was obtained for the carbonaceous product (CO) at -0.28 V vs. RHE, indicating the onset for CO₂RR.

Next cyclic voltammetry was performed to understand the redox-active species present in the catalyst. Also, a control experiment was performed for the Ga-MOC and Cu-EDA complex each separately. It was observed that the characteristic reduction and oxidation peaks for the catalyst were well matched with the redox peak found in each constituent for the gel (Fig. 18a). A redox peak at -0.56 V vs. Ag/AgCl for the Ga-Cu xerogel indicates the reduction of the Cu²⁺ to Cu⁺. The oxidation of the Cu⁺ to Cu²⁺ was also found at -0.4 V vs. Ag/AgCl. These two peaks were also found in the case of CV of only Cu-EDA complex, which again confirms the redox-active behaviour of Cu^{II}.⁴⁷

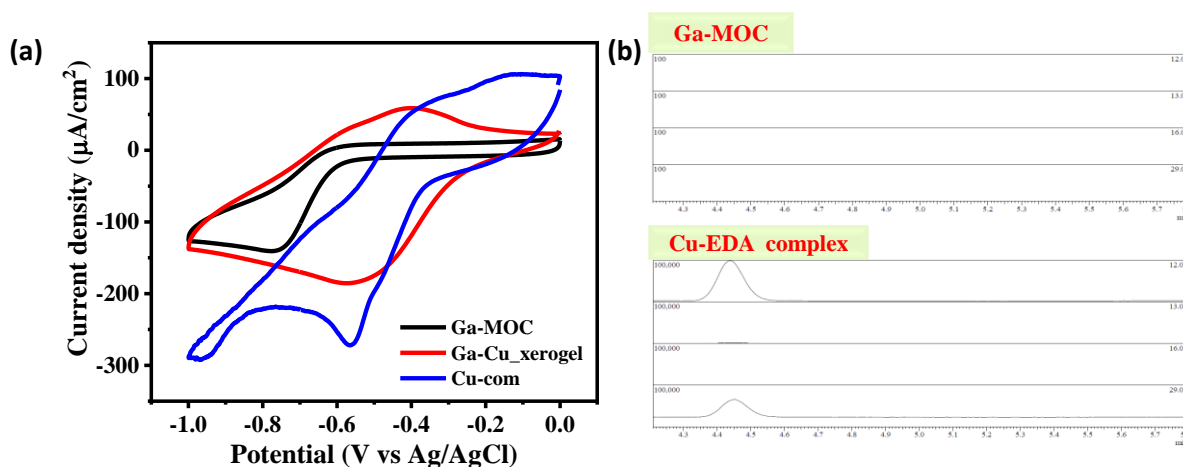


Figure 18. (a) CV curve for Ga-MOC (black), Ga-Cu xerogel (Red), and Cu-EDA complex (blue) taken in 0.2 M TBAHFP solution of acetonitrile by using GC electrode. (b) Mass peak of CO in

GCMS for catalysis with only Ga-MOC and Cu-EDA complex. Peak obtained with only Cu-EDA complex indicates Cu^{II} as the active catalytic center for the CO_2RR process.

As the system had two redox-active metal centers (Cu and Ga), a control experiment was performed with the pristine Ga-MOC to scrutinize the active catalytic site for the CO_2RR . Ga-MOC and Cu-EDA complex were used for electrochemical CO_2RR at the potential -0.98 V vs. RHE under the identical condition as done in the case of Ga-Cu xerogel. No detectable carbonaceous was found for Ga-MOC, but in the case of Cu-EDA complex, the mass peak for CO has been detected in GC-MS (Fig. 18b), indicating the Cu^{II} metal ion as the responsible unit for the CO_2 reduction reaction. To get a better insight into the CO_2 reduction reaction and to evaluate the faradaic efficiency (FE) of the reduced products,⁴⁰ chronoamperometric studies were performed at different potentials (Fig. 19a-b). Ga-Cu xerogel was tested under the six different potentials as follows -0.68 V, -0.78 V, -0.88 V, -0.98 V, -1.08 V, -1.18 V vs. RHE, and the faradaic efficiency distributions were obtained for all the reduced products. Analysis showed, among all the gaseous and liquid products acquired after the reduction event, CO was found to be the major one. Notably, with the application of more negative potential at the cathode, FE was found to be increased for CO with the suppression of the HER process and reached a maximum value of 92% at -0.98 V vs. RHE. Further increment in the negative potential indicates the lower feasibility of the CO_2 reduction reaction over the proton reduction, and the FE of CO was found to be lowering down. No significant change in partial current density for CO was found with increasing in the overpotential.

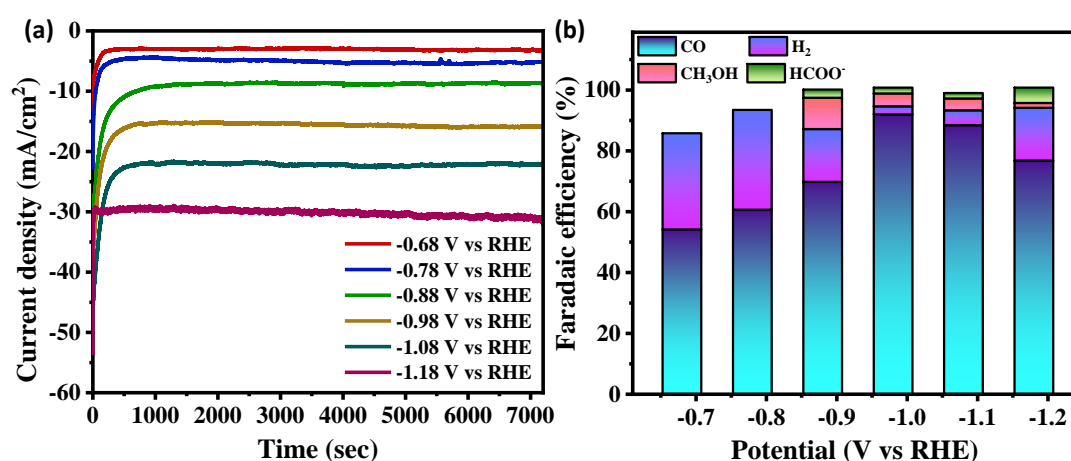


Figure 19. (a) Chronoamperometric response of Ga-Cu xerogel under different potential for 2 hours. The linear current density curve indicates the stability of the catalyst under different potentials. (b) Faradaic efficiency distribution of different products obtains after CO_2RR at different potentials.

This phenomenon is inline with the other reports that suggest the mass transport limitation of CO_2 at the higher total current density. Fig depicted the stability of our catalyst at different potentials as indicated by the linear current density curve over a time of two hours. At the two initial potentials (-0.68 V and -0.78 V), only CO and H_2 were found as the gaseous product without any trace of liquids. The faradaic efficiency of CO (FE_{CO}) was found to be 54% at the potential -0.68 V, which further increased to 60% and 69% at -0.78 and -0.88 V, respectively. First liquid product was obtained at the potential of -0.88 V with a minimal digit of faradaic efficiency. Only C1 products were obtained in the case of gas and liquid, both of which again restricted up to six electrons transfer only. Formate and methanol were found as the reduced products along with CO for only three particular potentials -0.88 V, -0.98 V, and -1.08 V (Fig 21). The faradaic efficiency of HCOO^- was lying between 1.7% to 2.7%, and for the methanol, it was found to be in the range of 4% to 10% in the potential region of -0.88 V to -1.08 V. Distribution curve at -0.98 V shows the highest FE for the CO_2 reduction process and FE of H_2 was found to be as lowest as 2.7% indicating successful crushing of HER activity. Further, the product of FE and current density was plotted against different potential values at which the catalyst was tested.

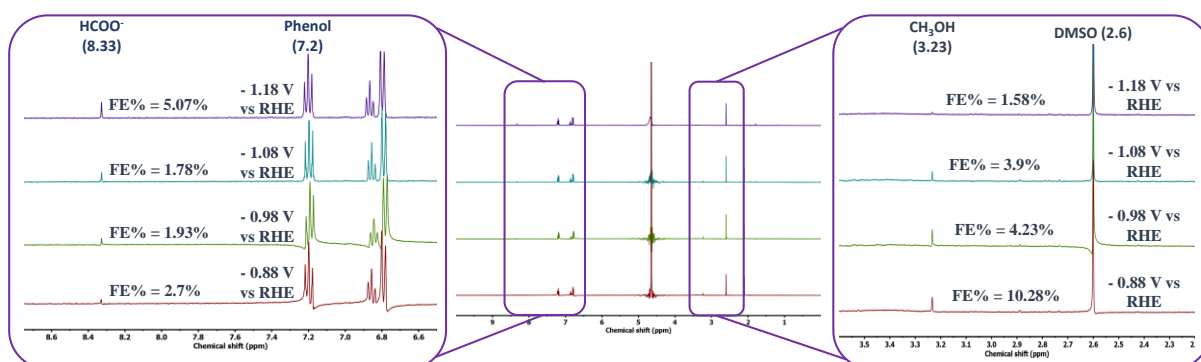


Figure 20. $^1\text{H-NMR}$ analysis of the liquid product after each run for two hours. DMSO and phenol with known concentrations were used externally as the standard, and the peak at 3.23 indicates the methanol, and the 8.33 peak indicates the formate as CO_2RR product.

A lower partial current density (-2.96 mA/cm^2) was obtained for CO (denoted as j_{CO}) at the initial potential region under the CO_2 saturated 0.2 M KHCO_3 solution. But it further accelerated with the increase in negative potential and culminated with -13.66 mA/cm^2 at -0.98 V, corresponding to the peak of the CO faradaic efficiency (Fig. 21a). The Ga-Cu xerogel performs well in terms of faradaic efficiency and shows long-term stability. A chronoamperometric study was carried out at -0.98 V vs. RHE for 16 hours, and the catalyst shows utmost stability towards both faradaic efficiency and current density (Fig 22a). More importantly, it retains 97.5% of the initial current density, and the faradaic efficiency of CO

was maintained throughout the experiment after 16 hours. PXRD pattern and AFM studies also suggest the extreme structural stability of the Ga-Cu xerogel after the electrochemical process (Fig 23a-b).

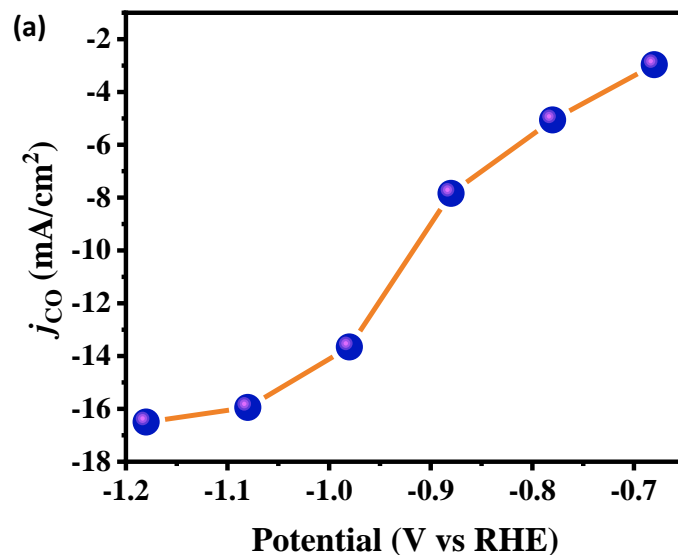


Figure 21. (a) Partial current density curve of CO at different potentials. Current density is saturating after 0.98 V vs. RHE.

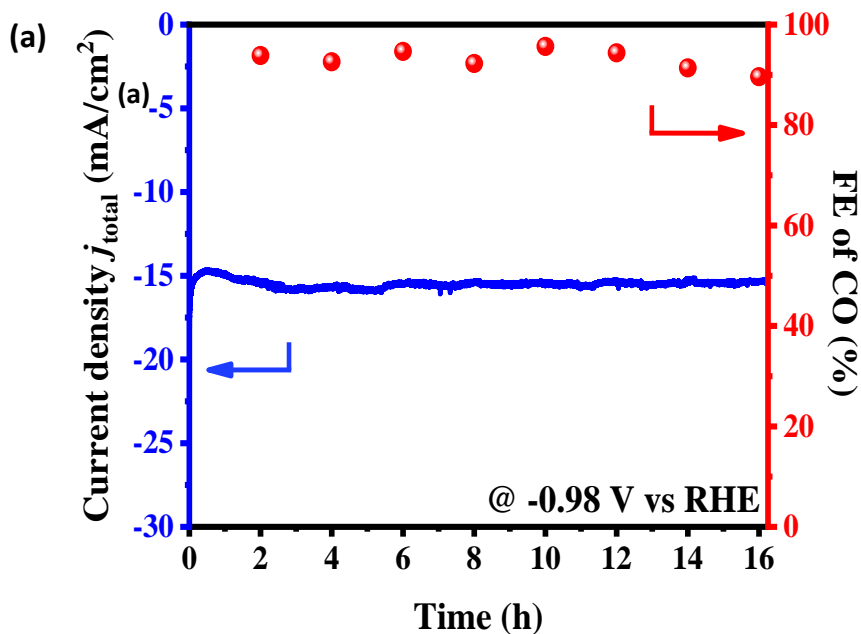


Figure 22. (a) Current density and FE% as a function of time (16 h) during the chronoamperometric study at -0.98 V vs. RHE.

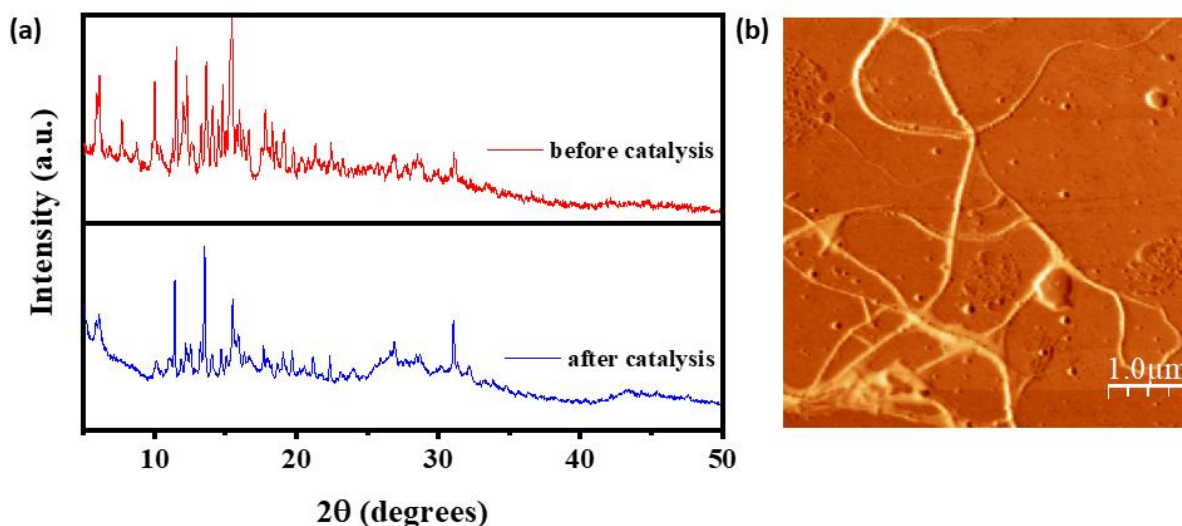


Figure 23. (a) PXRD pattern of the catalyst before (red) and after (blue) the catalysis process. (b) AFM image showed intact fibrous structure of the catalyst after the electrochemical process.

To investigate the origin of CO, first, a control experiment was carried out in 0.2 M KHCO_3 solution with argon saturation instead of CO_2 , which showed negligible production of CO. Further, an isotopic labeling experiment was performed with $^{13}\text{CO}_2$, and the mass peak disposed at 29 corresponded to the ^{13}CO (Fig. 24). Both the experiments unambiguously confirm that the CO is produced due to the reduction of CO_2 only. Considering all the Cu atoms are active toward CO_2RR , the turnover number was calculated to be $1.52 \times 10^{20} \text{ cm}^{-2} \text{ h}^{-1}$, and the turnover frequency was also found to be 987 h^{-1} at the potential -0.98 V .⁴⁶

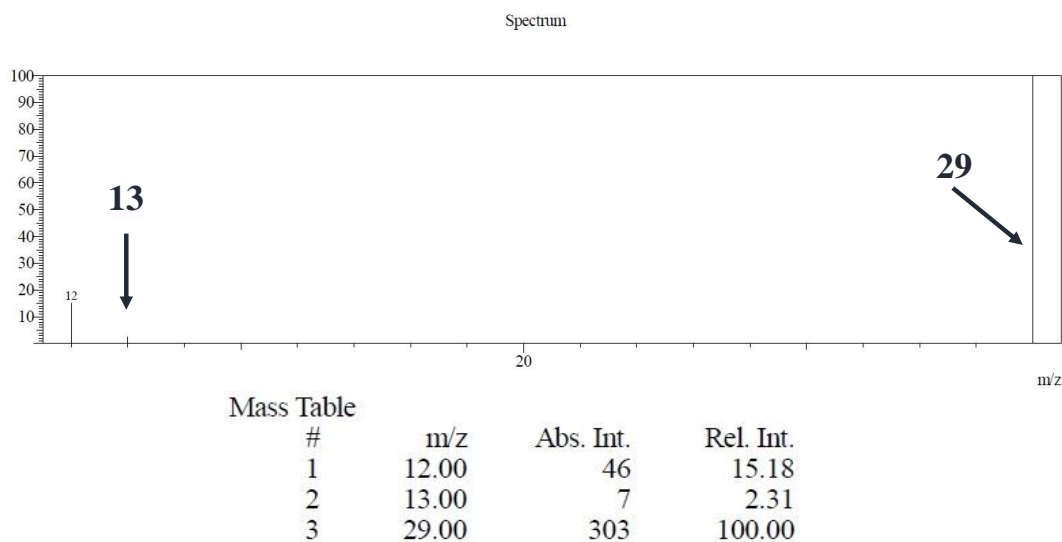


Figure 24. Mass spectrum for ^{13}CO during the electrocatalysis process with $^{13}\text{CO}_2$. A peak at 29 confirms the formation of ^{13}CO .

From the overpotential vs. log of the partial current density curve, the Tafel slope for the Ga-Cu xerogel was calculated to be 85 mV/dec (Fig. 25a). This value suggests the first

elementary electron transfer step is the rate-determining step and concomitantly indicates the formation of COOH^* on the catalyst surface.^{42,48,49} To understand the mechanism of electrochemical reduction of CO_2 , a detailed study was performed by the *in-situ* Diffuse Reflectance Infrared Fourier Transform Spectroscopy (DRIFTS) technique. The possible intermediates in CO_2 to CO pathway were directly detected by this FT-IR study (Fig. 25b). As the electrochemical study suggests, the highest Faradaic efficiency (92%) for CO production was found at -0.98 V vs. RHE. The investigation for the intermediates was also carried out at the same potential, and a change in absorbance was collected with time. The intermediate which can be found after the first electron transfer to the CO_2 is CO_2^- , and the formation of this specie was confirmed by the increase in peak intensity at 1669 cm^{-1} and 1244 cm^{-1} .⁵⁰ Peak arises at 1620 cm^{-1} can be attributed to the HCOO^* attached to the catalyst, which is considered as a crucial intermediate for the production of CO .⁵¹ Now, at the starting of the electrochemical reduction process the two peaks at 1621 cm^{-1} and 1669 cm^{-1} was distinguishable, but with time the peak maxima merged with each other with the increase in peak area and appeared as a single peak. A lower intensity peak was observed at 1488 cm^{-1} , which indicates the weak binding of the CO^* to the metal center and indicates the rapid desorption of CO from the catalyst surface.⁵⁰ New IR peaks were observed at 1543 cm^{-1} and 1360 cm^{-1} corresponded to the bidentate carbonate species.⁵² Detection of these intermediates clearly indicates the reaction progress on the electrode surface.

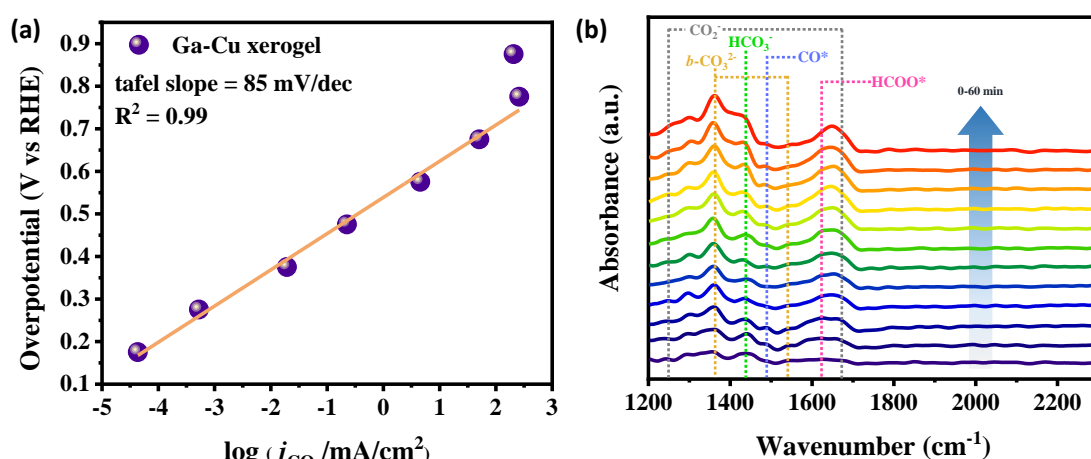


Figure 25. (a) Tafel slope for CO_2 to CO conversion over Ga-Cu xerogel with CO_2 saturated 0.2 M KHCO_3 solution. (b) *in-situ* DRIFTS measurement using Ga-Cu xerogel coated graphite rod as the working electrode with a CO_2 saturated 0.2 M KHCO_3 solution.

4.6 Summary:

In summary, we have developed a binder-driven self-assembled soft material. An extended nanostructure was observed for the Ga-Cu hydrogel, which shows a morphological change with time. An interesting phenomenon was observed where the gel to crystal transformation was found in a spontaneous way. This material was used for electrocatalytic CO₂ reduction reaction to CO. It shows a remarkable, resulting performance with a faradaic efficiency of 92% at a potential -0.98 V vs. RHE at pH=7. In addition to this, our catalyst shows an excellent stability towards the electrolysis process at -0.98 V vs. RHE for 16 hours. This work summarises the rational design of a soft heterogeneous electrocatalytic material for the CO₂RR process under mild conditions.

4.7 References:

- 1 P. Sutar and T. K. Maji, *Chem. Commun.*, 2016, **52**, 8055–8074.
- 2 J. Raeburn, A. Z. Cardoso and D. J. Adams, *Chem. Soc. Rev.*, 2013, **42**, 5143–5156.
- 3 J. Raeburn and D. J. Adams, *Chem. Commun.*, 2015, **51**, 5170–5180.
- 4 N. J. Oldenhuis, K. P. Qin, S. Wang, H. Ye, E. A. Alt, A. P. Willard, T. Van Voorhis, S. L. Craig and J. A. Johnson, *Angew. Chemie*, 2020, **132**, 2806–2814.
- 5 A. V. Zhukhovitskiy, M. Zhong, E. G. Keeler, V. K. Michaelis, J. E. P. Sun, M. J. A. Hore, D. J. Pochan, R. G. Griffin, A. P. Willard and J. A. Johnson, *Nat. Chem.*, 2016, **8**, 33–41.
- 6 A. Legrand, G. A. Craig, M. Bonneau, S. Furukawa, S. Minami, K. Urayama and S. Furukawa, *Chem. Sci.*, 2019, **10**, 10833–10842.
- 7 A. Legrand, L. H. Liu, P. Royla, T. Aoyama, G. A. Craig, A. Carné-Sánchez, K. Urayama, J. J. Weigand, C. H. Lin and S. Furukawa, *J. Am. Chem. Soc.*, 2021, **143**, 3562–3570.
- 8 Z. Wang, C. Villa Santos, A. Legrand, F. Haase, Y. Hara, K. Kanamori, T. Aoyama, K. Urayama, C. M. Doherty, G. J. Smales, B. R. Pauw, Y. J. Colón and S. Furukawa, *Chem. Sci.*, 2021, **12**, 12556–12563.
- 9 A. Carné-Sánchez, G. A. Craig, P. Larpent, T. Hirose, M. Higuchi, S. Kitagawa, K. Matsuda, K. Urayama and S. Furukawa, *Nat. Commun.*, 2018, **9**, 1–8.

- 10 H. C. Moon, T. P. Lodge and C. D. Frisbie, *J. Am. Chem. Soc.*, 2014, **136**, 3705–3712.
- 11 P. Sutar, V. M. Suresh and T. K. Maji, *Chem. Commun.*, 2015, **51**, 9876–9879.
- 12 Q. Xie, Y. Zhuang, G. Ye, T. Wang, Y. Cao and L. Jiang, *Nat. Commun.*, 2021, **12**, 1–9.
- 13 J. Zheng, R. Fan, H. Wu, H. Yao, Y. Yan, J. Liu, L. Ran, Z. Sun, L. Yi, L. Dang, P. Gan, P. Zheng, T. Yang, Y. Zhang, T. Tang and Y. Wang, *Nat. Commun.*, , DOI:10.1038/s41467-019-09601-3.
- 14 J. Hur, K. Im, S. W. Kim, J. Kim, D. Y. Chung, T. H. Kim, K. H. Jo, J. H. Hahn, Z. Bao, S. Hwang and N. Park, *ACS Nano*, 2014, **8**, 10066–10076.
- 15 S. Sarkar, P. K. Maji, Y. Negishi, S. Dutta, T. N. Das, R. Pan and S. Sarkar, *ACS Appl. Nano Mater.*, 2021, **4**, 1455–1466.
- 16 A. Prathap and K. M. Sureshan, *Angew. Chemie Int. Ed.*, 2017, **56**, 9405–9409.
- 17 D. Dietrich, C. Licht, A. Nuhnen, S.-P. Höfert, L. De Laporte and C. Janiak, *ACS Appl. Mater. Interfaces*, 2019, **11**, 19654–19667.
- 18 A. C. Ghosh, A. Legrand, R. Rajapaksha, G. A. Craig, C. Sassoeye, G. Balázs, D. Farrusseng, S. Furukawa, J. Canivet and F. M. Visser, *J. Am. Chem. Soc.*, 2022, **144**, 3626–3636.
- 19 D. Giuri, L. J. Marshall, B. Dietrich, D. McDowall, L. Thomson, J. Y. Newton, C. Wilson, R. Schweins and D. J. Adams, *Chem. Sci.*, 2021, **12**, 9720–9725.
- 20 R. Mohanrao, K. Hema and K. M. Sureshan, *Nat. Commun.*, 2020, **11**, 1–8.
- 21 S. Satapathy, P. Prabakaran and E. Prasad, *Chem. - A Eur. J.*, 2018, **24**, 6217–6230.
- 22 X. Zhang, Z. Wu, X. Zhang, L. Li, Y. Li, H. Xu, X. Li, X. Yu, Z. Zhang, Y. Liang and H. Wang, *Nat. Commun.*, 2017, **8**, 1–8.
- 23 D. H. Nam, P. De Luna, A. Rosas-Hernández, A. Thevenon, F. Li, T. Agapie, J. C. Peters, O. Shekhah, M. Eddaoudi and E. H. Sargent, *Nat. Mater.*, 2020, **19**, 266–276.
- 24 S. Nitopi, E. Bertheussen, S. B. Scott, X. Liu, A. K. Engstfeld, S. Horch, B. Seger, I. E. L. Stephens, K. Chan, C. Hahn, J. K. Nørskov, T. F. Jaramillo and I. Chorkendorff, *Chem. Rev.*, 2019, **119**, 7610–7672.

- 25 V. Talanquer, D. Oxtoby, M. F. Islam, J. Zhang, P. J. Collings, A. G. Yodh, H. Gleiter, J. Perepezko, M. Terrones, J. R. Dwyer, R. E. Jordan, R. J. Miller, M. Enomoto, J. K. Lee, F. Group, H. N. Lekkerkerker, D. G. Grier, E. R. Weeks, A. Schofield, P. N. Pusey, D. A. Weitz, D. W. Blair, A. J. Levine, R. A. Guyer, A. D. Dinsmore, A. M. Alsayed, A. G. Yodh, Y. Han, W. Van Megen, D. G. Grier, A. Dobry, H. T. Diep, L. Burakovsky, D. L. Preston, R. R. Silbar, G. Grimvall, M. Li, A. Bongiorno, W. Ostwald, M. Li, A. R. Denton, N. W. Ashcroft, S. Auer, D. Frenkel, R. L. Davidchack, D. Moroni, P. G. Bolhuis, K. Lu, Y. Li, Z. H. Jin, P. Gumbsch and K. Lu, *Science (80-.)*, 2012, **338**, 90–94.
- 26 X. Chen, J. Chen, N. M. Alghoraibi, D. A. Henckel, R. Zhang, U. O. Nwabara, K. E. Madsen, P. J. A. Kenis, S. C. Zimmerman and A. A. Gewirth, *Nat. Catal.*, 2021, **4**, 20–27.
- 27 W. Ju, A. Bagger, G. P. Hao, A. S. Varela, I. Sinev, V. Bon, B. Roldan Cuenya, S. Kaskel, J. Rossmeisl and P. Strasser, *Nat. Commun.*, 2017, **8**, 1–9.
- 28 K. Niu, Y. Xu, H. Wang, R. Ye, H. L. Xin, F. Lin, C. Tian, Y. Lum, K. C. Bustillo, M. M. Doeff, M. T. M. Koper, J. Ager, R. Xu and H. Zheng, *Sci. Adv.*, 2017, **3**, 1–10.
- 29 H. Wang, J. Jia, P. Song, Q. Wang, D. Li, S. Min, C. Qian, L. Wang, Y. F. Li, C. Ma, T. Wu, J. Yuan, M. Antonietti and G. A. Ozin, *Angew. Chemie*, 2017, **129**, 7955–7960.
- 30 Z. Weng, Y. Wu, M. Wang, J. Jiang, K. Yang, S. Huo, X. F. Wang, Q. Ma, G. W. Brudvig, V. S. Batista, Y. Liang, Z. Feng and H. Wang, *Nat. Commun.*, 2018, **9**, 1–9.
- 31 K. P. Kuhl, T. Hatsukade, E. R. Cave, D. N. Abram, J. Kibsgaard and T. F. Jaramillo, *J. Am. Chem. Soc.*, 2014, **136**, 14107–14113.
- 32 D. Yang, Q. Zhu, C. Chen, H. Liu, Z. Liu, Z. Zhao, X. Zhang, S. Liu and B. Han, *Nat. Commun.*, 2019, **10**, 1–9.
- 33 Z. Weng, J. Jiang, Y. Wu, Z. Wu, X. Guo, K. L. Materna, W. Liu, V. S. Batista, G. W. Brudvig and H. Wang, *J. Am. Chem. Soc.*, 2016, **138**, 8076–8079.
- 34 C. T. Dinh, T. Burdyny, G. Kibria, A. Seifitokaldani, C. M. Gabardo, F. Pelayo García De Arquer, A. Kiani, J. P. Edwards, P. De Luna, O. S. Bushuyev, C. Zou, R. Quintero-Bermudez, Y. Pang, D. Sinton and E. H. Sargent, *Science (80-.)*, 2018, **360**, 783–787.
- 35 A. Loiudice, P. Lobaccaro, E. A. Kamali, T. Thao, B. H. Huang, J. W. Ager and R.

- Buonsanti, *Angew. Chemie - Int. Ed.*, 2016, **55**, 5789–5792.
- 36 Y. Liu, Y. Zhang, K. Cheng, X. Quan, X. Fan, Y. Su, S. Chen, H. Zhao, Y. Zhang, H. Yu and M. R. Hoffmann, *Angew. Chemie - Int. Ed.*, 2017, **56**, 15607–15611.
- 37 Z. Sun, T. Ma, H. Tao, Q. Fan and B. Han, *Chem*, 2017, **3**, 560–587.
- 38 H. Guzmán, N. Russo and S. Hernández, *Green Chem.*, 2021, **23**, 1896–1920.
- 39 Y. Y. Birdja, E. Pérez-Gallent, M. C. Figueiredo, A. J. Göttle, F. Calle-Vallejo and M. T. M. Koper, *Nat. Energy*, 2019, **4**, 732–745.
- 40 H. Xu, D. Rebollar, H. He, L. Chong, Y. Liu, C. Liu, C. J. Sun, T. Li, J. V. Muntean, R. E. Winans, D. J. Liu and T. Xu, *Nat. Energy*, 2020, **5**, 623–632.
- 41 N. Sikdar, J. R. C. Junqueira, S. Dieckhöfer, T. Quast, M. Braun, Y. Song, H. B. Aiyappa, S. Seisel, J. Weidner, D. Öhl, C. Andronescu and W. Schuhmann, *Angew. Chemie - Int. Ed.*, 2021, **60**, 23427–23434.
- 42 J. Jiao, R. Lin, S. Liu, W. C. Cheong, C. Zhang, Z. Chen, Y. Pan, J. Tang, K. Wu, S. F. Hung, H. M. Chen, L. Zheng, Q. Lu, X. Yang, B. Xu, H. Xiao, J. Li, D. Wang, Q. Peng, C. Chen and Y. Li, *Nat. Chem.*, 2019, **11**, 222–228.
- 43 R. Angamuthu, P. Byers, M. Lutz, A. L. Spek and E. Bouwman, *Science (80-.)*, 2010, **327**, 313–315.
- 44 P. Sutar, V. M. Suresh, K. Jayaramulu, A. Hazra and T. K. Maji, *Nat. Commun.*, 2018, **9**, 1–12.
- 45 Y. Komiyama and E. C. Lingafelter, *Acta Crystallogr.*, 1964, **17**, 1145–1148.
- 46 H. Bin Yang, S. F. Hung, S. Liu, K. Yuan, S. Miao, L. Zhang, X. Huang, H. Y. Wang, W. Cai, R. Chen, J. Gao, X. Yang, W. Chen, Y. Huang, H. M. Chen, C. M. Li, T. Zhang and B. Liu, *Nat. Energy*, 2018, **3**, 140–147.
- 47 M. Wałęsa-Chorab, R. Banasz, D. Marcinkowski, M. Kubicki and V. Patroniak, *RSC Adv.*, 2017, **7**, 50858–50867.
- 48 T. Zheng, K. Jiang, N. Ta, Y. Hu, J. Zeng, J. Liu and H. Wang, *Joule*, 2019, **3**, 265–278.
- 49 M. Zhao, Y. Gu, P. Chen, Z. Xin, H. Zhu, B. Wang, K. Zhu, S. Yan and Z. Zou, *J.*

- Mater. Chem. A*, 2019, **7**, 9316–9323.
- 50 L. Liu, H. Zhao, J. Andino, Y. Li, *ACS Catal.*, 2012, **2**, 1817–1828.
- 51 X. Li, Y. Sun, J. Xu, Y. Shao, J. Wu, X. Xu, Y. Pan, H. Ju, J. Zhu and Y. Xie, *Nat. Energy*, 2019, **4**, 690–699.
- 52 X. Rtm, Y. Ph and X. Whd, *Joule*, 2018, **2**, 1004–1016.

Summary and Future Outlook

The thesis work comprises of self-assembly of different gelator molecules to the formation of the gel. These inorganic-organic hybrid soft materials were exploited in energy and environment-related applications. Various molecules with π -electron rich units and small metal-organic cubes were employed as the gelator with some linker units. The low molecular weight organogelator consists of π -electron rich chromophore with terminal terpyridine groups as coordinating sites, and these two units were covalently connected through a flexible amidealkyl chain. This bipodal ligand was further connected with each other through metal ion binding, where Fe(II) was taken as a redox-active center. Introduction of metal ions induces different photophysical and electrochemical properties. Based on these properties, the CPG was employed in photocatalytic CO₂ reduction reaction to different value-added products with high productivity, selectivity, and it also shows high stability. Furthermore, Ga(III) based metal-organic cubes were taken as gelator, and the self-assembly process was explored in the form of hydrogel. Different -NH₂ group containing metal complexes were employed as the binder, which arranged these MOCs in a well-oriented fashion through charge-assisted hydrogen bonding. These MOC-based hydrogels showed a spontaneous gel to crystal transition. This phenomenon was investigated through morphological and rheological properties of different stoichiometric gels. Redox-active metal complex containing heterogeneous system was utilized in electrochemical CO₂ reduction reaction with high faradaic efficiency towards CO formation.

The implementation of these hybrid gel materials as a catalyst in the CO₂ reduction application is in an infant stage, which is yet to be explored in different way. The future research objective will include the modification of the LMWG with different metal centers to realize the novel properties of gel materials. Current thesis work is only dealing with C1 products from photocatalytic and electrocatalytic CO₂ reduction reactions, which can be improved to C2 or C3 by coupling these two aforementioned methods. Incorporation of DTE-based photoresponsive materials into this soft hybrid system to realise the mechanical strength and morphological difference with light irradiation can be an interesting topic to be explored. The self-healing properties of these soft materials are another interest in this field. This thesis only deals with a single gelator component, whereas the physical properties of these soft materials can be tuned with a hybrid multicomponent system, which can be done with different clay materials and 2D materials. Overall the well-designed gelator molecules and

corresponding organogel and metallogel cover a widespread interest in material science. Hence, the implementation of these soft hybrid materials with superior efficacy can fulfill the energy requirements.

Biography



Tarak Nath Das was born on August 28, 1998, in Murshidabad, West Bengal (India). He completed his B.Sc. Hons. Chemistry (2019) from Ramakrishna Mission Vivekananda Centenary College, Rahara, Kolkata. He joined as an Int. Ph.D. student (Chemical Sciences) at New Chemistry Unit of Jawaharlal Nehru Centre for Advanced Scientific Research (JNCASR), Bangalore, India, in August 2019. Currently, he is working with Prof. Tapas Kumar Maji as an MS student from August 2020. His research work is focused on multifarious properties and applications of Hybrid Gel Materials.

